Advanced Gas Turbine

AGT

Technology Project

DOE/NASA/0168-8
NASA CR-174798
EDR 11682

Eighth Semiannual Report
For work performed from
1 July 1983 - 31 December 1983

Allison
GAS TURBINE DIVISION
General Motors Corporation
P O Box 420
Indianapolis, Indiana 46206-0420

June 1985

(NASA-CR-174798) ADVANCED GAS TURBINE (AGT) TECHNOLOGY PROJECT Semiannual Report (Detroit Diesel Allison) 94 p HC A05/MF A01 CSCL 21E

N85-29961

Unclas
G3/07 21675

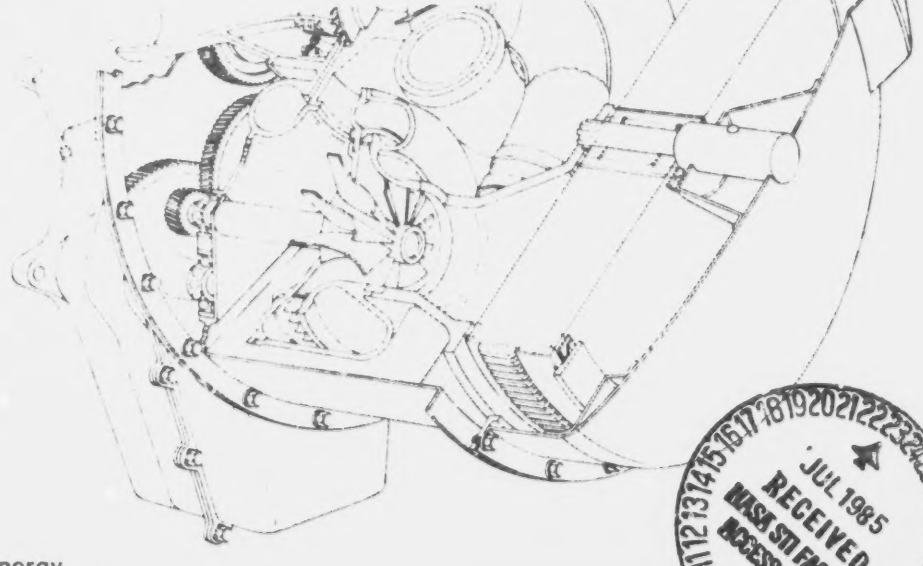

Prepared for
National Aeronautics
and Space Administration
Lewis Research Center
Cleveland, Ohio 44135
Contract DEN 3-168

For U. S. Department of Energy
Conservation and Renewable Energy
Office of Vehicle and Engine Research and Development

JUL 1985
RECEIVED
NASA STI FACILITY
ACCESS DEPT.

DOE/NASA/0168-8
NASA CR-174798
EDR 11682

Advanced Gas Turbine
AGT
Technology Project

Eighth Semiannual Report
For work performed from
1 July 1983 - 31 December 1983

Allison Gas Turbine Division
General Motors Corporation
Indianapolis, Indiana 46206-0420

June 1985

Prepared for
NATIONAL AERONAUTICS AND SPACE ADMINISTRATION
Lewis Research Center
Under Contract DEN 3-168

for
U.S. Department of Energy
Conservation and Renewable Energy
Office of Vehicle and Engine Research and Development

FOREWORD

This report presents a technical summary of the Allison Gas Turbine project to develop an automotive gas turbine power-train system under NASA Contract DEN 3-168 (Department of Energy funding). The report covers the 6-month period 1 July 1983 through 31 December 1983.

The basic objective of this project is to develop and demonstrate an advanced automotive gas turbine that will, when installed in a Pontiac Phoenix class vehicle of 1360 kg (3000 lbm) inertia weight, achieve a fuel economy of 18 km/L (42.5 mpg), meet or exceed the 1985 emission requirements, and have alternate fuel capability.

Several General Motors Divisions and other companies are major contributors to this effort. They are as follows: Pontiac Motor Division—vehicle and cost studies, Delco Remy Division—starter/boost motor, Corning Glass Works—regenerator, The Carborundum Company and GTE—ceramics.

The Allison Program Manager for the AGT 100 is H. E. (Gene) Helms; design effort is directed by Leonard Lindgren; materials effort is directed by Dr. Peter Heitman; and project effort is directed by Richard Johnson. The Pontiac effort is headed by Leighton Smith. The NASA AGT 100 Project Manager is Paul T. Kerwin.

TABLE OF CONTENTS

Section	Title	Page
	Summary	1
	Introduction	2
I	Vehicle System Development*	
II	Engine Development	6
	2.1 Reference Power-Train Design*	
	2.2 Experimental Engine	6
	2.2.1 Fabrication	6
	2.2.2 Experimental Engine Testing	6
	2.2.3 Performance Analysis	10
III	Compressor Development	13
	3.1 Compressor Aerodynamic Development	13
	3.1.1 Task 1—Effect of Impeller Diffusion Levels (AREQ)	13
	3.1.2 Task 2—Alternate Impeller Designs	14
	3.2 Compressor Rig Mechanical Development	15
	3.3 Compressor Mechanical Development	17
IV	Gasifier Turbine Development	20
	4.1 Gasifier Turbine Aerodynamic Development	20
	4.2 Gasifier Turbine Mechanical Development	20
	4.3 Ceramic Gasifier Turbine Design	21
	4.3.1 Transient Three-Dimensional Finite Element Scroll Analysis	21
	4.3.2 Alternate Design Scrolls	28
	4.3.3 Gasifier Turbine Rotor	28
V	Power Turbine Development	33
	5.1 Power Turbine Aerodynamic Development	33
	5.2 Power Turbine Mechanical Development	33
VI	Combustor Development	37
	6.1 Test Facility	37
	6.2 Test Results	38
	6.2.1 Proof Testing	39
	6.2.2 Start-Nozzle Testing	39
	6.2.3 Pilot Testing	39
	6.2.4 Main-Nozzle Testing	40
	6.3 Heat Transfer Analysis	42
VII	Regenerator Development	45
	7.1 Design and Material Development	45
	7.1.1 Outboard Seals	45
	7.1.2 Inboard Seals	46
	7.1.3 Regenerator Disks	48
	7.1.4 Parts Fabrication	53

*No activity this period

PRECEDING PAGE BLANK NOT FILMED

TABLE OF CONTENTS (cont)

Section	Title	Page
	7.2 Rig Development Testing	54
	7.3 Engine Testing	54
VIII	Secondary Systems	56
	8.1 Gearbox	56
	8.2 Bearings and Seals	56
	8.3 Secondary Airflow Systems	57
IX	Materials Development	63
	9.1 Thermal Barrier Development	63
	9.1.1 Carborundum (CBO) Mullite Development	63
	9.1.2 Zircon Thermal Barrier Material	63
	9.2 Silicon Carbide Component Development	66
	9.2.1 Gasifier Rotor	66
	9.2.2 Gasifier Turbine Scroll Assembly	74
	9.3 Silicon Nitride Component Development	78
X	Controls Development	79
	10.1 Engine Operation without Pilot Flame	79
	10.2 Software Changes to Support Engine Testing	79
	10.2.1 Burner Variable Geometry Control	79
	10.2.2 Pilot Light-Off Detection	79
	10.3 Main Fuel Nozzle Purge	79
	10.4 Improved Fuel System	79
	10.4.1 Electric Fuel Pump	79
	10.4.2 Fuel Metering Valve	79
	10.4.3 Electronic Control Unit	80
XI	Transmission Development*	
XII	Supportive Manufacturing, Cost, and Marketability	81
	12.1 Manufacturing Feasibility	81
	12.2 Cost Analysis*	
	Appendix A. Terms and Definitions	84

*No activity this period

LIST OF ILLUSTRATIONS

Section	Title	Page
1	AGT 100 Project Plan	3
2	AGT 100 engine in 1985 Pontiac Phoenix	3
3	AGT 100 advanced gas turbine engine	4
4	Cross section of AGT 100 gas turbine engine	4
5	AGT 100 ceramic components	5
6	AGT 100 engine test hours	10
7	AGT 100 performance comparison of net power	11
8	AGT 100 performance comparison of fuel rate	11
9	AGT 100 performance comparison of airflow	11
10	AGT 100 performance comparison of pressure ratio	11
11	Meridional flow-path elevation	13
12	Impeller shroud diffusion	14
13	Impeller blade normal thickness distribution	14
14	Cross section of modified compressor rig	16
15	AGT 100 impeller hub and shroud blade thicknesses	19
16	New gasifier vane aerodynamic profile	20
17	Gasifier turbine scroll to power turbine scroll gap	23
18	AGT 100 reference power-train design start transient	23
19	AGT 100 ceramic scroll body temperature and maximum principal stress distribution	24
20	AGT 100 ceramic shroud temperature and maximum principal stress distribution	25
21	AGT 100 ceramic backplate temperature and maximum principal stress distribution	26
22	AGT 100 ceramic exit elbow tube temperature and maximum principal stress distribution	27
23	Alternate slip-cast scroll design configuration	28
24	Required volume characteristic strength for the fully machined rotor	29
25	Candidate scheme for the ceramic rotor/metal shaft attachment	31
26	Candidate scheme for the ceramic rotor/metal shaft attachment	31
27	A finite element model for the ceramic rotor/metal shaft attachment study	32
28	A dimensional comparison of new and original power turbine exhaust couplings	36
29	Airflow over AGT 100 combustor in engine	38
30	Airflow over the AGT 100 combustor as installed in the rig	38
31	Schematic showing placement of igniters in centerbody	40
32	A side view of the pilotless combustor centerbody	40
33	A front view of the pilotless combustor centerbody	40
34	A plot of burner variable geometry position as a function of fuel/air ratio and burner inlet temperature	41
35	Burner variable geometry map for engine S/N D-2, BU3	42
36	Finite element model of the AGT 100 combustor	43
37	AGT 100 combustor body temperatures at 30 sec into the starting transient	43
38	AGT 100 combustor body temperatures at steady-state conditions—1649°C (3000°F) primary and 954°C (1750°F) secondary (T_6)	43
39	Outboard seal development sequence	45
40	Cross section showing the thermal barrier addition to metal platform/silicone leaf seal	46
41	Photograph of polyimide outboard seal wearface	46
42	AGT 100 inboard seal platform temperature profile with and without cooling	46
43	A graph of maximum platform temperature as a function of gas temperature including extrapolation to the RPD to design temperature	47
44	A comparison of the current inboard seal crossarm and a cooled interface concept	48
45	AGT 100 regenerator matrix configurations	49

LIST OF ILLUSTRATIONS (cont)

Section	Title	Page
46	Strength of Corning Glass Works AS matrix at reduced temperature gradients showing negligible changes	50
47	A photograph showing radial and circumferential cracks in AGT 100 disk 17-01 after 80 hr of testing	50
48	History of disk failures compared with measured through-wall leakage rates indicating low strength is at least partially due to high wall porosity	51
49	CTE test strength for MAS CO3P and C09P samples	52
50	A photograph showing the hot face of an AGT 100 regenerator disk with NGK C03P extruded matrix	53
51	Illustration of the loss of hot face rim relief slot filler that occurred during testing with C03P disk G-1	53
52	Magnesium-aluminum-silicate disk S/N G-2 after 46 hr testing	54
53	Cyclic thermal exposure test strength of MAT matrix exposed to 1179°C for 100 cycles	54
54	A cross section of the redesigned bulkhead and power turbine coupling	55
55	Photograph of the seal wearface failure on engine S/N D-2, BU1	55
56	The oil pump assembly showing the original regulating valve	56
57	The oil pump assembly showing the improved regulating valve	56
58	A cross section of the carbon seal installation showing the improved cooling arrangement	57
59	A schematic of the AGT 100 helium leak detection system	58
60	A schematic highlighting the carbon dioxide dilution measurements for AGT 100 leakage testing	59
61	A schematic of the AGT 100 regenerator rig leakage measurement system	60
62	A schematic defining the seven leakage sites included in the performance model leakage sensitivity study	61
63	AGT 100 sensitivity to leakage at each of the seven sites defined for the performance model	62
64	Anticipated power gains for 10% leakage reduction at the seven leakage sites	62
65	Percent expansion of sintered SiC and mullite/cordierite samples showing a slightly greater percentage for the mean values of mullite as compared with sintered SiC	65
66	Location of test bars cut from CBO sintered alpha SiC rotors	66
67	Microphotographs of typical strength-controlling defects observed in a CBC sintered SiC rotor test bar	73
68	Cumulative probability plot of spin-burst failure for 19 Group I rotors	75
69	Cumulative probability plot of spin-burst failure for nine Group I rotors meeting all NDE requirements	75
70	Technical milestone plan for development of the rotor/shaft attachment	76
71	Ceramic scroll assembly No. 1 photograph showing FPI indications on the outer surface and a broken tab	77
72	Ceramic scroll assembly No. 1 photograph showing machined shroud surfaces	77
73	Internal surface of GTE Laboratories HIP processed injection molded AY6-100 Si_3N_4 rotor	78
74	BVG map for operation without pilot flame	80
75	Combustion case assembly bulkhead made from experimental die	81
76	Initial four-piece weldment design for regenerator housing	82
77	Proposed one-piece regenerator housing made from experimental die	82

LIST OF TABLES

Section	Title	Page
I	AGT 100 project and design objectives	2
II	Aerodynamic component rigs	4
III	Comparison of impeller geometric variables	15
IV	Engine S/N D-1 compressor clearance measurements	18
V	Engine S/N D-2 compressor clearance measurements	18
VI	Comparison of vane design parameters	21
VII	Engine S/N D-1 gasifier turbine clearance measurements	22
VIII	Engine S/N D-2 gasifier turbine clearance measurements	22
IX	Probability of survival summary (50 sec transient)	23
X	Alpha SiC strength properties (CATE project bar data)	30
XI	Gasifier rotor probability of survival at various conditions	30
XII	Power turbine predicted maximum power operating parameters	34
XIII	Engine S/N D-1 power turbine clearance measurements	35
XIV	Engine S/N D-2 power turbine clearance measurements	35
XV	Transient heat transfer analysis	44
XVI	Summary of as-received disk properties	49
XVII	Critical properties of mullite thermal barrier material	64
XVIII	Critical properties of zircon-based thermal barrier material	65
XIX	Biaxial strength of zircon-based thermal barrier material	66
XX	Spin test, ECR samples (first 100)	67
XXI	Process development, gasifier turbines	68
XXII	Summary, development ECRs	69
XXIII	Strength characteristics of CBO sintered alpha SiC gasifier rotors	74
XXIV	Rotor spin burst tests (Group I rotors)	75

SUMMARY

Significant development activity occurred during the July-December 1983 period in the Allison-Pontiac AGT 100 Advanced Gas Turbine Technology Project. The areas of ceramic components, aerodynamic components, and experimental engines all shared in development progress.

Two builds (9 and 10) of engine serial number (S/N) D-1 were evaluated through dynamometer testing. Accumulated test time was 11 hr 42 min, raising its total time to 20 hr 40 min. A second engine, S/N D-2, was assembled and accumulated 20 hr 39 min of test. Only two builds of engine S/N D-2 were required, and only the regenerator was disassembled between the two builds. Through 1983, total accumulated engine test time (burning) was 41 hr 19 min. Engine S/N D-2 incorporated a modification to the interface system between the ceramic regenerator bulkhead and power turbine scroll assembly. This change solved the problem of cracked bulkheads experienced on the last builds of engine S/N D-1. A design modification was defined to eliminate the tendency to leak hot gas from the engine flow path into the gearbox vent cavity. This leak characteristically increases with operating time due to deterioration of sealing material.

Compressor aerodynamic analyses that identified impeller modifications for improved performance were completed. These near-term improvements will be tested next period on a compressor rig that was modified for improved control of heat transfer between the flow path and structural path.

Two turbine aerodynamic improvements were designed for 1984 implementation. They are an improved gasifier vane shape and a reduced capacity power turbine. This latter change has improved component matching in the experimental engine.

Combustor development included rig changes to better simulate the engine flow path and to provide viewing stations for use of optical pyrometers. Rig testing was conducted to proof-test ceramic units, to examine starting and igniter relocations, and to map stability limits.

Regenerator testing evaluated 23 disk/seal combinations in 145 hr of hot rig testing. Advanced concepts included a silicone leaf seal, polyimide integral wearface and seal platform, different cross-arm cooling systems, low-leakage aluminum silicate disks, and an extruded magnesium aluminum silicate disk.

Ceramic turbine rotor development experienced improvement in molding, baking, and sintering engine configuration rotors. Nineteen sintered alpha silicon carbide rotors were cold-spin tested to failure. Average burst speed was 94,930 rpm. Of these rotors, the nine of highest quality had an average burst speed of 99,330 rpm. These nine rotors had minor surface flaws which for engine use could be removed by machining.

The first finish-machined ceramic scroll assembly was received. This assembly, made of sintered alpha silicon carbide, is composed of five separate component parts. Fabrication of a thermal shock rig for proof-testing static ceramic components was initiated, and most rig parts were completed by the end of 1983.

INTRODUCTION

This is one of a series of semiannual reports documenting work performed on an Advanced Gas Turbine (AGT) Technology Development Project for automotive applications. The work is being conducted by Allison Gas Turbine Operations of General Motors Corporation under NASA/DOE contract DEN-168.

The objectives of the project, as highlighted in Table I, are to develop the technology for an experimental power-train system that demonstrates the following: (1) the potential of a combined cycle fuel economy of 17.9 km/L (42.5 mpg) using diesel fuel No. 2 in a 1985 Pontiac Phoenix of 1364 kg (3000 lbm) weight on a 15°C (59°F) day; (2) emission levels less than federal standards; and (3) the ability to use a variety of fuels. It is intended that the technology demonstrated through this project would assist the automotive industry in making a go/no-go decision regarding the production engineering development of gas turbine power trains.

In meeting the project objectives, the engine will be designed to accomplish the following, also outlined in Table I: (1) achieve reliability and life comparable to conventional 1985 engines; (2) achieve initial and life-cycle power-train costs competitive with 1985 power trains; (3) demonstrate vehicle acceleration suitable for safety and maneuverability; and (4) meet 1985 federal vehicle noise and safety standards.

Initially, the project scope included the fabrication and chassis dynamometer testing of the engine, transmission, and electronic control system installed in a 1985 Pontiac Phoenix passenger car. However, Government funding constraints after the first year made it necessary to reduce the program scope. Activities eliminated included fabrication and testing of the transmission and vehicle. The electronic control scope was narrowed from that of controlling the engine, transmission, and vehicle to controlling an engine on a dynamometer. Figure 1 depicts the activity areas and schedule for the revised project.

Table I.
AGT 100 project and design objectives.

Project objectives:	System design objectives:
• 17.9 km/L (42.5 mpg) in 1985 Pontiac Phoenix	• comparable reliability and life
• alternate fuels capability	• competitive initial and life-cycle costs
• meet 1985 emission standards	• competitive accelerations
	• meets noise/safety standards

The AGT 100 design has been matched to the Pontiac Phoenix X-body car, shown in Figure 2. A front-wheel drive car, the Phoenix represents the current generation of advanced passenger cars, emphasizing efficiency of space and weight to combine comfort and function with high fuel economy. The AGT 100 will also fit into the Pontiac A6000, an A-body car that is slightly larger and is the latest GM front-wheel design with potential to replace the X-body car in the Pontiac future marketing of cars. The Fiero, a new Pontiac mid-engine personal car, can also accommodate the AGT 100 engine.

The AGT 100, shown in Figures 3 and 4, is a two-shaft, regenerative gas turbine engine. In all respects, this engine design is tailored for high-volume application to fuel-efficient passenger cars. Its two-shaft configuration allows (1) the use of conventional transmissions, manual or automatic, and (2) turbine tip speeds [approximately 503 m/s (1650 ft/sec)] commensurate with available ceramic material properties (strength and variability). Single-shaft configurations were rejected by Allison because of the corresponding requirement for a continuously variable transmission and for approximately 40% higher turbine rotor ceramic material strength (for equal reliability). Careful attention was given to component arrangement for both vehicle installation and management of potentially high heat losses. All hot-section components are grouped together, bounded on one end by the regenerator, on the other end by the gearbox, and enclosed by a well-insulated cylindrical case. High-cycle temperature is possible through the use of ceramic hot-section parts. This, coupled with high aerodynamic component efficiencies, produces low fuel consumption and a 50% improvement in composite miles per gallon (30% energy efficiency improvement) in a Pontiac Phoenix. Most importantly, the AGT 100 uses existing technologies for shafts, bearings, cases, control system, accessories, etc, and thereby provides a reliable test device for evaluating ceramic and aerodynamic components.

The main development challenges in the program are in building small, high-performance gas

ORIGINAL PAGE IS
OF POOR QUALITY

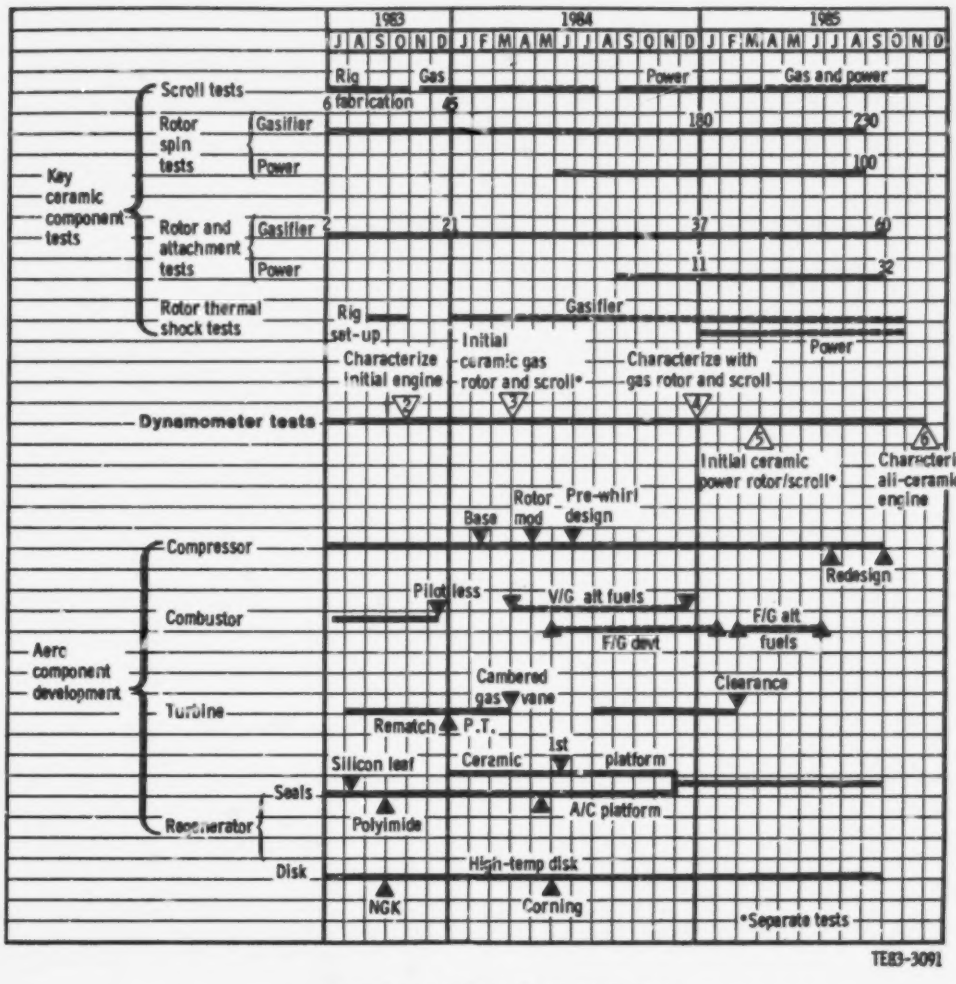

Figure 1. AGT 100 project plan.

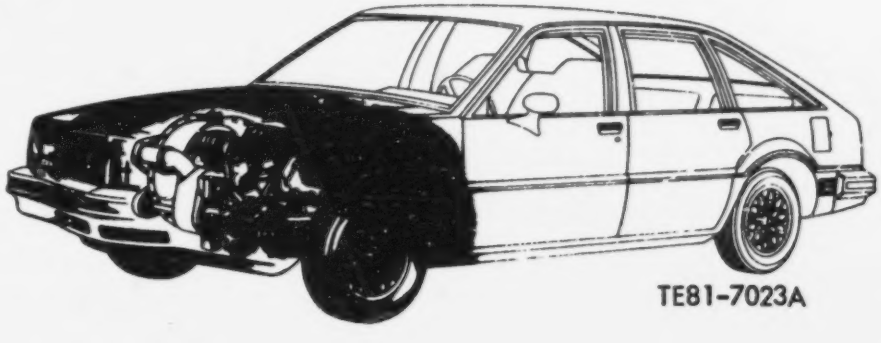

Figure 2. AGT 100 engine in 1985 Pontiac Phoenix.

ORIGINAL PAGE IS
OF POOR QUALITY

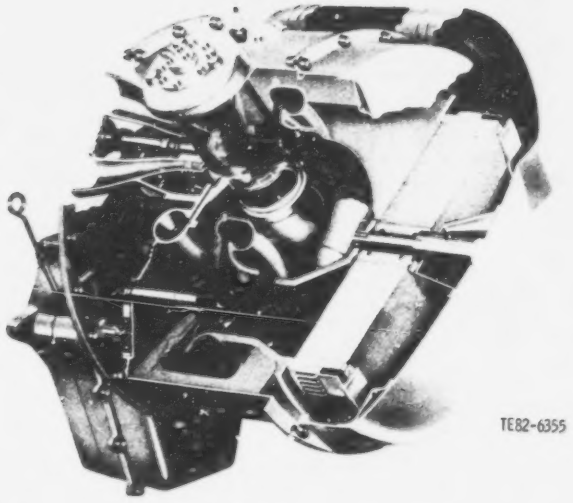

Figure 3. AGT 100 advanced gas turbine engine.

turbine components and developing ceramic components for the required high engine cycle temperatures that are price competitive and can be produced in an automotive production environment. The AGT 100 ceramic components are shown in Figure 5.

Because of the small-size engine [0.35 kg/s (0.76 lbm/sec) airflow], extensive rig testing, outlined in Table II, is being performed in component development. A major ceramic component development program is being pursued, and the ultimate success of the engine depends on the success of this activity.

Mechanical development of the engine is being conducted in two essential phases. The first incor-

Table II.
Aerodynamic component rigs.

Component	Builds	Hours
Compressor	5	286
Combustor	17	181
Turbines		
Gasifier	2	204
Power	1	26
Interturbine duct	3	239
Regenerator		
Cold side flow distribution	8	110
Hot side flow distribution	1	72
Seal leaf leakage	6	60
Hot simulator rig	4	480
Ceramic seal platform	Seven units	40
		1698

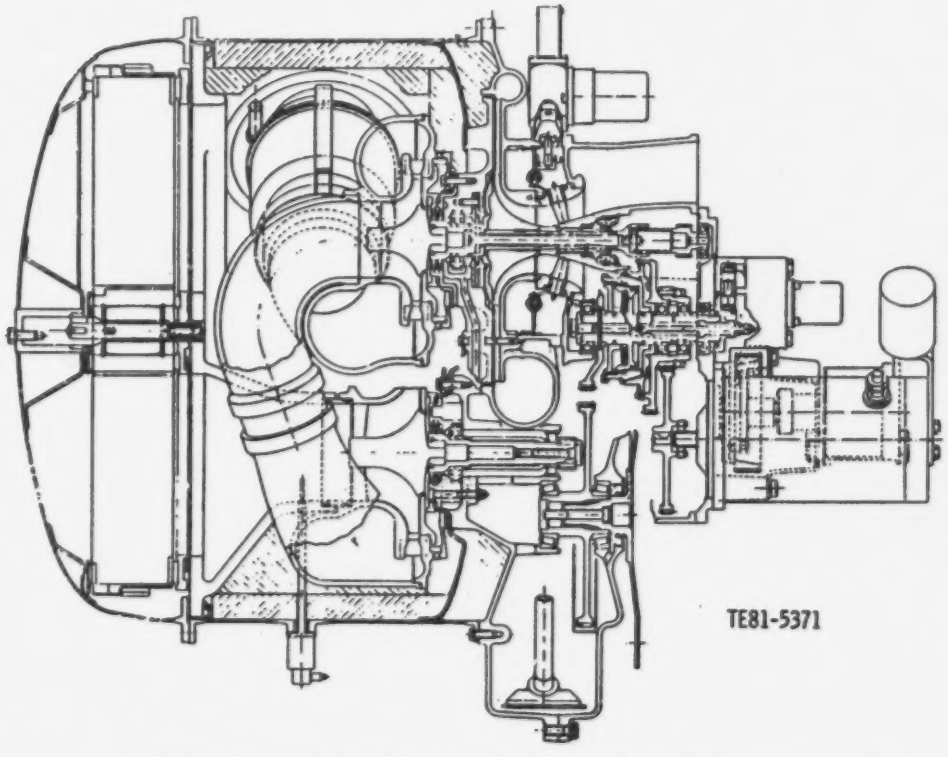

Figure 4. Cross section of AGT 100 gas turbine engine.

ORIGINAL PAGE IS
OF POOR QUALITY

porates early available ceramic components with metal substitutes for those components requiring further ceramics development. This phase includes metal turbine rotors and engine operation at 1080°C (1976°F) turbine inlet temperature. The second phase includes engine demonstration of all ceramic component types for 1288°C (2350°F) turbine inlet temperature. The transition from the first to second phase will occur in steps as each new ceramic component becomes available.

A team concept is used in this project, with many of the team members being General Motors Divisions. Allison is the prime contractor and team leader with responsibility for the overall power train and controls. Pontiac Motor Division (PMD) has vehicle design and cost analysis responsibility, and Delco Remy will develop the starter/boost system for the engine. The primary non-GM groups on the team are Carborundum Co (CBO), Corning Glass Works (CGW), and GTE Laboratories, Inc, who are involved in the ceramic effort.

This report is structured on a component basis (e.g., all work relating to the gasifier turbine rotor, including rig work and ceramic rotor development, is discussed as a part of the gasifier turbine section). Exceptions to this are functional areas that are not peculiar to any one major component: engine subsystems, cover structures, gearbox and power transfer, rotor bearings, shafts/seals, and secondary flow. There are separate sections for materials development and controls development.

Certain sections are omitted in this report because no effort was expended in those areas. These sections are identified in the Table of Contents to preserve continuity.

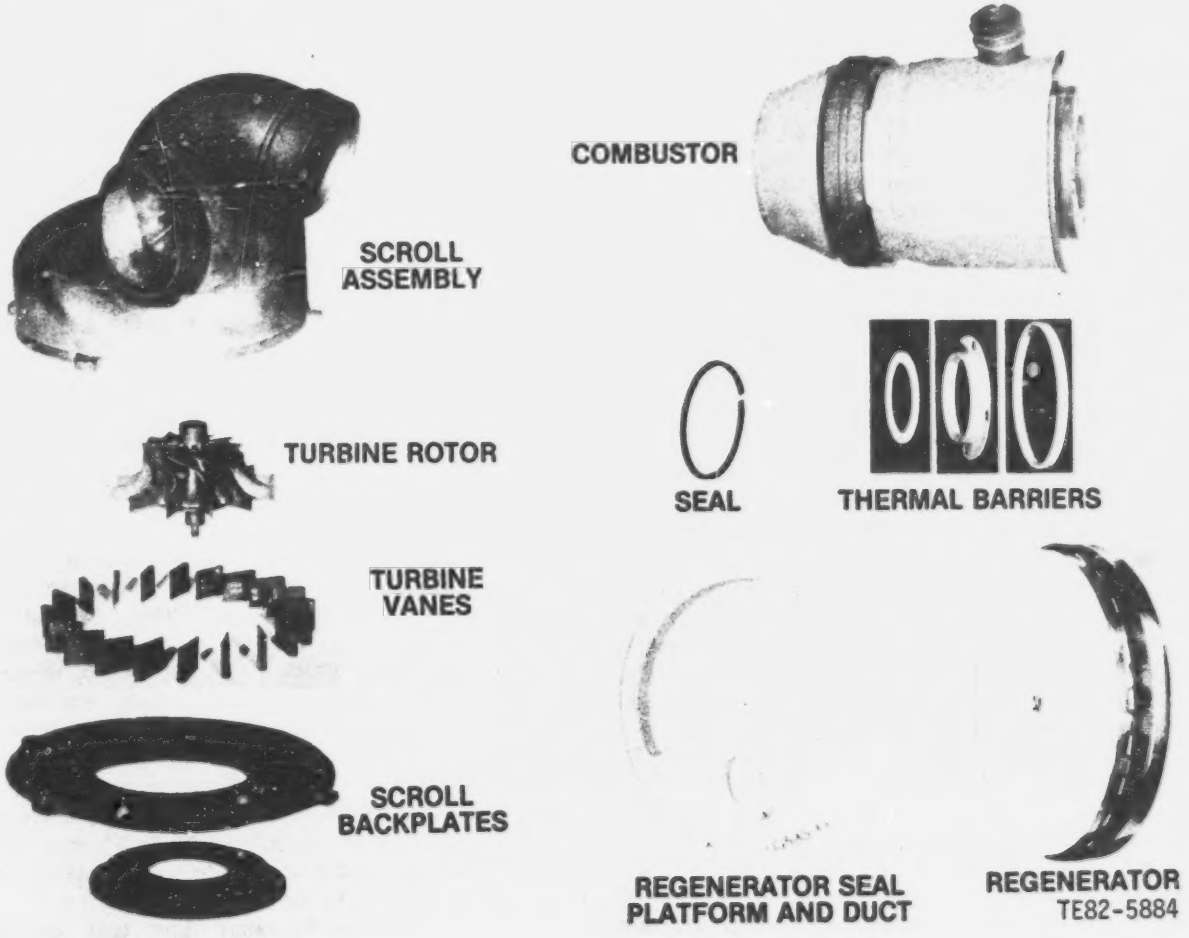

Figure 5. AGT 100 ceramic components.

II. ENGINE DEVELOPMENT

The goal of experimental engine development during this reporting period was to obtain performance data and to gain experience with durability testing for evaluation of mechanical systems. This goal supports the establishment of the AGT 100 engine as a credible machine for evaluation of ceramic components and for identification of engine interaction of components. The engine test program has been and continues to be one that yields early identification of ceramic component problems related to the engine environment and also other engine-related mechanical and aerodynamic problems. Component performance in the engine is determined for comparison with test rig results. The comparison provides guidance for future rig work. Engine testing also demonstrates control system adequacy.

One engine was used initially to accomplish normal shakedown activity. Use of this engine allowed a minimum of parts rework and was compatible with project funding. Most of the parts for a second engine were obtained with the initial engine, but many of them were not finished until initial engine running revealed the important clearances and/or adjustments that needed to be made to geometry, lubrication, and instrumentation systems. This phase was concluded with the completion of machining of parts for a second engine in May 1983. Subsequently, changes identified for either engine now have been incorporated into both. Testing of both the first and second engine took place during this period.

Each experimental AGT 100 engine has been serialized. The first was designated serial number (S/N) D-1, the second was labeled S/N D-2. In this report, each assembly of an engine is referred to as a build or buildup (BU) and each subsequent disassembly is referred to as a teardown (TD). For example, the eighth assembly is BU8; and when testing is completed, the corresponding teardown is TD8. A teardown is defined as occurring when a major splitline of the engine is separated.

2.2 EXPERIMENTAL ENGINE

This subsection is divided into three discussions: one on fabrication, one on testing, and one on test performance of the two engines during this reporting period.

2.2.1 Fabrication

Principal efforts during the second half of 1983 consisted of refurbishing engine-tested parts and fabricating hardware with design changes that provide improved durability or performance features. The changes defined as a result of engine testing are discussed in subsection 2.2.2.

Also, additional hardware has been ordered to improve compressor and turbine efficiency and matching. New compressor rotors with thinned blades have been ordered for aerodynamic rig testing and ultimate engine evaluation. A new gasifier scroll and backplate assembly will incorporate provisions for a new vane that will provide improved performance. Also, a new power turbine and backplate assembly to provide improved matching for the reduced temperature testing has been ordered. New gears will be used for matching at the new reduced speed required by the capacity change.

All of the ordered hardware is scheduled to be available in April 1984.

2.2.2 Experimental Engine Testing

At the beginning of this reporting period, one engine—S/N D-1—had been assembled and tested eight times; i.e., the test program had progressed through BU8. Total accumulated running time was 8 hr 58 min. Testing had been scheduled to accomplish running at increasing rotor speeds and had resulted in operation at 100% gasifier speed with BU8.

During the present reporting period, testing continued with the goal to identify engine-related mechanical and aerodynamic problems and engine component modifications necessary to improve engine operation, durability, and performance. Engine S/N D-1 was tested through BU10 while a second engine—S/N D-2—was activated and tested through BU2. During this reporting period, engine S/N D-1 was tested for 11 hr 42 min, for a total accumulated time of 20 hr 40 min, and engine S/N D-2 was operated for 20 hr 39 min. Engine test time in this reporting period totaled 32 hr 21 min; program total engine test time at the end of this reporting period was 41 hr 19 min.

Each build configuration and test accomplished in the present reporting period is discussed in the following pages.

Engine S/N D-1 BU9 and test. This build incorporated parts modified to accomplish the following:

- provide positive retention of the compliant seal between the combustor and the scroll to prevent loss of the seal during running
- provide positive retention of the turbine bearing carbon seals to prevent looseness due to thermal differentials
- increase radial clearance of the turbine bearing seals to reduce wear
- increase clearances at the combustor body to air-control bands of the variable geometry to reduce the potential for binding
- increase the compression on an O-ring seal at the compressor discharge to ensure no air leakage overboard at that point

In addition, a new combustor assembly was proof tested on the combustor rig for use in BU9, and the engine integral regenerator drive gearing was included.

The planned test program for BU9 consisted of obtaining performance data throughout the speed range plus accumulating additional running time for durability experience, to be followed by the injection of powder to aid in establishing air leakage paths. Early in the running program, main burner flameouts resulted from the pilot flame going out. Subsequent starts with sustained running were made by remaining on the start-fuel nozzle until burner inlet temperature (BIT) reached 760°C (1400°F), the temperature at which main burner does not require a pilot flame to maintain combustion.

Steady-state data were obtained at lower speeds. At gasifier speeds above 70%, vibration levels rose to higher levels than had been experienced previously. At speeds a little above 70%, accelerometers at the compressor inlet plane responded. Analysis showed this to be a low frequency (400 Hz) response attributable to a case mode, and the levels of displacement measured were not considered significant for that frequency.

At about 80% speed on the gasifier, accelerometers at several stations on the engine recorded vibration levels at rotational frequency that were beyond a specified limit of 16.5 mm/s (0.65 in./sec) velocity. Shaft whip was not excessive.

An investigation was made to determine if a change in the regenerator drive method incorporated in this build had produced the vibration. Engine BU9 used the integral internal engine drive gears to drive the regenerator. Prior testing had utilized an external chain drive. The effect of this change on the vibration was investigated in two steps. First, the test stand drive chain was reinstalled but allowed to freewheel during engine running to duplicate the inherent side load from the chain on the regenerator drive shaft. In further testing, although higher speeds were reached, vibration levels were still too high. Second, the internal engine regenerator drive system was disconnected by removing a gear set. With the test stand drive system then used to rotate the regenerator, the drive system was returned completely to that used in all previous tests. A test run with this drive configuration was terminated when performance data indicated excessive flow-path leakage. A borescope examination showed that the ceramic-regenerator bulkhead was broken at its upstream or power turbine end.

The engine was removed from the test stand, and the regenerator and ceramic bulkheads were removed. No other distress was found in this area. The failure of the bulkhead appeared to be due to a sideload imposed at the turbine end where the turbine-to-bulkhead coupling is located. This load was oriented so the problem could have been due to radial thermal growth of the power turbine transmitted through a coupling that did not realign because of excessive friction.

The engine run time for BU9 was 10 hr 44 min. Total engine run time accumulated was 19 hr 42 min.

Engine S/N D-1 BU10 and test. The engine was reassembled with the addition of a new ceramic bulkhead. The bulkhead was installed so it was displaced radially outward from the power turbine scroll to provide extra allowance for turbine scroll thermal expansion. The gearbox cover was removed so the gasifier pinion shaft could be removed and reindexed. Runout of this shaft was improved from 0.063 mm (0.0025 in.) to 0.025 mm (0.001 in.) with the expectation that some unbalance would be relieved. No other disassembly was done prior to additional testing of the BU10 engine.

Operation of the engine at speeds above 80% again produced excessive vibration. Further running was limited to that necessary to implement an air leakage detection test.

Fine powders were injected into the engine at two locations: (1) the compressor inlet and (2) the air tube between the compressor and the regenerator. A blue powder—cobalt aluminum chromium—was injected at the compressor inlet and a white powder—titanium dioxide—was injected into the air tube. The use of two colors was expected to assist in tracing the source of air leakage.

Teardown of the engine proceeded slowly with examination and photographs taken concurrently

to record the leak detection powder traces. While quantitative evaluation of gas leakage from powder traces would be judgmental, location of leakages was detectable. In general, very little overboard leakage was found. No splitlines leaked, but small powder traces indicated leakage at an instrumentation sealing point and at the seal where the burner variable geometry actuator arm penetrates the combustor case. Internally, leakage traces were found at piston rings and at the ceramic insulating spacer ring on the gasifier scroll support.

The largest powder trace was found in the cavity between the hot and cold engine sections. Leakage there was from the sealed holes penetrating the combustor case through which spring-loaded rods pass to retain the scrolls. Three of eight such locations showed significant powder traces. The seal was found to be missing from one of the three.

Disassembly revealed that the ceramic bulkhead was broken at the power turbine coupling position. The break occurred in much the same location as on the previous build.

In addition, the following conditions were found on teardown:

1. The carbon seal behind the impeller rubbed the gasifier rotor shaft. This was found to be due to excess shaft excursion permitted by an out-of-print bearing mass isolator.
2. One scroll hold-down spring set had yielded to its minimum operating length; six others were shorter than print. The collapsed spring set was from the position where the seal was missing.
3. A tooth was chipped on the power transfer clutch gasifier gear. Metallurgical examination revealed an inclusion as the source of breakage.
4. The gasifier turbine carbon seal showed distress on the turbine side. Seals with higher temperature carbon material will be obtained.

Post-test investigation of the vibration that occurred on BU9 and BU10 revealed that the gasifier rotor was significantly out of balance. Further, the bearing mass isolator spring bars were out of print, which resulted in an inability to accommodate out-of-balance forces.

The cause of the unbalance is being studied. As with most turbine engine designs, a rotor disassembly is required after balance is obtained for reassembly in the engine. This provides an opportunity for undetected unbalance to occur. To moderate the effect of any excess unbalance, a viscous vibration damper to be mounted at the cold end gasifier bearing location was designed and fabricated.

The breakage of the ceramic bulkhead is believed to be due to a greater thermal misalignment between the bulkhead and power turbine than could be accommodated by the coupling. A design modification was made that lengthened the coupling and increased diametrical clearances. This change resulted in a coupling connection that will accommodate 230% more bulkhead-to-turbine misalignment.

Running time for BU10 was 58 min, for a total accumulated running time on S/N D-1 engine of 20 hr 40 min.

Engine S/N D-1 BU 11 preparation. Through the remainder of this reporting period, design modifications and parts rework were under way to prepare for the next test. As mentioned, a viscous vibration damper was designed and fabricated for installation at the No. 2 bearing (compressor) location. New mass isolator spring bars were fabricated for both the gasifier and power turbine bearing locations. At the gasifier turbine bearing location, two of the mass isolator spring bars were instrumented with strain gages. These gages were calibrated so a shaft displacement (whip) signal could be obtained during running.

Engine S/N D-1, BU11 will incorporate the reworked ceramic regenerator bulkhead and increased length coupling to allow greater misalignment between the bulkhead and power turbine. The gasifier turbine metal vane set will be replaced, due to erosion, with a new set that will include two ceramic vanes.

Testing of engine S/N D-2 reported in the next subsection revealed further loss of air seals at the scroll hold-down rods. These graphite seals will be replaced on engine S/N D-1, BU11 with metal seals.

In an effort to better define compressor performance, instrumentation is being added just downstream of the impeller to assist in identifying heat loss between the impeller and the normal compressor outlet measuring position. Running clearance of the impeller and of the power turbine will be reduced somewhat for improved performance.

Engine S/N D-2 BU1 and test. A new engine (S/N D-2) was assembled and tested during this reporting period. The BU1 configuration was the same as engine S/N D-1, BU9, except that the flow capacities of both turbines were matched to the original 1080°C (1976°F) turbine inlet temperature (TIT) cycle. (Engine S/N D-1, originally similarly matched, had been rematched by BU9.) In addition

the ceramic bulkhead was reworked to accommodate the new design power-turbine-to-bulkhead coupling.

The goal of the test program was to explore both mechanical operation and performance throughout the speed range.

Simple motoring tests to 50% gasifier speed showed no problem. The engine was then started successfully. Performance data, as well as data for mechanical assessment, were obtained at various combinations of speeds from 60% to 70% on the gasifier and 30% to 70% on the power turbine (output shaft). This initial run lasted 4 hr 24 min.

Following the second start, performance data indicated that a substantial leak from the flow path had developed. The engine was removed from the test stand. Removal of the engine regenerator revealed severe wear on the regenerator hot seal and a large amount of oil in the regenerator housing.

The worn seal was attributed to contact between the regenerator disk rim cement and excessive plasma-spray material used to retain the carbon wear face on the seal. The cement dust produced is highly abrasive, resulting in considerable carbon material removal. The seal was removed for repair, and the regenerator disk was judged acceptable for further use.

The oil found in the regenerator housing was representative of a relatively large loss of oil during operation. Considerable oil was found at the compressor inlet. The gearbox had been vented to the compressor inlet, and this engine build was the first to make use of the oil/air separator built into the gearbox to prevent entrained oil from being introduced into the flow path. Plugging the vent was planned for the next build.

Running time for this first build of engine S/N D-2 was 4 hr 33 min.

Engine S/N D-2 BU2 and test. The regenerator and seal assembly was replaced with the one from engine S/N D-1, the gearbox vent to compressor inlet was plugged, and the engine returned to test.

Early running produced a continuation of a problem first encountered to a significant degree on engine S/N D-1, BU9. The pilot nozzle flamed out after combustion lightoff. This required making start-fuel nozzle to main-fuel nozzle transitions at 760°C (1400°F) BIT, instead of at the 480°C (900°F) previously used. After 6 hr of operation the pilot fuel nozzle had carboned to essentially full plugging of the pilot orifice. With the current engine fuel system, this plugging results in loss of fuel flow control with the flow going to maximum, requiring engine shutdown. The fuel system was rearranged so that the pilot fuel could be dumped overboard on manual control and testing could continue. New fuel system hardware undergoing bench testing will not have the characteristic of full fuel flow occurring when the pilot nozzle is plugged.

A change also was made to the main nozzle fuel purge procedure. To this point, purging (on shutdown) had been to overboard using flow-path pressure. Partial plugging of the main nozzle has resulted from fuel coking in the small nozzle orifices. In this period, the procedure was reversed to purge back into the engine on shutdown using test-stand air pressure regulated above compressor discharge pressure.

As running continued, several instances of combustor flameout occurred. Examination of data indicated the probability of lean blow out (LBO). The burner variable geometry (BVG) schedule was modified to richen the primary zone by an overall BVG position bias of 2.54 mm (0.1 in.). Further running at 60% and 70% N_1 speed was uneventful; however, as speed was increased to 80%, a combustor flashback occurred. This was a result of being too rich in the primary zone, producing combustion in the prevaporization chamber, which was detected by thermocouples in that area.

The experience indicated that a further tailoring of the BVG schedule was required. The fixed bias was eliminated and the basic schedule modified for BIT below 960°C (1400°F).

The engine was taken to 80% N_1, 80% N_2. At that speed the pressure in the insulated, vented cavity between the hot and cold engine section rose to 112 kPa (16 lb/in.^{2}) gage pressure. Data were acquired at that operating condition and the engine shutdown.

This pressure had been carefully monitored. On S/N D-1 pressure had been permitted to go to 175 kPa (25 lb/in.^{2}) gage. Teardown revealed that the eight graphite ball seals at the scroll hold-down springs had allowed leakage of burner inlet air into the cavity. During early running on S/N D-2, this cavity pressure was very low. At subsequent times, at comparable operating conditions, the pressure was higher. A look at representative values of this pressure throughout the running showed definite periodic changes in the pressure, indicating that the seals failed one by one.

The pressure level was considered undesirably high, and the test program was terminated. A further low speed run was made to inject an air leak tracer powder into the flow path, and the engine was removed from the stand.

Teardown inspection showed two of the eight graphite ball seals, those closest to the burner, had oxidized to disappearance. A solution for the ball seal failures will be the substitution of seals made from Haynes 188 material.

A small crack at the outer diameter (o.d.) of the compressor inducer was blended out. An oil leak from the gearbox into the flow path ahead of the compressor due to a warped casting splitline was corrected with an O-ring. No significant leakage was indicated by powder traces. The gasifier turbine carbon seal was broken, and the power turbine seal had deteriorated. This recurring problem (low temperature capability) was already identified, and high-temperature replacement seals have been ordered. Also for the next build some cooling air will be directed to the hot side of the gasifier turbine seal.

Testing of the S/N D-2 engine has shown a decrease in combustor operating range between LBO and flashback. Data defining these conditions were generated on the combustor rig subsequent to the engine test. Increased incidence of LBO is thought to be due to the lack of a pilot flame. With improved definition of LBO and flashback from combustor rig data, a new schedule for the BVG will be incorporated into the electronic control unit for the next run.

Running time on this build was 16 hr 6 min for a total time on S/N D-2 engine of 20 hr 39 min. Total accumulated time for engines S/N D-1 and S/N D-2 was 41 hr 19 min at the end of this reporting period. A plot showing engine test hours accumulation by build number is shown in Figure 6.

Engine S/N D-2 BU3 preparation. Through the end of this reporting period, modifications were in process to prepare for the next test. The primary change was the replacement of the graphite ball seals at the scroll hold-down springs with metal ones. In addition, carbon shaft seals were replaced and the compressor inlet splitline was sealed with an O-ring.

At the end of this reporting period, assembly of the engine was under way.

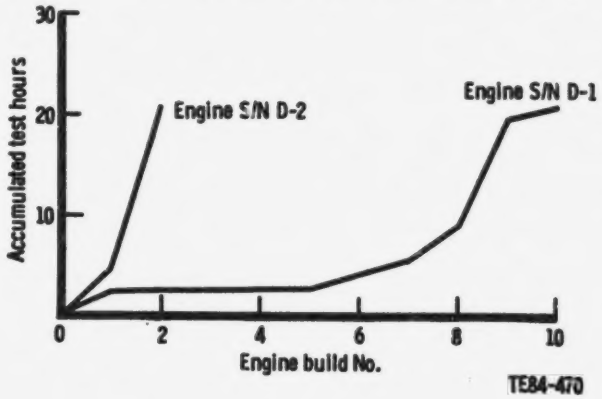

Figure 6. AGT 100 engine test hours.

2.2.3 Performance Analysis

During the reporting period, experimental testing was conducted on engine S/N D-1, BU9 and BU10, and on engine S/N D-2, BU1 and BU2. Data analysis consisted of comparing the performance of S/N D-1, BU9 with S/N D-1, BU8 performance reported in the Seventh Semiannual Report, NASA CR-174629 (EDR 11577), and comparing the performance of engine S/N D-2 with S/N D-1. Teardown of engine S/N D-1, BU10 revealed the failure of the ceramic regenerator bulkhead that resulted in a large leak path bypassing the combustor and both turbines. Data from S/N D-1, BU10, therefore, is not included as part of this performance analysis.

Because of the many combinations of rotor speeds, turbine inlet temperature, and starter-input power during engine testing, a meaningful comparison of performance could only be made using the performance computer model adjusted to match engine S/N D-1, BU8 data record number 11163. The discussion in EDR 11577 of the adjusted performance computer model is applicable.

Simulations of test data points from engine S/N D-1, BU8 and BU9, and engine S/N D-2, BU1 and BU2, were made at observed test conditions of air inlet pressure and temperature, compressor inlet guide vane setting, rotor speeds, and starter input power. Key performance parameters of net power (dynamometer power less starter input power), fuel rate, compressor airflow, and compressor pressure ratio from the simulations were plotted versus the same observed performance parameters as shown in Figures 7 through 10. Different symbols were used to distinguish the engines and builds. The shaded symbol indicates the adjusted performance model match point.

Deviation of the points from the labeled zero error line indicates the degree of error between the computer model and the observed data. These errors are expected to be reduced by further model adjustments based on gasifier and power turbine nozzle flow calibrations and mechanical loss data that will be obtained on subsequent builds of the engine.

Lines were drawn on the comparison plots that best fit data from each of the engines. Minimal data scatter of the two engine builds of each engine

ORIGINAL PAGE IS
OF POOR QUALITY

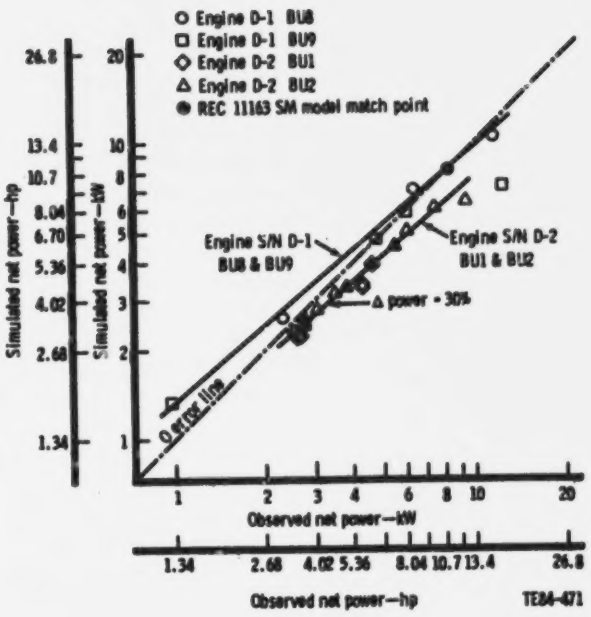

Figure 7. AGT 100 performance comparison of net power.

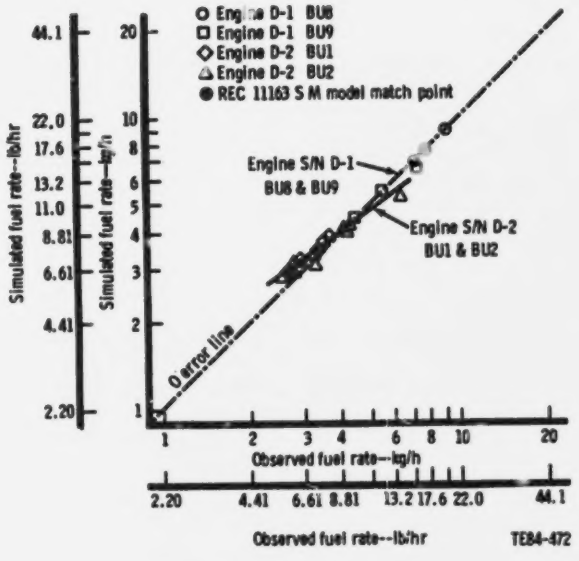

Figure 8. AGT 100 performance comparison of fuel rate.

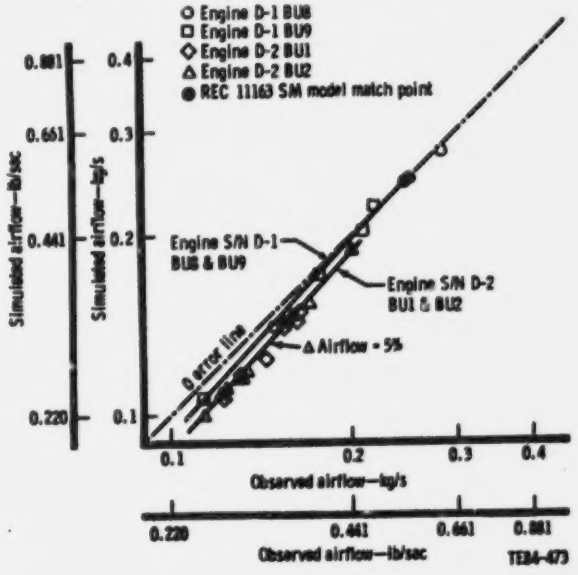

Figure 9. AGT 100 performance comparison of airflow.

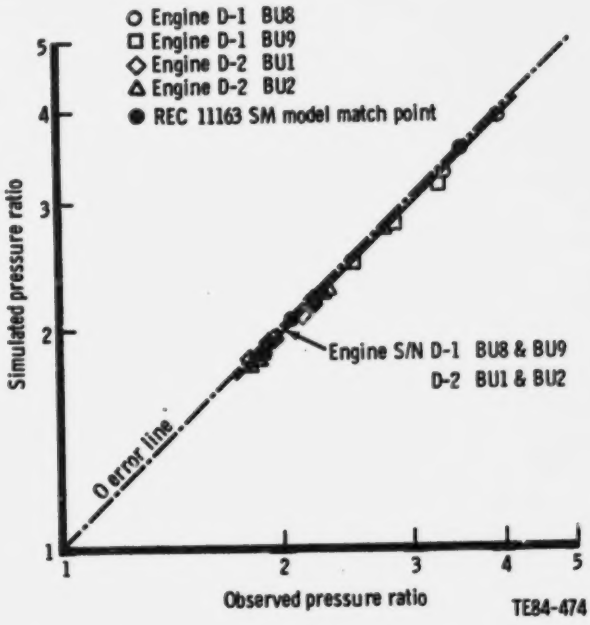

Figure 10. AGT 100 performance comparison of pressure ratio.

around the respective engine line indicated a constancy of performance between BU8 and BU9 of engine S/N D-1 and between BU1 and BU2 of engine S/N D-2.

A comparison of engine S/N D-2 performance with engine S/N D-1 performance at constant simulated parameter level showed the following:

- The net power of engine S/N D-2 was 30% greater than that of engine S/N D-1 at all power levels within the test range of engine S/N D-2.
- The fuel rate of engine S/N D-2 was greater than that of engine S/N D-1 at test fuel rates greater than 3.86 kg/h (8.55 lb/hr). At test fuel rates less than 3.86 kg/h (8.5 lb/hr), the fuel rate of engine S/N D-2 was less than that of engine S/N D-1.
- The airflow of engine S/N D-2 was 5% greater than that of engine S/N D-1 at all airflow levels within the test range of engine S/N D-2.
- There was no significant pressure ratio difference between engine S/N D-1 and engine S/N D-2.

Data analysis to date has been based on predicted values of flow leakage, and matching the computer model to observed data has resulted in mechanical losses and heat rejection rates several times higher than estimated values. Future builds of engine S/N D-1 will include flow calibrations of both turbine nozzles as a function of nozzle vane inlet to exit static pressure ratios.

The flow calibrations in conjunction with static pressure data obtained during normal engine testing will be used to define turbine flow capacities. Gasifier turbine flow capacity relative to measured compressor inlet flow and power turbine flow capacity relative to gasifier flow capacity will more accurately define actual flow leakage ahead of and behind the gasifier turbine, respectively. A motoring test of the mechanical system without a compressor impeller using bladeless turbine rotors will be used to calibrate the gearbox mechanical loss as a function of rotor speeds and oil temperature.

Using these data, data analysis of future engine test data is expected to result in a high degree of confidence in determining component performance at engine operating conditions.

III. COMPRESSOR DEVELOPMENT

The AGT 100 compressor development efforts in the reporting period were concentrated in three major areas:

1. aerodynamic design and evaluation studies
2. compressor rig design
3. mechanical development of the compressor

3.1 COMPRESSOR AERODYNAMIC DEVELOPMENT

Aerodynamic development was directed toward design of two compressor configurations for evaluation of impeller passage diffusion [area equivalent ratio (AREQ)] effects and design studies for evaluation of alternate compressor configurations.

3.1.1 Task 1—Effect of Impeller Diffusion Levels (AREQ)

A preliminary design study indicated potential positive effects of reduced impeller AREQ on compressor efficiency. With impeller static pressure recovery held constant, a potential increase in efficiency of 14% resulted from a reduction in AREQ from 2.37 to 1.93. In this reporting period, two new impeller configurations were designed to evaluate AREQ effects. The two configurations were designed so they could both be obtained from existing, same-size impeller blanks as shown in Figure 11.

The primary purpose for these configurations was to evaluate AREQ effects; however, in light of further design studies, other areas of potential improvement have been addressed as well. Equilibrium flow analysis of the baseline impeller (BU3) indicated the impeller knee region was slightly low in flow area. This was addressed in the new designs as shown in Figure 12 by recontouring the shrouds. The new configurations resulted in improved shroud diffusion characteristics as shown in Figure 12.

Engine test data have consistently shown the compressor flow capacity to be lower than that measured in previous compressor rigs. The new designs have incorporated an increased flow capacity of 5%. This increased flow capacity was accounted for by the following:

- reduced impeller blade thickness (based on BU3 versus BU5 rig data)
- increased diffuser throat area
- slight increase in impeller outer diameter

The impeller blade thickness distribution shown in Figure 13 was selected to minimize losses in the inducer region. In a compressor such as the AGT 100 where the inducer is transonic, critical Mach number effects significantly contribute to inducer losses. The blade thickness was also reduced at the exit to reduce impeller exit blockage and resulting dump/mixing losses. A new diffuser was designed to operate with both impellers—narrow (type 1A impeller) and wide (type 1B impeller) exit widths. The diffuser throat area was maintained essentially the same as that on the engine rig, but the leading edge of the diffuser was moved radially outward by 0.147 cm (0.058 in.) to ensure the proper impeller to diffuser gap with the type 1A impeller. The same diffuser will be used with the type 1B impeller by modifying the vaneless space entry region and operating with a slightly higher vaneless space radius ratio (10.1% as compared to 8.4% for the type 1A impeller). Table III summarizes a comparison of the salient geometric variables of the current engine impeller and the two newly designed impellers.

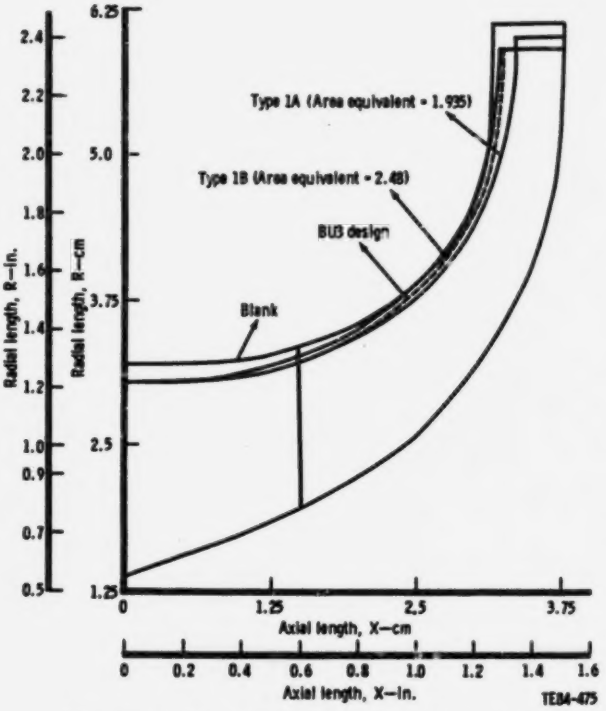

Figure 11. Meridional flow-path elevation.

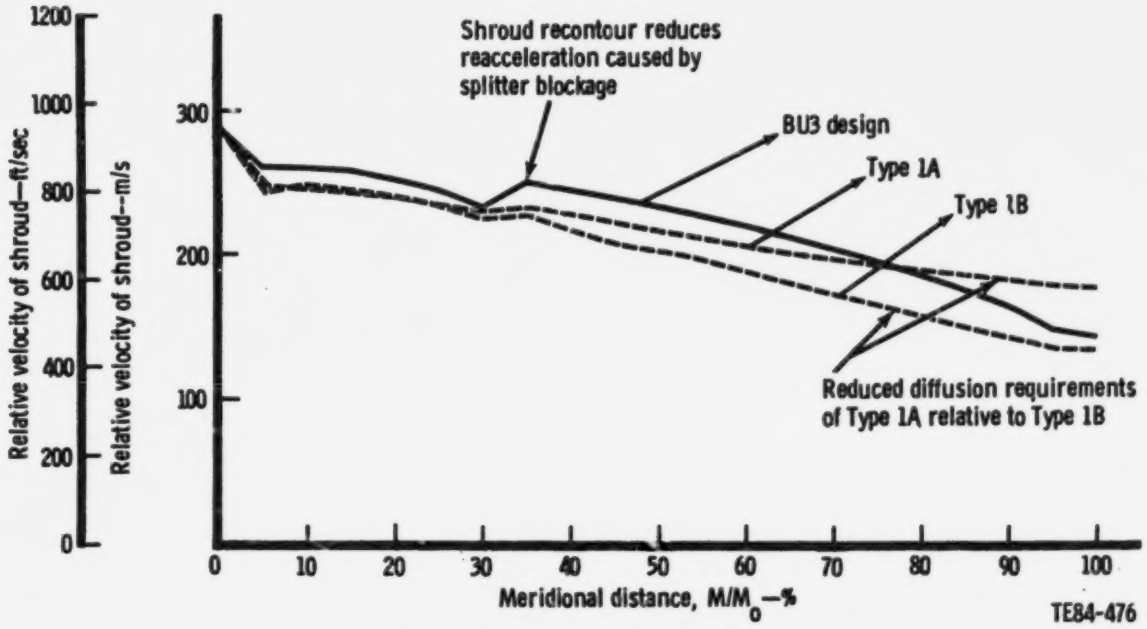
Relative velocity of shroud—ft/sec
Relative velocity of shroud--m/s
Shroud recontour reduces reacceleration caused by splitter blockage
BU3 design
Type 1A
Type 1B
Reduced diffusion requirements of Type 1A relative to Type 1B
Meridional distance, M/M0—%
TE84-476

Figure 12. Impeller shroud diffusion.

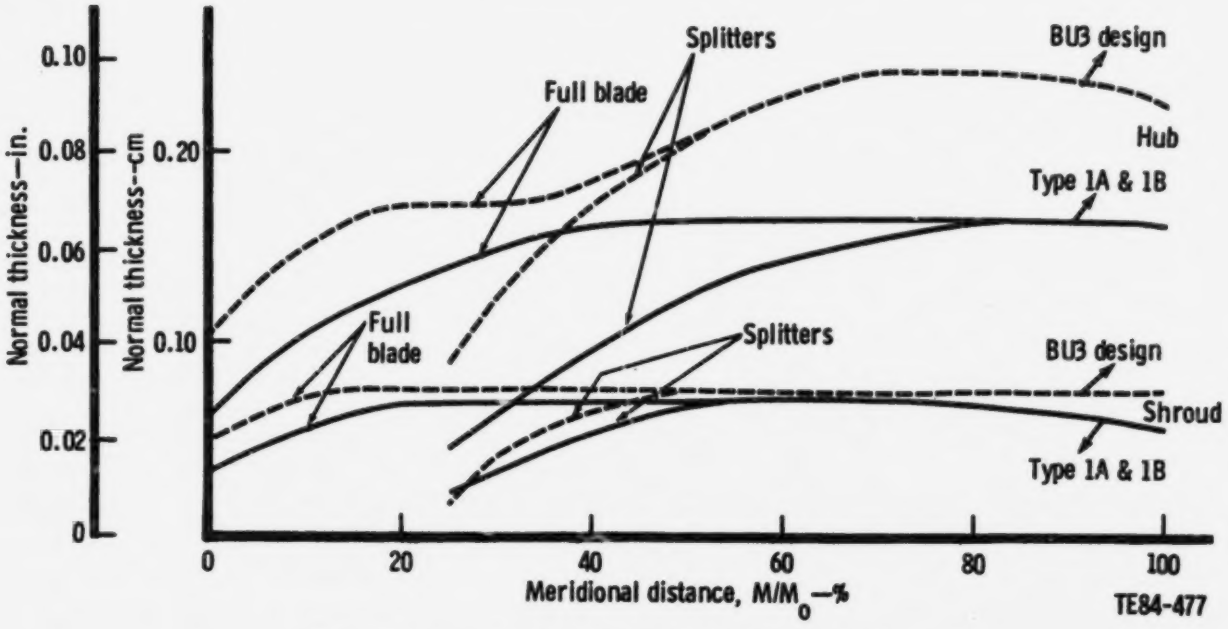

Figure 13. Impeller blade normal thickness distribution.

3.1.2 Task 2—Alternate Impeller Designs

Data obtained from the AGT 100 compressor rig tests have indicated that the key to higher efficiency levels is improved impeller performance, as described under Task 1, which is directed toward a quantitative evaluation of one of the primary design parameters—AREQ. The second phase of compressor development is also aimed at impeller performance and is structured to evaluate alternate design concepts. Currently, two different approaches have been adopted to analytically determine the most promising concept to carry on to the hardware/testing phase of the program.

Table III.
Comparison of impeller geometric variables.

	Current engine (BU3 type)	Narrow impeller (type 1A)	Wide impeller (type 1B)
$R_{1\ hub}$—cm (in.)	1.4 (0.551)	1.4 (0.551)	1.4 (0.551)
$R_{1\ tip}$—cm (in.)	3.11 (1.224)	3.11 (1.224)	3.11 (1.224)
$R_{2\ exit}$—cm (in.)	6.00 (2.365)	6.12 (2.410)	6.03 (2.373)
$B_{2\ exit}$—cm (in.)	0.554 (0.218)	0.427 (0.168)	0.554 (0.218)
$B_{2\ blade}$—deg	50.00	51.1	50.2
Average exit T_{noz}—cm (in.)	0.152 (0.060)	0.112 (0.044)	0.112 (0.044)
Number of blades, splitter/full	16/32	16/32	16/32
R_3 diffuser inlet—cm (in.)	6.488 (2.554)	6.634 (2.612)	6.634 (2.612)
b_4 diffuser throat width—cm (in.)	0.427 (0.168)	0.427 (0.168)	0.427 (0.168)
W_4 diffuser throat—cm (in.)	0.472 (0.186)	0.475 (0.187)	0.475 (0.187)
Number of vanes	21	21	21
Area ratio	4.04	3.953	3.953

The first concept incorporates prewhirl at the design point. The advantage of prewhirl is that it reduces inlet Mach number thereby reducing losses and required incidence for a given choke margin that reduces part-speed stall losses.

The second concept employs axial entry to the compressor but with a reduced number of blades in the inducer region (8 versus 16 in the current design). The lower number of blades in the inducer region reduces mechanical blockage resulting in lower inducer incidence for a given choke margin. Also, the lower number of blades increases passage hydraulic diameter minimizing passage frictional losses. Splitters were introduced at 30% and again at 55% meridional distances to reduce losses associated with blade loading.

Impellers utilizing the two concepts mentioned have been incorporated in a preliminary design and are being evaluated to determine the best concept.

3.2 COMPRESSOR RIG MECHANICAL DEVELOPMENT

The mechanical development of the compressor rig has been an on-going process throughout this program. However, during this work period, special emphasis has been placed on the modification of the compressor rig to address the following:

- interchangeability of compressor hardware between engine and compressor rigs
- minimizing discrepancies in performance evaluation due to rig sensitivity to environmental effects

The compressor rig, shown in Figure 14, was designed to accept engine hardware and thus to allow the testing of the engine compressor in the rig. To accommodate this, hardware on the rig was redesigned to ensure structural integrity. The modification of the rig also incorporated the ability to balance the rotor system during the buildup process without involving a teardown of the assembly. Since impeller shroud clearance strongly influences both impeller flow capacity and performance, a screw-thread arrangement has also been incorporated to vary shroud clearance up to 0.076 cm (0.030 in.) without rig teardown. This will enable the evaluation of an optimum running clearance within reasonable mechanical limits.

In a low flow compressor such as the AGT 100, small amounts of heat transfer to and from the environment (i.e., lubricating oil) have a significant influence on compressor performance. The sensitivities of the compressor to the environment are such that the following are true:

- At idle (50% speed), a 0.56°C (1°F) change in compressor temperature alters the calculated efficiency by one point.
- At maximum power, a 0.56°C (1°F) change in temperature affects the calculated efficiency by 0.3 points.

In view of this, a thorough heat transfer analysis was carried out to evaluate the effects of lubricating oil temperature in the front and rear bearings and heat transfer between air and the impeller. The results of the analysis revealed the following:

- Net heat transfer effects between the air and impeller were small and were less than 0.3% for all cases.
- The original design had high heat losses to the rear bearing and was sensitive to rear bearing oil temperature. This was in agreement with rig test data.

To address the significant heat transfer effects, the modification of the rig has incorporated the following design features:

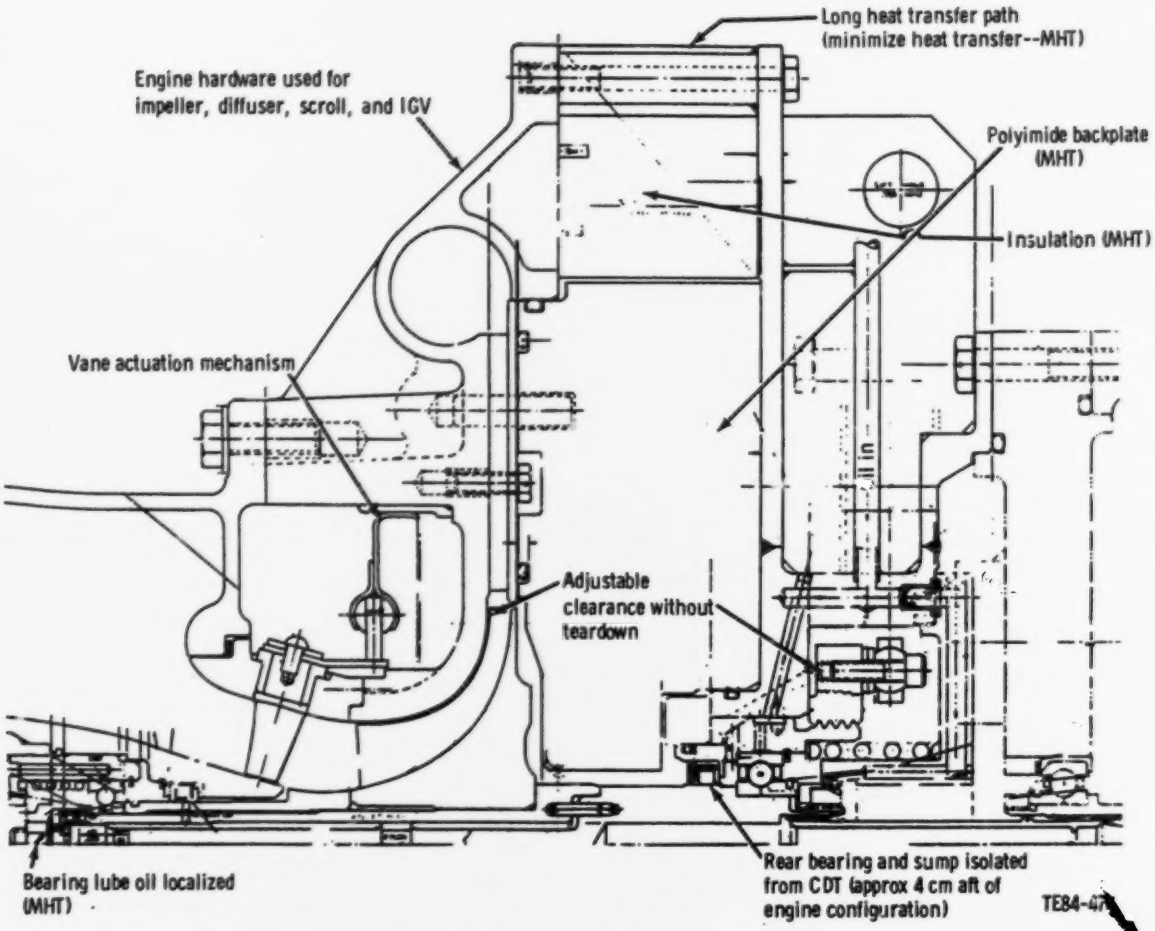

Figure 14. Cross section of modified compressor rig.

- The rear bearing has been moved 3.81 cm (1 1/2 in.) aft to isolate the rear bearing and its oil system.
- The backplate has been replaced by one made of polyimide and epoxy filled with glass microballoons. This material has low heat transfer and thermal capacity properties that further insulate the compressor from the rear bearing and its oil system.
- Insulating material has been added to isolate all hot sections from cold sections within reasonable limits.

Incorporation of the changes mentioned in the analytical model revealed a significant reduction in heat losses to external heat sinks (oil and ambient air); these changes should improve the measurement of compressor efficiency.

3.3 COMPRESSOR MECHANICAL DEVELOPMENT

Compressor mechanical development during this period consisted of evaluating engine running clearances and the release of a compressor design with thinned blades. Rub pins (mounds of epoxy) were used to acquire compressor running clearance measurements, and wax was used to obtain cold clearance measurements at buildup and teardown. Rub pin locations and the techniques used to obtain the cold wax measurements are described in the Seventh Semiannual Report (EDR 11577).

Cold wax goals and measurements and rub pin measurements for engine S/N D-1, BU9 through BU11 are shown in Table IV. Measurements for TD9 and BU10 are not available since the cold section of the engine has not yet been disassembled.

The cold wax goals and measured values appeared consistent. Rub pin measurements for TD10 indicated some rub pins in the knee and tip areas were not touched during running. The measured rub pin values indicated clearances slightly open as compared with previous data, although a similar occurrence was observed at TD8. This trend will be watched closely during future tests.

Additional thinning was done to the compressor impeller on engine S/N D-1 for BU9. As previously reported, the full blades and splitters were thinned for BU8 by removing metal from the suction surface only. The purpose of this thinning was to improve compressor airflow, pressure ratio, and efficiency previously seen in compressor rig test data. This thinning did not result in any significant gains in airflow, pressure ratio, or efficiency. For BU9, the full blade leading edges were thinned further in an attempt to improve high-speed compressor efficiency. This additional thinning did not show any significant improvement in efficiency, possibly because N_1 speed during BU9 and BU10 did not exceed 75%.

The compressor impeller used on engine S/N D-2 is the same configuration as the one used on engine S/N D-1, BU8. The full blades and splitters have been thinned by removing metal from the suction side only as described in EDR 11577. The leading edges of the full blades were not thinned further as was done on engine S/N D-1, BU9.

Cold wax goals and measurements and rub pin measurements for engine S/N D-2, BU1 through TD2 are shown in Table V. The cold wax measurement goals for engine S/N D-2, BU1 were the same as for engine S/N D-1, BU9 and BU11. Rub pin locations for engine S/N D-2 were the same as for engine S/N D-1.

No measurements were available for TD1 and BU2 since the cold section was not disassembled. Cold wax measurements at the inducer for BU1 indicated the clearance was 0.00635 to 0.0127 cm (0.0025 to 0.005 in.). These were about half of the desired values of 0.0127 to 0.02413 cm (0.005 to 0.0095 in.). The decision was made to proceed with these values since no high-speed running was expected. Table V indicates a light rub was experienced in the inducer region during either BU1 or BU2 running. TD2 cold wax measurements, as compared with BU1 cold wax measurements, indicate the cold clearance between the impeller and shroud at the inducer has opened slightly due to the rub. A small crack at the o.d. of one of the impeller blades near the inducer was observed at TD2. This crack was successfully blended out. The same impeller will be used on BU3 of engine S/N D-2.

Inspection charts of engine test impellers indicate extra thickness on both full blades and splitters. The results of a previous compressor rig test (rig BU5) showed increases in airflow, pressure ratio, and efficiency as a result of thinning compressor blades. The thinned impellers tested on BU8 and BU9 of engine S/N D-1 did not achieve performance levels similar to those demonstrated on the compressor rig. This was probably because the blades on the engine-tested impeller were not thinned as much as those on the rig-tested impeller.

A new impeller design, which has airfoil angles and contours similar to the present (baseline) impeller, was released during this reporting period. The airfoils in the new type 1A and 1B designs are thinner than those in both the present (baseline) design and a thinned rig test impeller (rig BU5), as shown in Figure 15. Use of this impeller in the engine is expected to result in improvements in airflow, pressure ratio, and efficiency similar to those improvements demonstrated on the compressor rig.

Table IV.
Engine S/N D-1 compressor clearance measurements.

BU/TD	BU9 Cold wax goals—cm (in.) Min	Max	BU9 Cold wax measured—cm (in.) Min	Max	BU9 Rub pins measured—cm (in.) Min	Max	TD10 Cold wax measured—cm (in.) Min	Max	TD10 Rub pins measured—cm (in.) Min	Max	BU11 Cold wax goals—cm (in.) Min	Max
Inducer	0.013 (0.005)	0.024 (0.0095)	0.020 (0.008)	0.030 (0.012)	0.013 (0.0075)	0.020 (0.008)	0.010 (0.004)	0.028 (0.011)	0.010 (0.004)	0.013 (0.005)	0.013 (0.005)	0.024 (0.0095)
Knee	0.025 (0.010)	0.030 (0.012)	0.025 (0.010)	0.030 (0.012)	0.015 (0.006)	0.015 (0.006)	0.025 (0.010)	0.041 (0.016)	0.020 (0.008)*	0.027 (0.0105)*	0.025 (0.010)	0.030 (0.012)
Tip	0.020 (0.008)	0.028 (0.011)	0.013 (0.005)	0.025 (0.010)	0.010 (0.004)	0.010 (0.004)	0.023 (0.009)	0.025 (0.010)	0.018 (0.007)	0.027 (0.0105)*	0.020 (0.008)	0.028 (0.011)

*Rub pin not touched

Table V.
Engine S/N D-2 compressor clearance measurements.

BU/TD	BU1 Cold wax goals—cm (in.) Min	Max	BU1 Cold wax measured—cm (in.) Min	Max	BU1 Rub pins measured—cm (in.) Min	Max	TD2 Cold wax measured—cm (in.) Min	Max	TD2 Rub pins measured—cm (in.) Min	Max
Inducer	0.013 (0.005)	0.024 (0.0095)	0.006 (0.0025)	0.013 (0.005)	0.007 (0.003)	0.007 (0.003)	0.011 (0.0045)	0.015 (0.006)	0.001 (0.0005R)	0.007 (0.003)
Knee	0.025 (0.010)	0.030 (0.012)	0.025 (0.010)	0.033 (0.013)	0.023 (0.009)	0.024 (0.0095)	0.028 (0.011)	0.032 (0.0125)	0.025 (0.010)	0.030 (0.012)
Tip	0.020 (0.006)	0.028 (0.011)	0.023 (0.009)	0.030 (0.012)	0.020 (0.008)	0.022 (0.0085)	0.019 (0.0075)	0.025 (0.010)	0.017 (0.0065)	0.020 (0.008)

R = rub

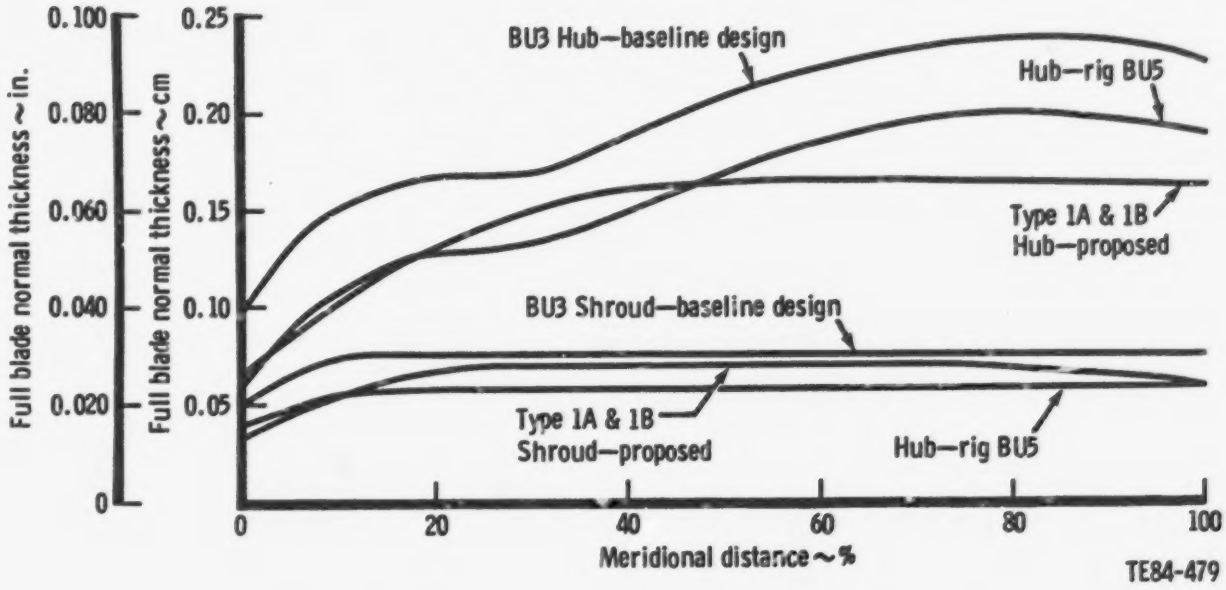

Figure 15. AGT 100 impeller hub and shroud blade thicknesses.

IV. GASIFIER TURBINE DEVELOPMENT

Gasifier turbine development for this reporting period is divided into the following three areas:

1. aerodynamic
2. mechanical
3. ceramic

Progress for the aerodynamic design consisted of definition of a new vane that will improve efficiency by as much as 1.5%.

In mechanical development cold and running clearances were obtained from engine assembly and testing, correction of gasifier-to-power-turbine-scroll misalignment, and initiation of design effort to incorporate the new vane.

Ceramic development continued during this reporting period on the gasifier scroll and rotor. A three-dimensional (3-D) finite element model defining scroll transient temperature gradients and corresponding stresses is presented in subsection 4.3 of this report. Probability of survival of 0.952 at the time of the highest thermal gradients approached the design goal of 0.9725. Probability of survival of the rotor for spin pit and operating conditions is also reported. Based on the latest material data, the reported probability of survival at maximum steady-state operating conditions exceeds the design goal value by 0.0189. Two rotor-to-shaft attachment schemes are reported, and a finite element model for the attachment is discussed.

4.1 GASIFIER TURBINE AERODYNAMIC DEVELOPMENT

Rig data analysis of the AGT 100 gasifier turbine indicated the vane loss to be larger than design. This has been attributed to the small vane width, trailing-edge blockage, and excessive turning downstream of the throat.

During this reporting period, aerodynamic definition of a new vane has been completed. This vane, shown in Figure 16, was originally designed and fabricated for a turbocompound turbine. This new design addresses all of the deficiencies identified in the AGT 100 gasifier rig data analysis and should provide an efficiency improvement of approximately 1.5%. A CAD/CAM layout drawing is being generated to establish the vane setting angle to achieve the desired throat dimension.

TE84-480A

Figure 16. New gasifier vane aerodynamic profile.

A comparison of the new and original vane design parameters are presented in Table VI. Significant advantages of the new vane are the following:

- 28% increase in vane width due to increased vane angle
- 8% increase in solidity due to longer chord
- 3.3% reduction in trailing-edge blockage due to reduced trailing-edge diameter
- 10 deg reduction in downstream turning
- 20% reduction in leakage through vane endwall slots (due to reduced number of vanes)
- 1.5% increase in static pressure reaction

During the next period, analytical effort will be directed toward identifying other areas for performance improvement of the gasifier turbine.

4.2 GASIFIER TURBINE MECHANICAL DEVELOPMENT

Gasifier turbine mechanical development during this reporting period included the following items:

- analysis of clearance measurements for engines S/N D-1 and S/N D-2
- analysis and correction of scroll-to-scroll fit problems
- initiation of gasifier turbine rematch modifications

A total of 13 platinum weld-wire rub pins are used to measure gasifier turbine running clearances with seven pins mounted on the rotor shroud and six mounted on the inner backplate as described in the previous semiannual report (EDR 11577). Cold wax clearance measurements are acquired at both buildup and teardown. The techniques used in obtaining these measurements are also described in the previous semiannual report.

Gasifier turbine clearances for engine S/N D-1, as shown in Table VII, indicate the cold wax clearance measurements at the tip for BU9 were open by approximately 0.04572 cm (0.018 in.) with respect to goal values. The coating on the gasifier turbine scroll was not restored between BU8 and

Table VI.
Comparison of vane design parameters.

	Original	New
Vane number	18	15
Vane throat—cm (in.)	0.5791 (0.2280)	0.5471 (0.2154)
Vane exit width—cm (in.)	0.6431 (0.2532)	0.8255 (0.3250)
Vane exit radius—cm (in.)	6.063 (2.387)	0.6063 (2.387)
True chord—cm (in.)	2.677 (1.054)	0.3472 (1.367)
Solidity	1.265	0.1367
Leading edge radius—cm (in.)	0.2540 (0.100)	0.2301 (0.0906)
Trailing edge radius—cm (in.)	0.0381 (0.015)	0.0254 (0.010)
Trailing edge blockage—%	10.7	7.4
Downstream turning—deg	10	0

BU9, resulting in the large difference. Loss of some of this coating during BU8 testing destroyed the rub pin height reference surface. For that reason, the rub pins on the scroll were not measured on BU9. Rub pin measurements taken at TD10 indicated a slight rub in the area of the exducer at the 12 o'clock position. An indication was present at this position at TD8; therefore, since the coating was not restored, the indicated rub may have been from either or all of BU8, BU9, or BU10 operation. The coating will be restored for BU11 and the cold wax measurement goals for BU11, as shown in Table VII, will be the same as for BU9 except closed down by about 0.00508 cm (0.002 in.) at the backplate.

Gasifier turbine cold wax measurements and goals and rub pin measurements for engine S/N D-2, BU1 through TD2 are shown in Table VIII. The cold wax measurement goals for engine S/N D-2, BU1 were the same as for engine S/N D-1, BU9. Rub pin locations for engine S/N D-2 were the same as for engine S/N D-1. No measurements were available for TD1 and BU2 since the scrolls were not removed. In general, the clearances were similar to those previously observed on engine S/N D-1, except no rub occurred at the exducer.

Two problems, related to the fit of the gasifier turbine scroll to the power turbine scroll, were encountered during the initial build of engine S/N D-2. The gasifier turbine scroll exit and the power turbine scroll inlet were misaligned so the interturbine coupling would not fit and the gap between the scrolls was decreased to approximately 0.6604 cm (0.26 in.), as compared with the design value of approximately 1.397 cm (0.55 in.). A search of previous build records on engine S/N D-1 revealed that although the coupling would fit, the gap between the scrolls, as shown in Figure 17, has always been about 0.6604 cm (0.26 in.). For this reason, engine S/N D-1 has been using an interturbine coupling whose overall length had been reduced 0.72136 cm (0.284 in.) by removing material from both ends of the coupling.

Inspection of both scrolls from both engines revealed minor deviations from print dimensions; the scrolls from engine S/N D-2 were out of print more than the scrolls from engine S/N D-1. The supplier who fabricates the scrolls was notified and inspections of his tooling also uncovered minor dimensional deviations. These deviations in tooling were corrected and both scrolls from both engines were returned to the vendor and reworked to the proper dimensions. The corrected scrolls were installed in BU1 of engine S/N D-2 and will be installed in BU11 of engine S/N D-1. In addition, a new interturbine coupling was designed to the same overall dimension as the original coupling but with a longer span between piston rings to permit more scroll misalignment. This new interturbine coupling was used on BU1 of engine S/N D-2 and will be used on BU11 of engine S/N D-1.

4.3 CERAMIC GASIFIER TURBINE DESIGN

This subsection presents a discussion of the finite element scroll analysis, an alternate scroll design, and probability of survival calculations and shaft attachment designs for the rotor.

4.3.1 Transient Three-Dimensional Finite Element Scroll Analysis

Allison's STRATA computer program was used to calculate scroll transient temperatures for turbine speed and inlet temperature versus time characteristics as shown in Figure 18. This calculation was done for the scroll body, backplate shroud, and exit elbow tube, all constrained together as an

Table VII.
Engine S/N D-1 gasifier turbine clearance measurements.

BU/TD	BU9 Cold wax goals—cm (in.) Min	BU9 Cold wax goals—cm (in.) Max	BU9 Cold wax measured—cm (in.) Min	BU9 Cold wax measured—cm (in.) Max	BU9 Rub pins measured—cm (in.) Min	BU9 Rub pins measured—cm (in.) Max	TD10 Cold wax measured—cm (in.) Min	TD10 Cold wax measured—cm (in.) Max	TD10 Rub pins measured—cm (in.) Min	TD10 Rub pins measured—cm (in.) Max	BU11 Cold wax goals—cm (in.) Min	BU11 Cold wax goals—cm (in.) Max
Tip	0.036 (0.014)	0.038 (0.015)	0.076 (0.030)	0.091 (0.036)	Not measured		0.076 (0.030)	0.094 (0.037)	0.023 (0.009)	0.030 (0.012)	0.036 (0.014)	0.038 (0.015)
Knee	0.028 (0.011)	0.033 (0.013)	0.043 (0.017)	0.053 (0.021)	Not measured		0.041 (0.016)	0.046 (0.018)	0.025 (0.010)	0.029 (0.0115)	0.028 (0.011)	0.033 (0.013)
Exducer	0.036 (0.014)	0.043 (0.017)	0.038 (0.015)	0.046 (0.018)	Not measured		0.028 (0.011)	0.038 (0.015)	0[R]	0.028 (0.011)	0.036 (0.014)	0.043 (0.017)
Backplate, o.d.	0.071 (0.028)	0.076 (0.030)	0.076 (0.030)	0.081 (0.032)	0.0445 (0.0175)	0.048 (0.019)	0.084 (0.033)	0.089 (0.035)	0.023 (0.009)	0.051 (0.020)	0.066 (0.026)	0.071 (0.028)
Backplate, i.d.	0.071 (0.028)	0.076 (0.030)	0.061 (0.024)	0.069 (0.027)	0.0495 (0.0195)	0.051 (0.020)	0.066 (0.026)	0.071 (0.028)	0.013 (0.005)	0.033 (0.013)	0.066 (0.026)	0.071 (0.028)

R = rub

Table VIII.
Engine S/N D-2 gasifier turbine clearance measurements.

BU/TD	BU9 Cold wax goals—cm (in.) Min	BU9 Cold wax goals—cm (in.) Max	BU9 Cold wax measured—cm (in.) Min	BU9 Cold wax measured—cm (in.) Max	BU9 Rub pins measured—cm (in.) Min	BU9 Rub pins measured—cm (in.) Max	TD10 Cold wax measured—cm (in.) Min	TD10 Cold wax measured—cm (in.) Max	TD10 Rub pins measured—cm (in.) Min	TD10 Rub pins measured—cm (in.) Max
Tip	0.036 (0.014)	0.038 (0.015)	0.041 (0.016)	0.053 (0.021)	0.033 (0.013)	0.0419 (0.0165)	0.051 (0.020)	0.076 (0.030)	0.030 (0.012)	0.038 (0.015)
Knee	0.028 (0.011)	0.033 (0.013)	0.042 (0.017)	0.056 (0.022)	0.030 (0.012)	0.033 (0.013)	0.038 (0.015)	0.069 (0.027)	0.028 (0.011)	0.0292 (0.0115)
Exducer	0.036 (0.014)	0.043 (0.017)	0.038 (0.015)	0.048 (0.019)	0.030 (0.012)	0.036 (0.014)	0.030 (0.012)	0.051 (0.020)	0.020 (0.008)	0.0241 (0.0095)
Backplate, o.d.	0.071 (0.028)	0.076 (0.030)	0.074 (0.029)	0.081 (0.032)	0.051 (0.020)	0.056 (0.022)	0.074 (0.029)	0.084 (0.033)	0.036 (0.014)	0.043 (0.017)
Backplate, i.d.	0.071 (0.028)	0.076 (0.030)	0.084 (0.033)	0.086 (0.034)	0.053 (0.021)	0.056 (0.022)	0.079 (0.031)	0.089 (0.035)	0.043 (0.017)	0.043 (0.017)

ORIGINAL PAGE IS
OF POOR QUALITY

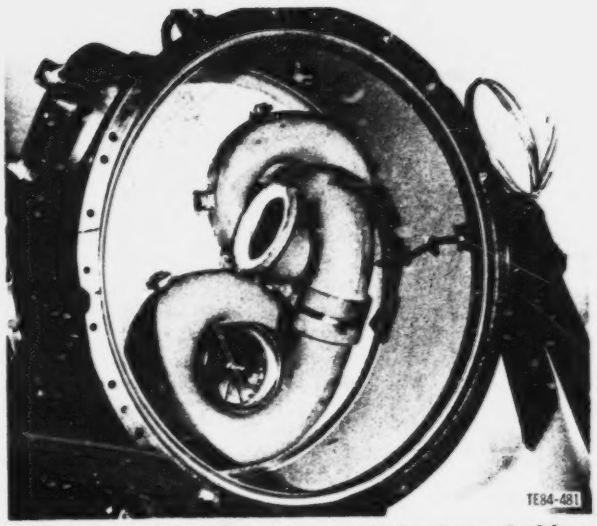

Figure 17. Gasifier turbine scroll to power turbine scroll gap.

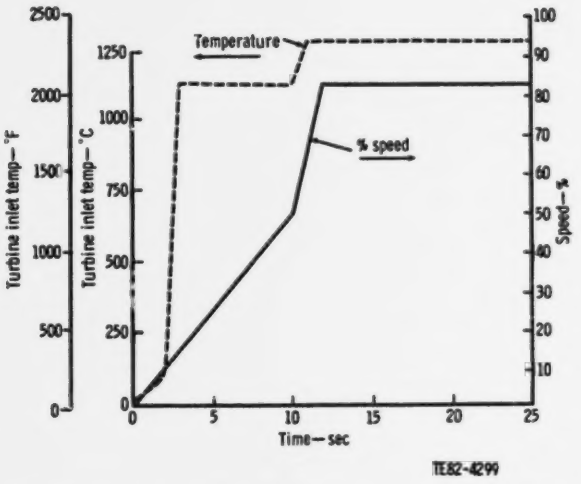

Figure 18. AGT 100 reference power-train design start transient.

Table IX.
Probability of survival summary (50 sec transient).

	Volume	Surface	Total
Scroll body	0.959166	0.992657	0.952123
Outer backplate	0.999872	0.999947	0.999819
Shroud	0.999999	1.000000	0.999999
Exit elbow tube	0.999939	0.999978	0.999917
Assembly total	0.958984	0.992583	0.951871

	Volume	Surface
Characteristic strengths	558 MPa (25,580 lb/in.^{2})	706 MPa (48,700 lb/in.^{2})
Weibull modulus	8.43	8.71

assembly. The time producing the highest thermal gradients—50 sec—was chosen as the point to be used for stress analysis. Those temperatures, proper mechanical constraints, and associated loads were imposed on each of the four components. Probability of survival (P_s) was calculated for each component and is summarized in Table IX. Material properties used for the Weibull analysis are also shown in the table. Laboratory evaluations currently underway are generating actual properties for alpha silicon carbide (SiC) from test bars. The Weibull analysis will be updated using actual material properties when sufficient statistical data are accumulated. These data should provide an improvement in the P_s values such that the total calculated P_s of 0.952 will approach the goal value of 0.972.

Figures 19, 20, 21, and 22 present temperature and maximum principal stress distribution plots for the scroll body, shroud, backplate, and exit elbow tube, respectively.

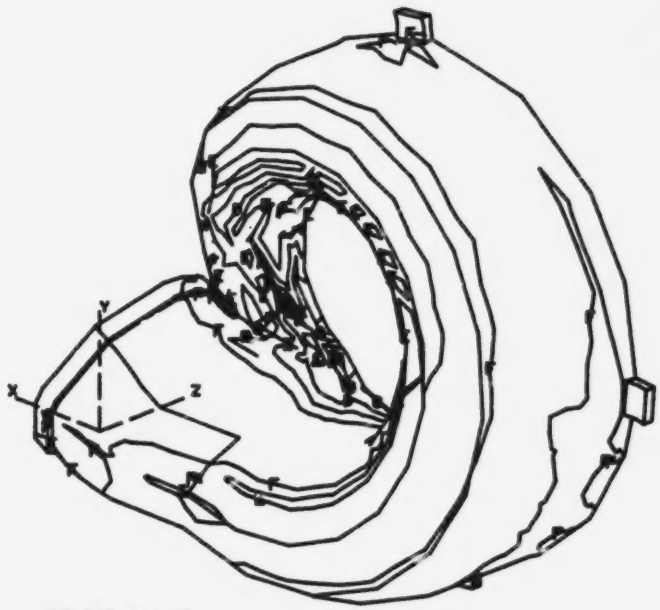

Legend--MPa (lb/in.^{2})

A	234.41	(34,000)
B	193.05	(28,000)
C	151.68	(22,000)
D	110.31	(16,000)
E	68.95	(10,000)
F	27.58	(4,000)
G	-13.79	(-2,000)
MAX	235.59	(34,170)
MIN	-30.34	(-4,400)

Denotes hidden

AGT 100 scroll
Contour plot of temperature maximum principal stress
Scale = 0.6400 Plot time and date = 18:13:00 83/318

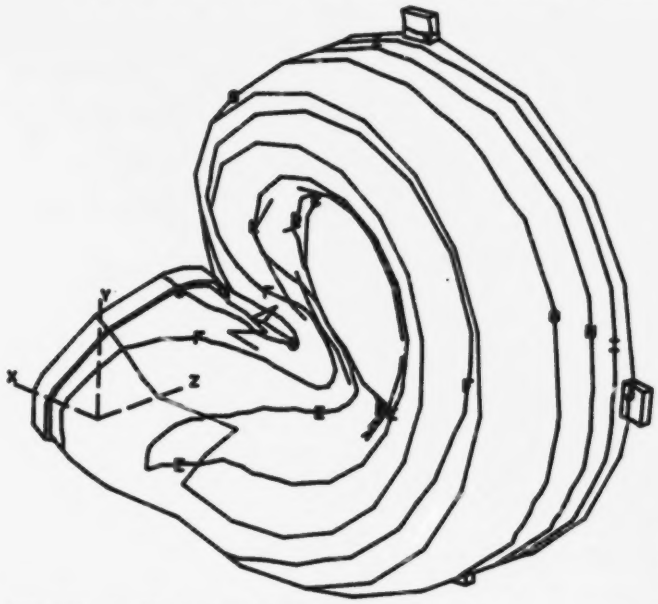

Legend--°C (°F)

A	926.67	(1700.00)
B	871.00	(1600.00)
C	815.56	(1500.00)
D	760.00	(1400.00)
E	704.44	(1300.00)
F	648.89	(1200.00)
G	593.33	(1100.00)
H	537.78	(1000.00)
I	482.22	(900.00)
J	426.67	(800.00)
MAX	940.42	(1724.76)
MIN	371.70	(700.52)

Denotes hidden

AGT 100 scroll temperatures at 50 sec
Contour plot of temperature
Scale = 0.6400 Plot time and date = 14:25:50 83/319

TE84-482

Figure 19. AGT 100 ceramic scroll body temperature and maximum principal stress distribution.

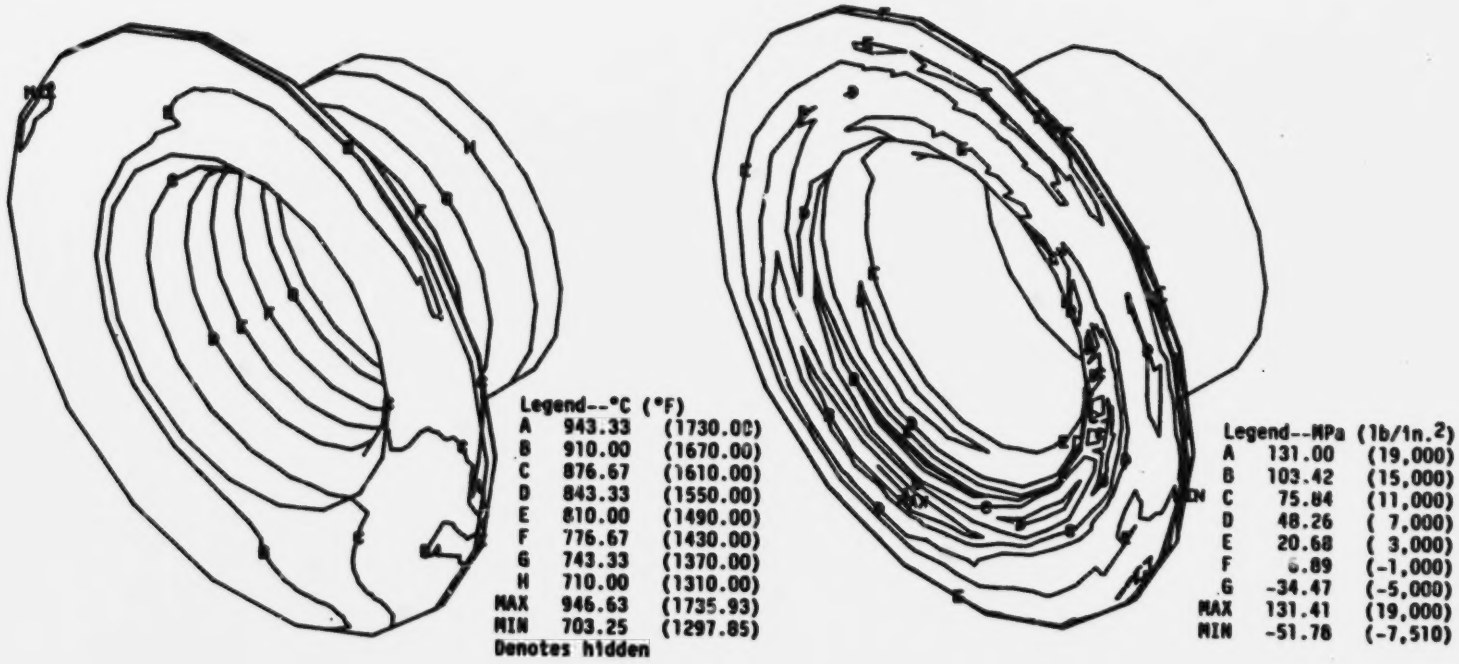

Figure 20. AGT 100 ceramic shroud temperature and maximum principal stress distribution.

ORIGINAL PAGE IS
OF POOR QUALITY

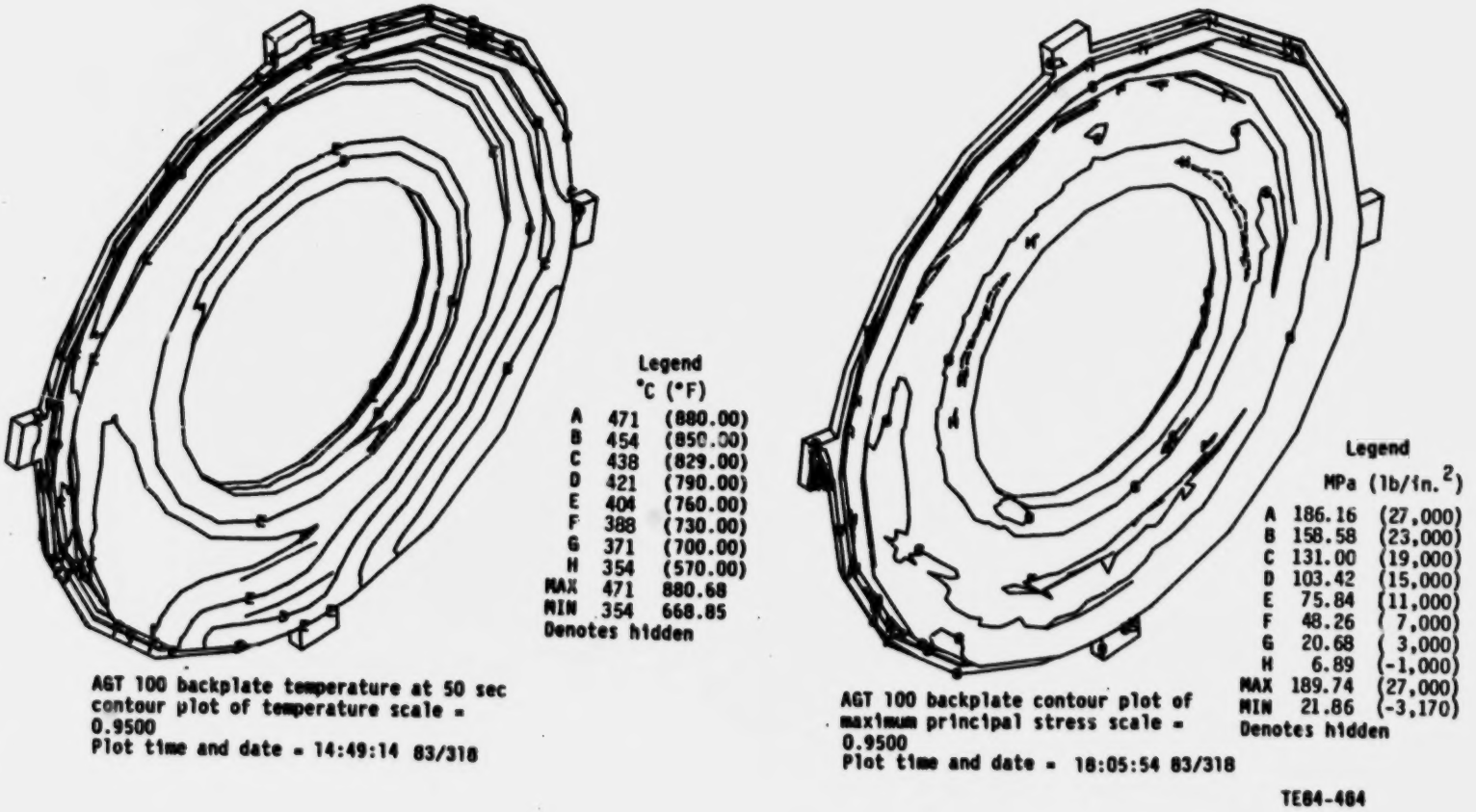

Figure 21. AGT 100 ceramic backplate temperature and maximum principal stress distribution.

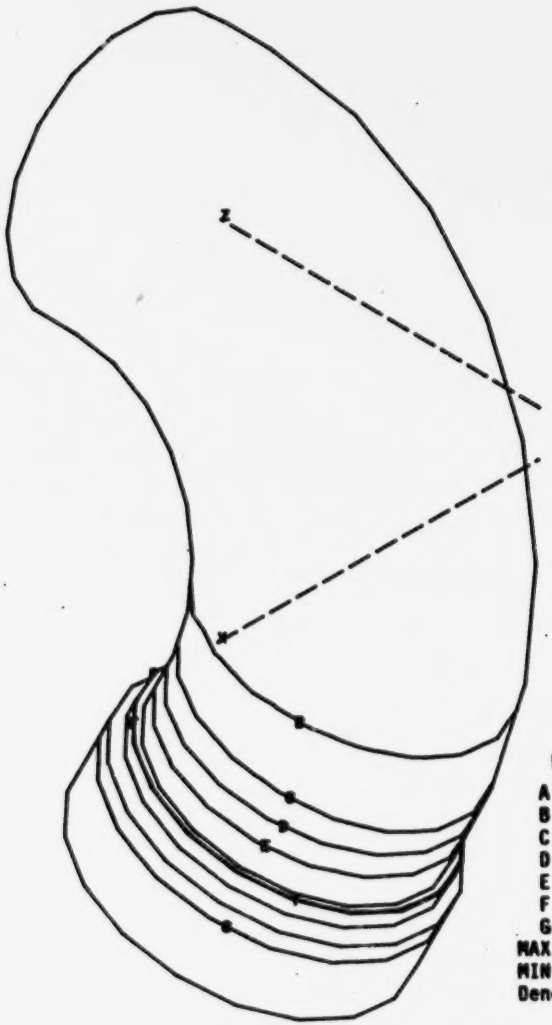

Legend--°C (°F)

A	721	(1330.00)
B	688	(1270.00)
C	654	(1210.00)
D	621	(1150.00)
E	588	(1000.00)
F	554	(1030.00)
G	521	(1337.71)
MAX	725	(1337.71)
MIN	496	(924.60)

Denotes hidden

AGT 100 tube temperature at 50 sec
contour plot of temperature scale = 1.3000
Plot time and date = 10:05:28 83/319

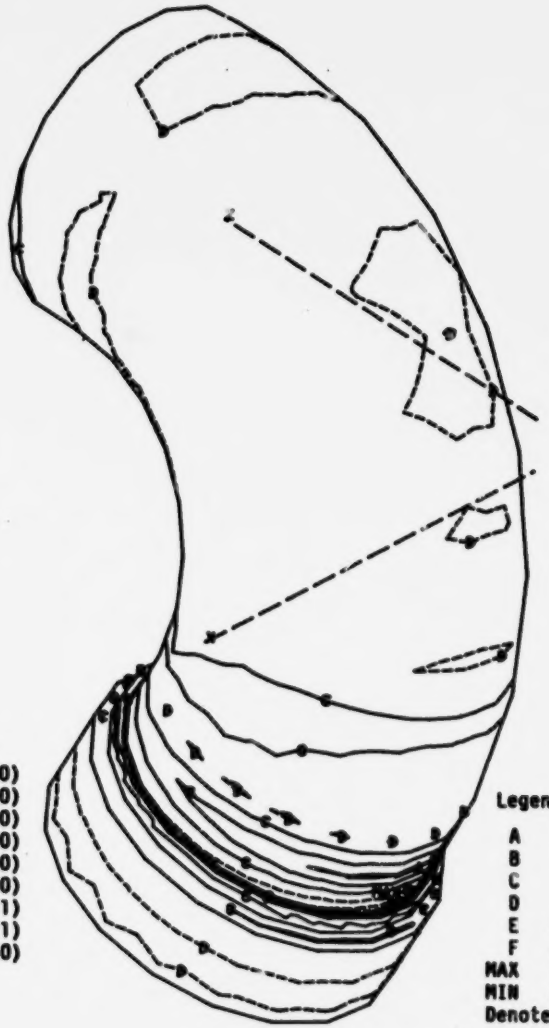

Legend--MPa (lb/in.^{2})

A	41.37	(6000)
B	27.58	(4000)
C	13.79	(2000)
D	0	0
E	-13.79	(-2000)
F	-27.58	(-4000)
MAX	36.20	(5250)
MIN	-38.75	(-5620)

Denotes hidden

AGT 100 tube contour plot of maximum principal stress scale = 1.3000
Plot time and date = 18:02:40 83/318

TE84-485

ORIGINAL PAGE IS
OF POOR QUALITY

Figure 22. AGT 100 ceramic exit elbow tube temperature and maximum principal stress distribution.

4.3.2 Alternate Design Scrolls

A scroll design study was initiated to create a design that is more compatible with the slip-casting method of manufacturing. The primary objective was to eliminate mold material at a smaller diameter than the casting. The difficulty with that type of configuration is that when the casting dries it shrinks onto the mold, which results in damage when the mold is removed. A much higher yield from the mold will be realized if this situation can be eliminated.

Figure 23 shows a cross section of a configuration that eliminates cast material at diameters longer than the mold. A layout will be made for this configuration in the near future. Also to be incorporated in the layout is a scheme for joining by brazing and/or sintering the separately cast inlet and scroll body parts.

4.3.3 Gasifier Turbine Rotor

Probability of survival analyses of the ceramic gasifier rotor has progressed. The analyses addressed spin and operating conditions. The spin condition included the as-molded rotor geometry (including airfoil machining stock) and the machined rotor geometry. The as-molded configuration simulates burst-test conditions for material characterization; the machined rotor simulates the engine configuration.

P_s was calculated in 1979 and 1982 for two sets of SiC material data generated during the

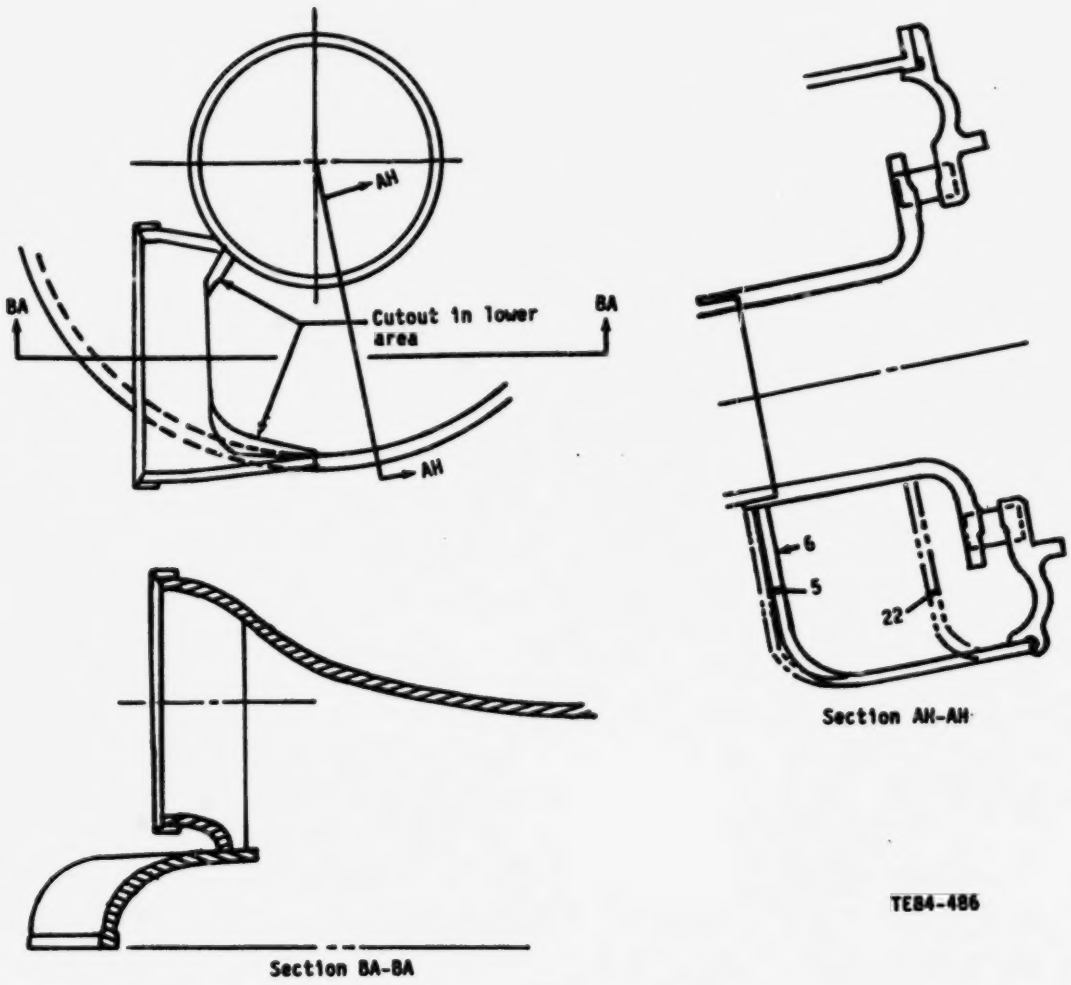

Figure 23. Alternate slip-cast scroll design configuration.

Ceramic Applications in Turbine Engines (CATE) project. The 1982 data are considered state-of-the-art alpha SiC properties. The property data are shown in Table X, and the corresponding P_s calculations illustrate the influence of the material strength. The P_s calculations are summarized in Table XI. Note that 3-D and two-dimensional (2-D) finite element models are being utilized at the spin and maximum power/steady-state conditions and that the models predict nearly identical probability of survival. Other comparisons are evident: the improved material (1982 data base) is significant, the additional airfoil mass of the as-molded rotor (versus machined) reduces the probability of survival, and the maximum power/steady-state P_s (0.9949) exceeds the design goal of 0.976. Calculations of P_s for the transient accelerations condition are active at the date of this report.

Detailed examination of the P_s calculations shows the volume flaw strength distribution is the dominant influence in rotor probability of survival. An estimate of the spin condition mean-failure speed can be made using this observation and the following relation:

$$\frac{\ln P_{s_1}}{\ln P_{s_2}} = \left(\frac{N_1}{N_2}\right)^{2\,M_v} \qquad (1)$$

Assumes P_s surface = 1

Consider mechanical spin and the as-cast configuration where:

P_{s_1} = 0.9935 (3-D prediction)
N_1 = 86,240 rpm (100% N_G)
M_v = 8.619 M_v — Weibull modulus, volume flaw strength distribution
N_2 = 0.5 (mean failure probability, mechanical spin)

Substituting values in Equation 1 gives the following:

N_2 = 113,050 rpm

This measure is useful in interpreting spin burst tests. For example, a group of burst test rotors demonstrating an average failure speed of 113,000 rpm would substantiate component performance similar to the average strength of material test bars. Also, the scatter in the burst speeds can be compared with the scatter in bar strength as another measure of the structural performance of the component. For comparison, the predicted mean failure speed of the machined rotor (less airfoil mass) is approximately 119,500 rpm.

A depiction of the required volume strength versus volume Weibull modulus for a given P_s can also be generated. Shown in Figure 24 are the required volume characteristic strength parameters to achieve P_s = 0.976 at room temperature and 100% shaft speed for the fully machined rotor. For comparison, the requirements at P_s = 0.990 are also shown. Identified in Figure 24 are demonstrated test bar strengths. The bar strengths exceed the requirements except for axial direction bars cut from rotors. However, the strength controlling feature of a rotor is the radial direction, not the axial.

Equation 1 can also be used to estimate the failure rate for overspeed proof qualification of machined rotors. Calculations predict a 2.5% failure rate for proof testing of rotors at 115% speed. This failure rate is judged to be economically acceptable.

Design and analysis of candidate rotor/shaft attachment schemes were active. Shown in Figures 25 and 26 are the most promising of the schemes. Both feature an insulator to reduce heat flux from

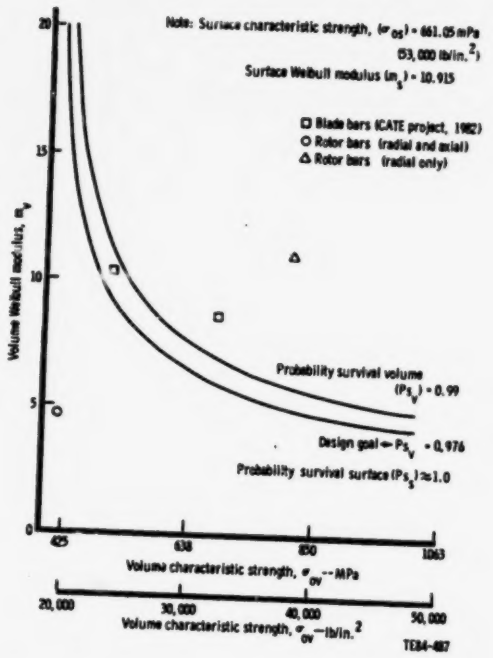

Figure 24. Required volume characteristic strength for the fully machined rotor.

Table X.
Alpha SiC strength properties (CATE project bar data).

Timeframe	MOR MPa (lb/in.²)	Surface strength σ_{os} MPa (lb/in.²)	M_s	Volume strength σ_{ov} MPa (lb/in.²)	M_v
1979	356.5 (51,700)	705.75 (48,700)	8.71	557.7 (25,580)	8.43
1982	384.0 (55,700)	661.05 (53,000)	10.915	686.5 (32,293)	8.619

Symbols:
MOR - modulus of rupture, bar specimen, 4 pt bend, 1/4 point loading, 1/8 × 1/4 × 1.5 in. span
σ_{os} - Weibull characteristic strength, surface flaw strength distribution
M_s - Weibull modulus, surface flaw strength distribution
σ_{ov} - Weibull characteristic strength, volume flaw strength distribution
M_v - Weibull modulus, volume flaw strength distribution

Table XI.
Gasifier rotor probability of survival at various conditions.[c]

(Alpha SiC material)

Maximum power steady-state conditions, goal: P_s = 0.976

Condition		Reliability, P_s 3-D FEM		2-D FEM	
	m_{os}/σ_{os} m_{ov}/σ_{ov}	8.71/48.7 8.43/25.58	10.915/53.0** 8.619/32.293**	8.71/48.7 8.43/25.58	10.915/53.0** 8.619/32.293**
Mechanical—spin at 100% N_G (maximum stress at root of blade, inducer)	(1) machined	0.9789	0.9975	0.9816	0.9978
	(2) as-cast	—	0.9935	0.9492	0.9938
Maximum power—steady state (maximum stress at stub shaft to backface)	(1) machined	0.9579	0.9949	0.9450	—
	(2) as-cast (for comparison)	—	—	0.8682	—

Transient acceleration to 83% N_G at 32 sec

FEM—finite element model
N_G—gasifier rotor speed, 100% = 86,240 rpm
*Calculations active at date of this report
**State-of-the-art material strength (1982 data base)

the rotor into the gasifier shaft. Figure 25 shows a thin layer between the shaft and insulator. Figure 26 shows a relatively thick layer between the shaft and insulator with an axial limit stop to facilitate assembly.

Finite element analysis is being used to calculate the temperature and stress distributions and the rotor/shaft joint probability of survival. Shown in Figure 27 is the finite element model for one of the candidate attachments (the other is similar).

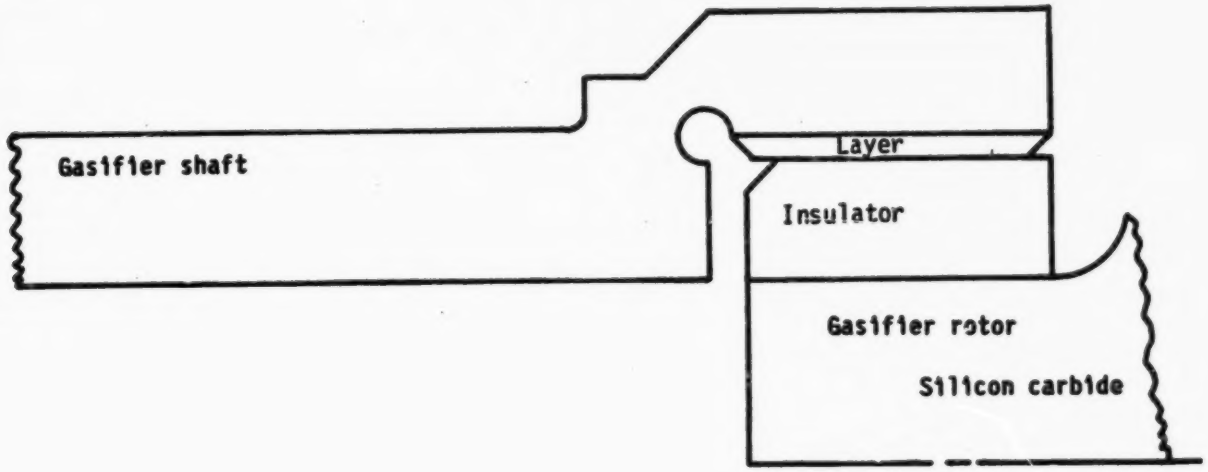

Ref: AA100932
AA100010

TE84-488

Figure 25. Candidate scheme for the ceramic rotor/metal shaft attachment.

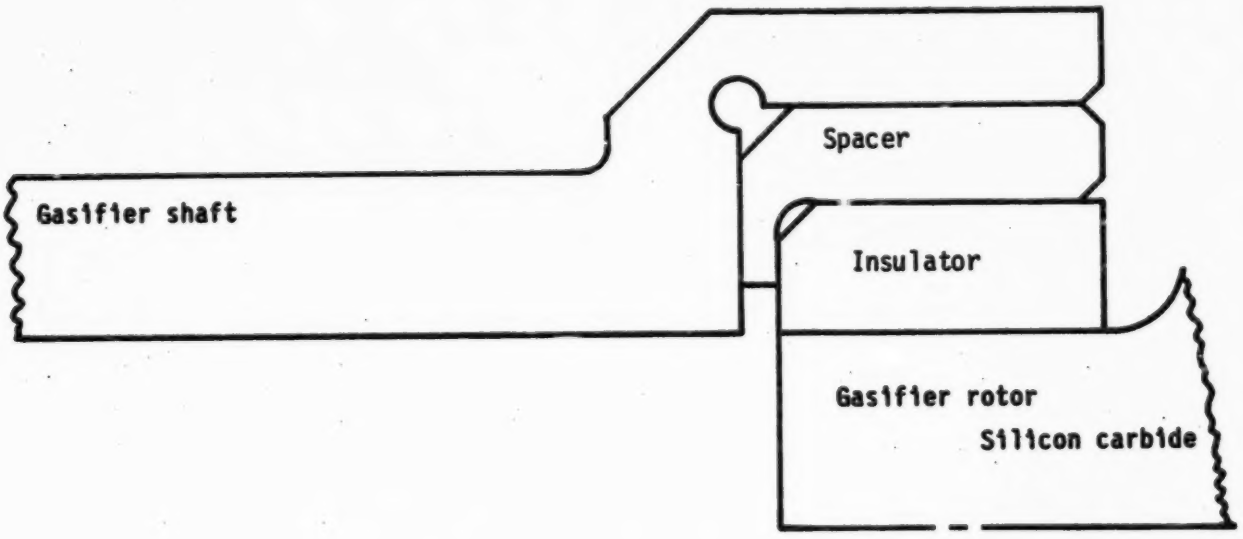

TE84-489

Ref: AA100932
AA100010

Figure 26. Candidate scheme for ceramic rotor/metal shaft attachment.

The goal of this study is to define an assembly interference fit that will maintain radial interference (contact) throughout the operating envelope of the engine.

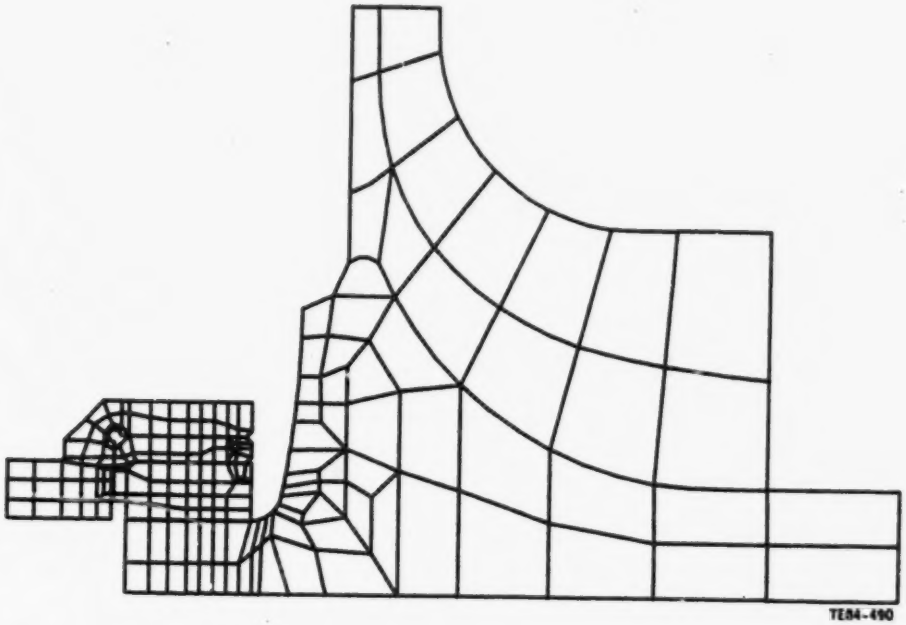

Figure 27. A finite element model for the ceramic rotor/metal shaft attachment study.

V. POWER TURBINE DEVELOPMENT

Power turbine development during this reporting period resulted in both aerodynamic and mechanical improvements. A significant improvement of 17% efficiency was defined for reduced temperature engine testing by reducing the capacity and matching at a lower speed. Mechanical improvements included reduction in clearances, a new power turbine exhaust coupling, and incorporation of reduced capacity and speed features for the improved efficiency rematching.

5.1 POWER TURBINE AERODYNAMIC DEVELOPMENT

The power turbine is not speed matched to the gasifier turbine at the reduced temperature—1080°C (1976°F)—testing of the AGT 100 engine. The turbine flow capacity at maximum power was originally selected for 68,000 rpm conditions, consistent with the reference power-train design (RPD) engine. This rpm level results in a ratio of turbine tip speed (U_T) to isentropic spouting velocity (C_T)* of 0.924 at maximum power. The RPD value is 0.72. This accounts for an efficiency reduction of approximately 15%. Although the power turbine speed can be reduced readily on the test stand through dynamometer adjustment, the mismatch continues to occur. The reduced speed operation results in higher flow capacity (typical of a radial turbine) and gives rise to reduced power turbine expansion ratio. Reduced expansion ratio results in reduced power turbine work and low engine shaft power.

A study was initiated to provide a rematch of the power turbine to achieve higher shaft power for reduced temperature engine testing. This rematch can be achieved by adjusting the turbine flow capacity to match the maximum power operating conditions at a power turbine speed of 53,395 rpm. This change will be made on the engine hardware by reducing the power turbine vane width to achieve the desired throat area. The analysis was conducted using engine test data from BU8 as the reference. The gas-generator cycle parameters for the rematched power turbine were selected to be the same for maximum power operation as interpreted from BU8 data. Results of this study are illustrated in Table XII. The 17% increase in power turbine efficiency as a result of the rematch is significant. A further gain in regenerator performance may be associated with the rematch due to reduced turbine exit swirl and Mach number.

*$C_T = \sqrt{2gJC_pT\left[1 - \left(\frac{1}{R_e}\right)^{\frac{\delta-1}{\delta}}\right]}$

where C_T = Isentropic spouting velocity
g = Acceleration due to gravity
J = Work equivalent of heat
C_p = Specific heat
T = Turbine inlet stagnation temperature
R_e = Turbine expansion ratio = inlet pressure/outlet pressure.

5.2 POWER TURBINE MECHANICAL DEVELOPMENT

Power turbine mechanical development during this reporting period included the following items:

- analysis of clearance measurements from engines S/N D-1 and S/N D-2
- design of a new power turbine exhaust coupling

A total of 13 platinum weld-wire rub pins are used to measure power turbine running clearances with seven pins mounted on the shroud and six mounted on the inner backplate as described in the previous semiannual report (EDR 11577). Cold wax measurements are acquired at both buildup and teardown. The techniques used in obtaining these measurements are also described in the previous semiannual report.

Power turbine clearances for engine S/N D-1, as shown in Table XIII for BU9 through BU11, indicate generally good agreement between cold wax goals and cold wax measured clearances. Rub pin measurements indicate clearances are still relatively open for the builds shown. Data were not available for TD9 and BU10 because the hot section was not disassembled. The cold wax clearance goals for engine S/N D-1, BU9 were reduced, with respect to the cold wax clearance goals for engine S/N D-1, BU8, by the values shown in the following:

- tip—0.0127 cm (0.005 in.)
- knee—0.00254 cm (0.001 in.)
- exducer—same
- backplate o.d. and i.d.—same

The cold wax clearance goals for engine S/N D-1, BU11 are the same as for engine S/N D-1, BU9, except the backplate goals have been reduced by 0.00508 cm (0.002 in.). These reductions in clearances are consistent with determining minimum safe engine running clearances.

Table XII.
Power turbine predicted maximum power operating parameters.

Parameter	BU8	Rematched turbine
Maximum speed—rpm	68,156	53,395
Vane width—mm (in.)	13.34 (0.5251)	10.80 (0.4250)
Actual flow—kg/s (lb/sec)	0.239 (0.526)	0.239 (0.526)
Equivalent flow—kg/s (lb/sec)	0.280 (0.616)	0.280 (0.616)
Expansion ratio (T-T)	1.6723	1.6723
Expansion ratio (T-S)	1.7325	1.7325
Efficiency (T-T)—%	69.8	87.0
Efficiency (T-S)—%	65.6	83.0
Equivalent work—kJ/kg (Btu/lb)	295 (12.7)	36.3 (15.6)
U_T/C_T	0.924	0.724
Exit swirl—deg	33.0	17.6
Exit Mach number	0.232	0.201
Static pressure reaction	0.744	0.493
Specific speed	95.4	73.8

Power turbine clearances for engine S/N D-2 are shown in Table XIV for BU1 through TD2. Rub pin locations for engine S/N D-2 were the same as for engine S/N D-1. The cold wax clearance goals for engine S/N D-2, BU1 were the same as for engine S/N D-1, BU9. No problems were indicated by the clearance measurements from engine S/N D-2.

In addition to the scroll alignment problems described in subsection 4.2, power turbine mechanical development effort during this reporting period included the redesign of the power turbine exhaust coupling to reduce the load transferred to the ceramic bulkhead. This redesign addressed the following:

- increase in overall coupling length to fit into the shortened bulkhead and increased span between piston rings to provide greater tolerance to power-turbine-scroll-to-bulkhead misalignment
- change in coupling material from Hastelloy X to 430 stainless steel to utilize the lower coefficient of thermal expansion of the new material to provide more tolerance for thermal growth and possible scroll-to-bulkhead misalignment
- reduction in the outside diameter of the end of the coupling that fits into the bulkhead to the minimum amount that provides piston ring engagement around the entire circumference of the coupling
- rounding of both ends of the coupling to reduce the possibility of binding in the power turbine scroll and the bulkhead
- relocation of the T_6 thermocouple mounting position from the bulkhead to the coupling

The new coupling, shown compared with the original coupling in Figure 28, was used in engine S/N D-2, BU1 and will be used in engine S/N D-1, BU11.

Table XIII.
Engine S/N D-1 power turbine clearance measurements.

BU/TD	BU9 Cold wax goals—cm (in.) Min	BU9 Cold wax goals—cm (in.) Max	BU9 Cold wax measured—cm (in.) Min	BU9 Cold wax measured—cm (in.) Max	BU9 Rub pins measured—cm (in.) Min	BU9 Rub pins measured—cm (in.) Max	TD10 Cold wax measured—cm (in.) Min	TD10 Cold wax measured—cm (in.) Max	TD10 Rub pins measured—cm (in.) Min	TD10 Rub pins measured—cm (in.) Max	BU11 Cold wax goals—cm (in.) Min	BU11 Cold wax goals—cm (in.) Max
Tip	0.048 (0.019)	0.058 (0.023)	0.048 (0.019)	0.058 (0.023)	0.050 (0.0195)	0.051 (0.020)	0.052 (0.0205)	0.074 (0.029)	0.052 (0.0205)	0.057 (0.0225)	0.048 (0.019)	0.058 (0.023)
Knee	0.038 (0.015)	0.064 (0.025)	0.042 (0.0165)	0.053 (0.021)	0.037 (0.0145)	0.038 (0.015)	0.043 (0.017)	0.056 (0.022)	0.038 (0.015)	0.043 (0.017)	0.038 (0.015)	0.064 (0.025)
Exducer	0.038 (0.015)	0.051 (0.020)	0.039 (0.0155)	0.043 (0.017)	0.038 (0.015)	0.038 (0.015)	0.041 (0.016)	0.046 (0.018)	LP	LP	0.038 (0.015)	0.051 (0.020)
Backplate, o.d.	0.046 (0.018)	0.053 (0.021)	0.051 (0.020)	0.069 (0.027)	0.037 (0.0145)	0.046 (0.018)	0.053 (0.021)	0.076 (0.030)	LP	0.0008 (0.0003)	0.041 (0.016)	0.048 (0.019)
Backplate, i.d.	0.046 (0.018)	0.053 (0.021)	0.043 (0.017)	0.056 (0.022)	0.030 (0.012)	0.041 (0.016)	0.028 (0.011)	0.048 (0.019)	LP	0.0005 (0.0002)	0.041 (0.016)	0.048 (0.019)

LP = lost pin

Table XIV.
Engine S/N D-2 power turbine clearance measurements.

BU/TD	BU1 Cold wax goals—cm (in.) Min	BU1 Cold wax goals—cm (in.) Max	BU1 Cold wax measured—cm (in.) Min	BU1 Cold wax measured—cm (in.) Max	BU1 Rub pins measured—cm (in.) Min	BU1 Rub pins measured—cm (in.) Max	TD2 Cold wax measured—cm (in.) Min	TD2 Cold wax measured—cm (in.) Max	TD2 Rub pins measured—cm (in.) Min	TD2 Rub pins measured—cm (in.) Max
Tip	0.048 (0.019)	0.058 (0.023)	0.056 (0.022)	0.076 (0.030)	0.048 (0.019)	0.048 (0.019)	0.046 (0.018)	0.058 (0.023)	0.043 (0.017)	0.055 (0.0215)
Knee	0.038 (0.015)	0.064 (0.025)	0.044 (0.0175)	0.055 (0.0215)	0.030 (0.012)	0.038 (0.015)	0.043 (0.017)	0.048 (0.019)	0.029 (0.0115)	0.038 (0.015)
Exducer	0.038 (0.015)	0.051 (0.020)	0.043 (0.017)	0.046 (0.018)	0.038 (0.015)	0.038 (0.015)	0.038 (0.015)	0.048 (0.019)	0.022 (0.0085)	0.036 (0.014)
Backplate, o.d.	0.046 (0.018)	0.053 (0.021)	0.043 (0.017)	0.048 (0.019)	0.030 (0.012)	0.038 (0.015)	0.038 (0.015)	0.043 (0.017)	0.020 (0.008)	0.028 (0.011)
Backplate, i.d.	0.046 (0.018)	0.053 (0.021)	0.041 (0.016)	0.048 (0.019)	0.033 (0.013)	0.038 (0.015)	0.038 (0.015)	0.046 (0.018)	0.018 (0.007)	0.030 (0.012)

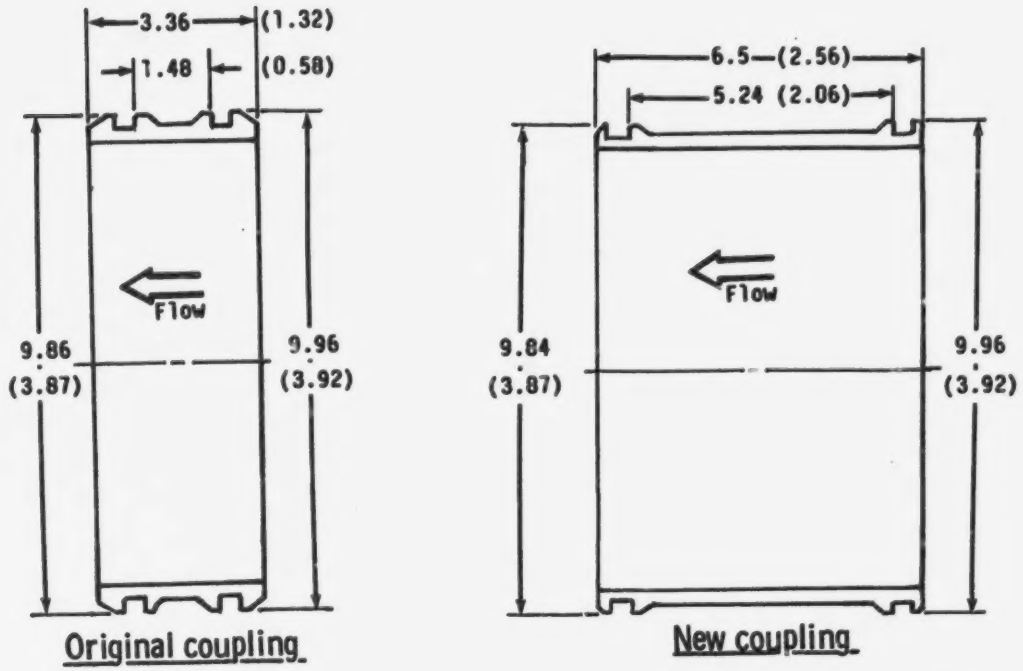

Note: All dimensions are in cm (in.).

TE84-491

Figure 28. A dimensional comparison of new and original power turbine exhaust couplings.

VI. COMBUSTOR DEVELOPMENT

During this reporting period, combustor development efforts were focused on test facility modifications, proof and nozzle tests, and transient heat transfer analysis. Significant improvement modifications were incorporated into the combustion rig during this period. These modifications included the addition of seven optical ports—one of which allows an infrared camera to view critical areas of the combustor. Additional modifications altered the airflow around the combustor so flow conditions in the engine were identically matched. Allison conducted 27 hr of rig testing in performing proof, cold start, pilot nozzle, and main nozzle evaluations. Main nozzle testing included lean blowout (LBO), rich flashback (RFB) mapping, and pilotless combustor testing. A transient heat transfer analysis also was conducted for rig start conditions. Results show only minor, 2-7°C, (3-12°F) inner-to-outer-wall temperature differences during the start cycle with the maximum thermally induced stress occurring at steady-state conditions or during extremely rapid cool-down cycles.

6.1 TEST FACILITY

As reported in the seventh AGT semiannual report, a combustor rig test section capable of handling the high temperature of the RPD cycle has been in use for some time. This facility, when built, duplicated the environment expected in the engine—such as the general flow path, insulating features, combustor orientation, variable geometry control, and fuel systems—as much as possible. A television camera, positioned to look through a periscope in the combustor exhaust, was connected to a color television monitor permitting visual observation of the combustion tests. This arrangement has proved extremely beneficial in analyzing the combustion phenomena during the continual development of the combustor. A preheater, capable of providing the combustion inlet air temperature at 1024°C (1875°F), was also successfully added to the combustor rig and has accumulated 80.5 hr of operation to date. This combustor test rig has been used extensively to evaluate problems with the current engine ceramic combustor that have occurred during pilot start and main nozzle operation.

Modifications adding seven optical ports to the rig (six for pyrometers and one for a camera) for viewing the combustor outer wall during hot firings have been completed. The large optical port allows an infrared camera to view the combustor body axially from planes just below that of the pilot to that of the combustor exit. Circumferentially, the view includes the two dilution holes across from the pilot. This method of observation removes the need for thermally painting the combustor to determine potential ceramic skin hot spots. The view is located in an area where hot spots have appeared in the past during cold-start nozzle operation and where hot spots have been traced to carbon deposition caused by liquid fuel puddling and subsequent expulsion from the pilot.

During this same period a preliminary heat transfer analysis of the cold-start transient to stabilized idle was initiated using typical combustor rig conditions. As analytical results of this study were to be compared with measured rig ceramic skin temperatures and ultimately used to develop a combined heat transfer/stress analysis of the engine combustor, a detailed comparison of the airflow around the combustors in the rig and engine was initiated. The airflow over the combustor in the engine is shown in Figure 29. Air exiting from the ceramic bulkhead flowed over the top 180 deg of the entire length of the combustor before entering the plenum between the back half of the combustor and the insulation. The airflow over the combustor in the rig, as depicted in Figure 30, also covered the front 180 deg of the combustor but only over a length extending to just above and below the dilution holes. Further, the mean air entry was centered over one of the dilution holes. This asymmetric rig airflow was not conducive to uniform dilution flow, and in the presence of skewed start nozzles, the airflow clearly aggravated nonuniform heating and created thermal stress gradients within the ceramic combustor body. By removal of insulation (the shaded area in Figure 30) and installation of a target centered over the dilution hole to deflect the incoming air both forward and sideways around the combustor, the flow path around the combustor closely simulated the engine flow path and provided for more uniform circumferential flow. The modified combustor rig has been reassembled on the test stand, and cold flow evaluation was conducted using a ceramic combustor body. The cold flow, close to the same Reynolds number as the hot flow, yielded tempera-

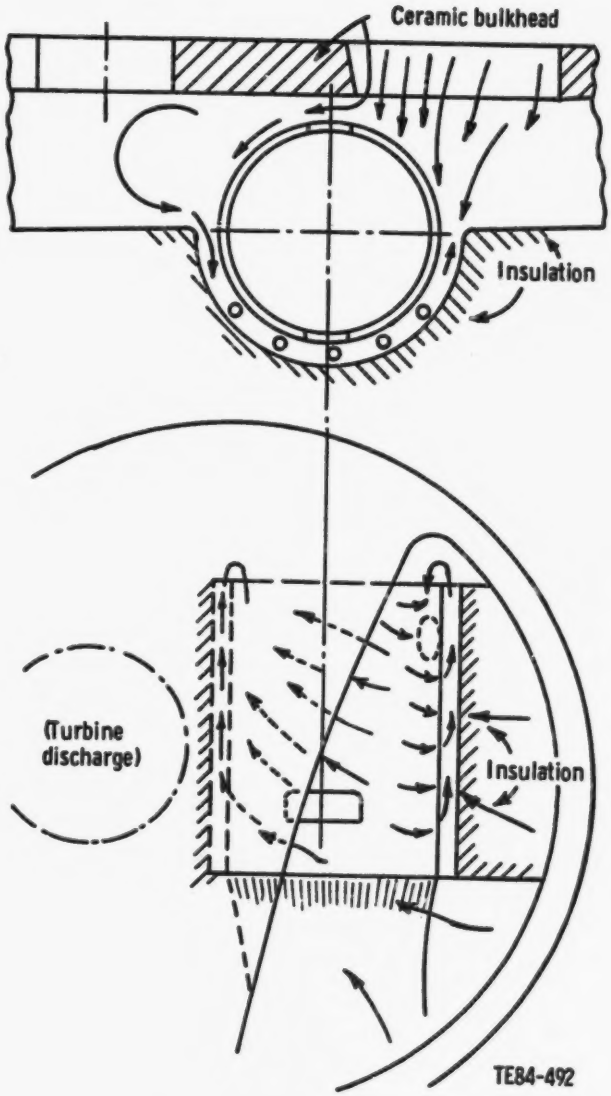

Figure 29. Airflow over AGT 100 combustor in engine.

ture, velocity, and pressure measurements that indicate that the modifications to the rig were successful in providing a nearly uniform flow around the combustor body. The magnitude of the measured air velocities—6.096–9.144 m/s (20-30 ft/sec)—indicates near plenum flow conditions.

6.2 TEST RESULTS

During this reporting period 27.6 hr of burning time were accumulated on the combustion rig. That time was devoted to proof testing present engine

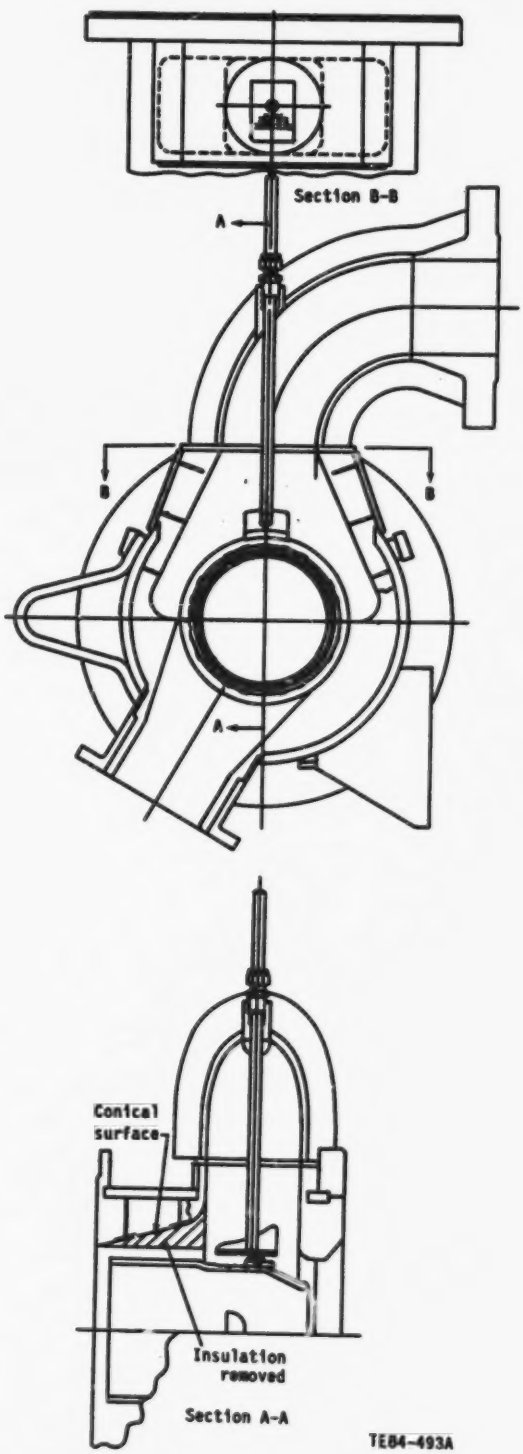

Figure 30. Airflow over the AGT 100 combustor as installed in the rig.

configuration assemblies, improving the cold start operation, and developing pilotless combustors incorporating new centerbody injection and ignition systems. Approximately 5 hr were devoted to start-nozzle-only operations; the remaining 22.6 hr involved main-nozzle-only operation.

6.2.1 Proof Testing

Combustor body assemblies 4 through 7 were proof tested. Assemblies 4 and 5 passed proof testing. Assembly 4 is still in the engine and now has accumulated over 60 hr of hot-fire operation. Assembly 5 was later rejected due to the presence of a flaw in the combustor body that was present but not detected prior to proof testing. Assembly 6 was used as a combustor development ceramic body, and results of this testing are reported in subsection 6.2.4. Assembly 7 experienced cracking of both dome and ceramic body. The ceramic body crack was later determined to be due to contact force (interference fit) between the pilot flame tube and the combustor body. As this was the first dome loss since its redesign during what appeared to be a normal rig qualification, emphasis was placed on determining the nature of the cracking. According to the investigation, the dome cracked due to a thermal gradient in the axial direction with the cooler temperature being on the reaction zone side of the combustor. A local hot spot was identified on the dome in line with a hot area upstream on the axial swirler. The crack initiation point was identified as being in the hot spot. The start-nozzle spray pattern was thought to have been distorted resulting in this local hot spot in the flame pattern. On shutdown or lean blowout the dome was cooled rapidly from the reaction zone side either by burner inlet air or unburned fuel resulting in excessive thermal stress on the dome. Initial tests on this combustor assembly were made to determine start-nozzle lean-blowout fuel flow rates at engine ignition condition. The start nozzle used was the last that had not been through the second and final rework of a newly developed Rochester Products Division process that smooths the fuel flow patternization profile. On recalibration of the start-nozzle spray pattern, the internal flow director was found to have been damaged (as a result of the main-nozzle rich-flashback tests described in subsection 6.2.4) and yielded random patternization flows between 35% and 60%.

6.2.2 Start-Nozzle Testing

Starting nozzles were reworked early in the program to provide higher idle fuel flow rates, and their flow patternization profiles were found to be skewed 35% to 50% (maximum deviation between any pair of six sectors on the flow patternization rig). The start nozzles were reworked initially to a 20% patternization profile, and subsequent combustor testing at cold start-up condition was successful. Two of the start nozzles have been reworked for the second time using a newly developed Rochester Products Division method that enhances and smooths the fuel flow patternization profile. Further, the technique is not sensitive to thermal distortion and has been found to enhance performance and durability on other Allison combustors. Flow patternization profiles from these nozzles have resulted in extremely uniform flow (skew of less than 15%), and all of the remaining start nozzles are being reworked now. Results from previous qualification tests indicate that desired operational characteristics improve as start-nozzle uniformity improves.

6.2.3 Pilot Testing

Recent operation on both the rig and engine indicates that the combustor pilot flame is extinguished early in the start-nozzle cycle due to pilot-nozzle flame blowout. As a result of the pilot loss, the combustor flames out (lean blowout) during main-nozzle operation when the burner inlet temperature (BIT) is below the self-ignition limit—760°C (1400°F) for the AGT combustor. Continued operation in this mode has resulted in pilot operational problems, particularly nozzle tip plugging (coking).

Because of the plugging, an investigation into the pilot fuel-nozzle flameout and subsequent coking was initiated. An initial change to a gaseous fuel (methane) proved to be very successful during atmospheric pressure testing. A specially constructed pilot test rig allowed a wide range of system pressure difference/inlet pressure ratios ($\Delta P/P_s$) to be simulated and overall methane injection pressure effects to be evaluated. Pilot flame was easily sustained at all $\Delta P/P_s$ simulating actual combustor condition. A wide tolerance of overall methane injection pressure allowed operation between rich and lean blowout limits at all combustor operating conditions.

Additional atmospheric pressure tests are in progress to determine optimal configuration changes to the pilot (primarily affecting its swirl air volume and flow pattern) using both methane and the desired pilot fuel—DF-2. Evaluation of fuel and configuration changes will be determined under hot fire conditions in the combustor rig. This is required particularly when DF-2 is used as the pilot

ORIGINAL PAGE IS
OF POOR QUALITY

fuel, since atmospheric testing of the present pilot did not duplicate engine or combustor rig coking problems.

6.2.4 Main-Nozzle Testing

Nearly all of the main-nozzle testing has involved the development of the pilotless centerbody and pilotless combustor operation. Previous results indicate that a pilot is not required at higher burner inlet temperatures to sustain the main-nozzle flame. The new design provides for start-nozzle ignition with the placement of the igniter within the present centerbody assembly. Extensive open air testing was conducted to optimize the placement of the ignition point. A design drawing of the new centerbody appears in Figure 31. The finished product is shown in Figures 32 and 33.

Besides incorporating igniters, the pilotless combustor centerbody includes a new water-cooled manifold surrounding the fuel tubes to suppress coking tendencies in the main fuel tubes at elevated BIT.

In the absence of a pilot, the combustor flames out [lean blowout (LBO)] during main-nozzle operation when the BIT is below the self-ignition limit of DF-2 [760°C (≈1400°F) for the AGT combustor]. To sustain combustion during this mode of main-nozzle operation, the burner variable geometry

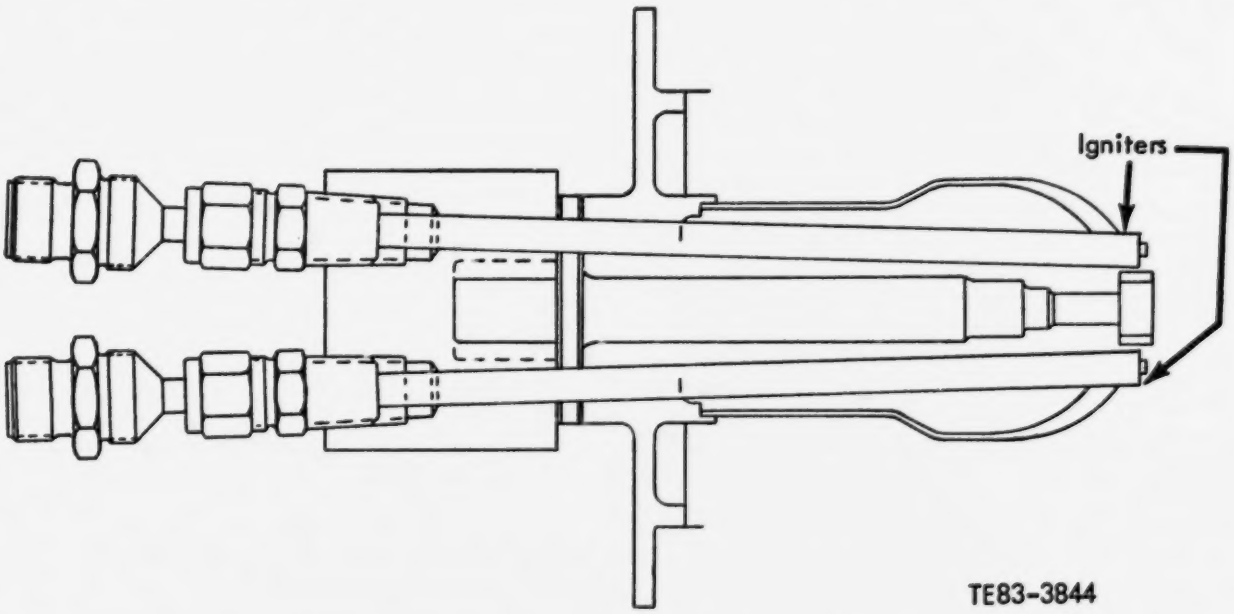

Figure 31. Schematic showing placement of igniters in centerbody.

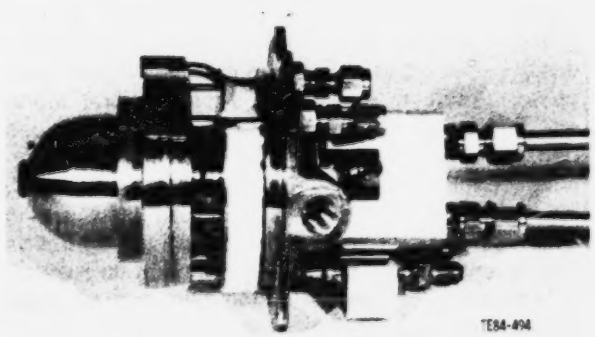

Figure 32. A side view of the pilotless combustor centerbody.

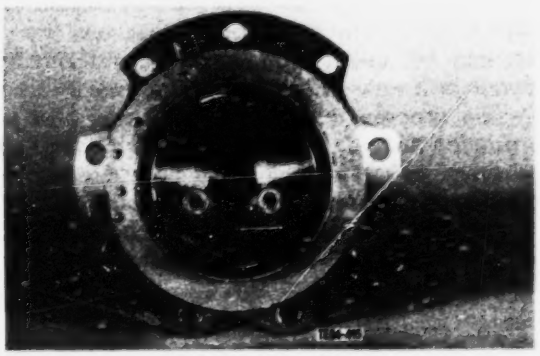

Figure 33. A front view of the pilotless combustor centerbody.

(BVG) settings must be changed to increase the primary zone fuel/air ratio. Present BVG settings were established in the presence of a pilot flame and result in a primary zone fuel/air ratio that is often slightly lower than the LBO limit in the absence of a pilot flame (Figure 34).

A decrease in the airflow in the primary zone (by decreasing the BVG setting) increased the primary zone fuel/air ratio above the LBO limit and permitted continuous operation but also increased the risk of rich flashback (RFB) into the premix chamber. This phenomenon occurs in a fuel/air premixed, prevaporized combustor when the velocity in the unreacting mixing and vaporizing portion of the combustor decreases below the flame speed and the primary zone flame flashes back into this region. This phenomenon has been experienced on the AGT engine combustor when the BVG settings were adjusted to permit continuous operation without a pilot.

As a result of the need to sustain the combustor flame at low BITs, an attempt was made to map the LBO and RFB operating conditions of the combustor, i.e., establish BVG settings that permitted safe engine combustion operation without a pilot and that would still be sufficiently close to the LBO limit so that NO_x is not appreciably increased. The limits, in terms of fuel/air ratios, were to be established at each BVG setting over a BIT range of 649°C (1200°F) to 982°C (1800°F).

Lean blowout limits were easy to obtain, and for the range checked to date—649°C (1200°F), 704°C (1300°F), and 760°C (1400°F) BITs—the limits verified past experimental information. In addition, the LBO limits were found to be unrelated to combustor loading. Rich-flashback limits were found at a given BVG setting to be a function of both the BIT and combustor loading. Increased combustor loading results in RFB occurring at lower primary zone fuel/air ratios. At increased combustor loadings the margin between the BVG settings resulting in LBO and RFB limits narrows somewhat, and tighter controls are required on the BVG settings at these conditions. Rich-flashback limits have been determined so far up to 760°C (1400°F). Both LBO and RFB limits for 100% speed (the highest loading) and present BVG limits as a function of fuel/air ratio and BIT are presented in Figure 34.

The LBO and RFB limits at high fuel/air ratios are widely separated for a given BVG setting. However, as fuel/air ratio and BIT decrease and require low BVG settings, the margin between LBO and RFB also narrows and concise operational control is necessary. As very little energy is required to sustain the flame at these conditions, the igniters in

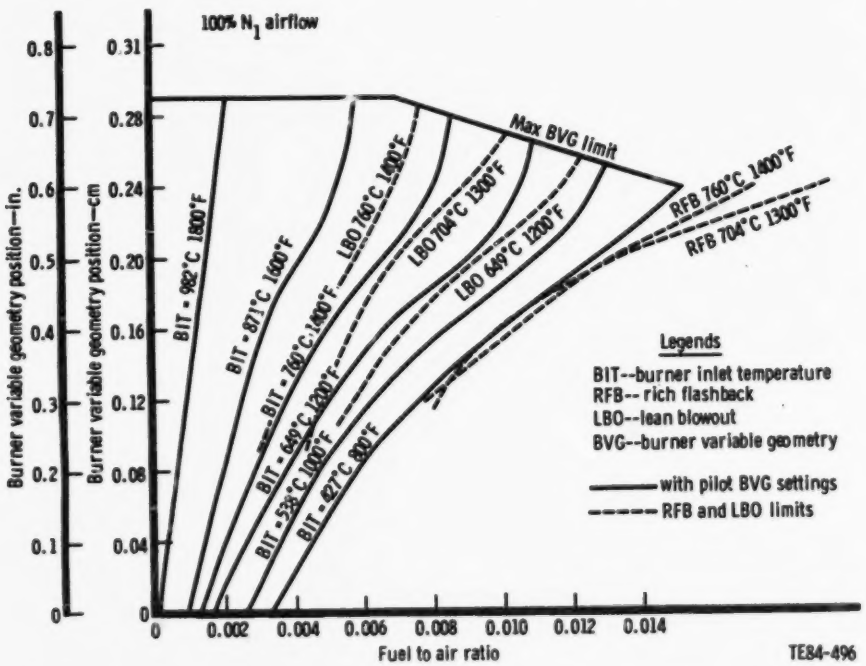

Figure 34. A plot of burner variable geometry position as a function of fuel/air ratio and burner inlet temperature.

the centerbody will be energized at BVG settings of 1 cm (0.4 in.) and below to determine if the LBO and RFB margins can be widened. Presently, the engine is operating successfully without a pilot on a revised BVG schedule, as shown in Figure 35.

During the combustor mapping, fuel flow exceeded 22.68 kgm/h (50 lbm/hr) with burner outlet temperatures exceeding 1427°C (2600°F) [over 1649°C (3000°F) in the primary zone]. This represents a significant increase in sustained fueling rate and burner outlet temperature (BOT) exceeding the requirements for one RPD cycle.

6.3 HEAT TRANSFER ANALYSIS

A preliminary heat transfer analysis of the cold-start transient to stabilized idle was done under typical combustor rig conditions. A 3-D finite element model (see Figure 36) was used to determine temperature during the transient and at steady-state idle conditions. Typical results from this analysis, which assumes an axisymmetric flow field inside the combustor, are shown in Figures 37 and 38.

While the predicted axial variation of surface temperature indicates an appreciable axial gradient near the dilution holes, the temperature difference between the inner and outer surfaces of the combustor was small. Variation was from 3.3-6.7°C (6-12°F) in the primary zone to about 1.7-2.2°C (3-4°F) in the cooler dilution region.

The low flow rates at idle and the high thermal conductivity of the silicon carbide combine to permit only a gradual buildup of combustor skin temperature. Thus, the maximum thermal and stress gradient in this analysis develops at steady-state conditions, and the combustor surface temperature at a given time in the transient is not very sensitive to the duration and peak temperatures characteristic of the start-nozzle transient. Table XV summarizes the conditions for two different start-nozzle transients typical of the combustor rig. Thus, through analysis, maximum stress gradients were found to occur at steady state and during extremely rapid cool-down.

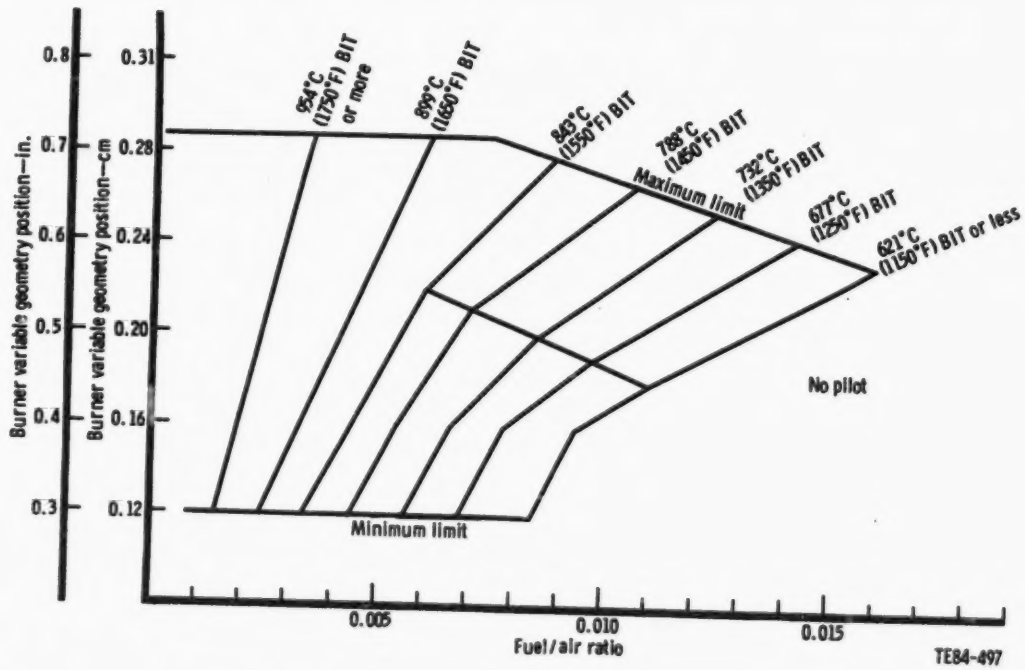

Figure 35. Burner variable geometry map for engine S/N D-2 BU3.

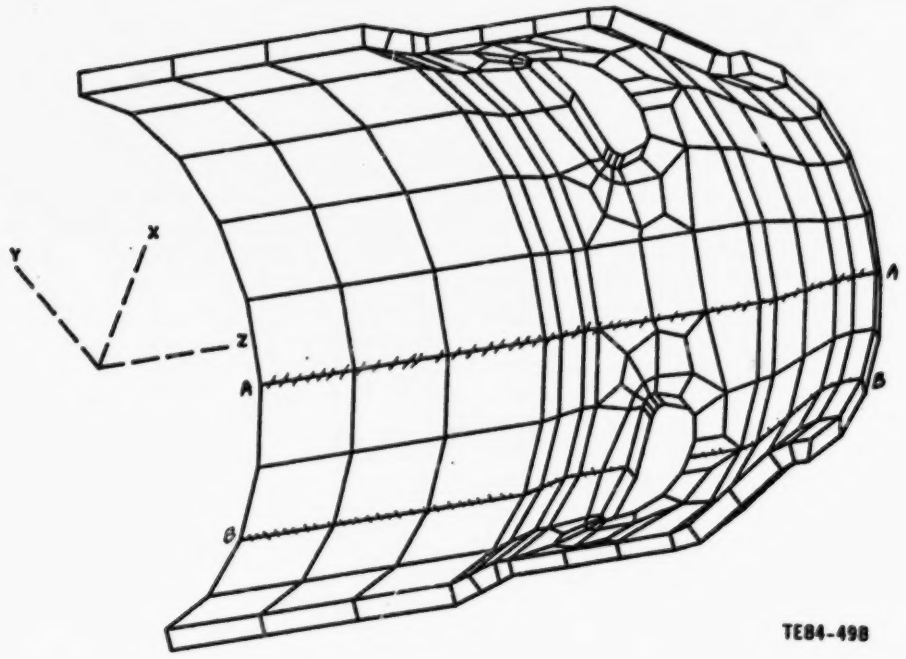

Figure 36. Finite element model of the AGT 100 combustor.

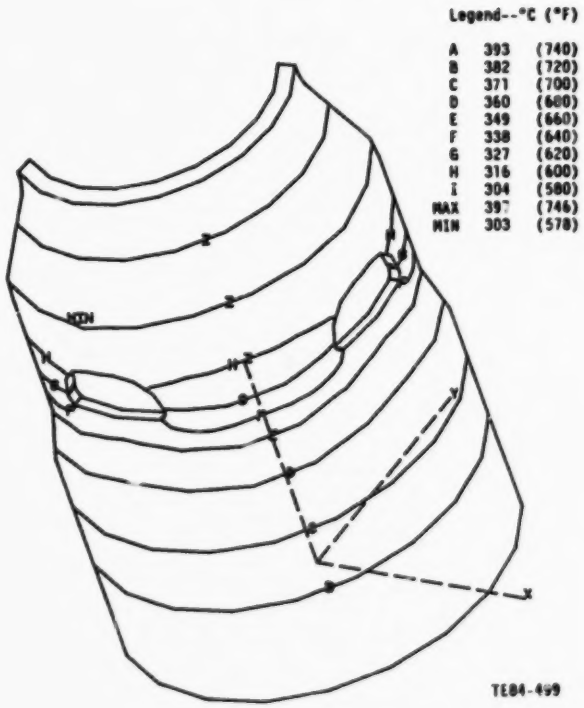

Figure 37. AGT 100 combustor body temperatures at 30 sec into the starting transient.

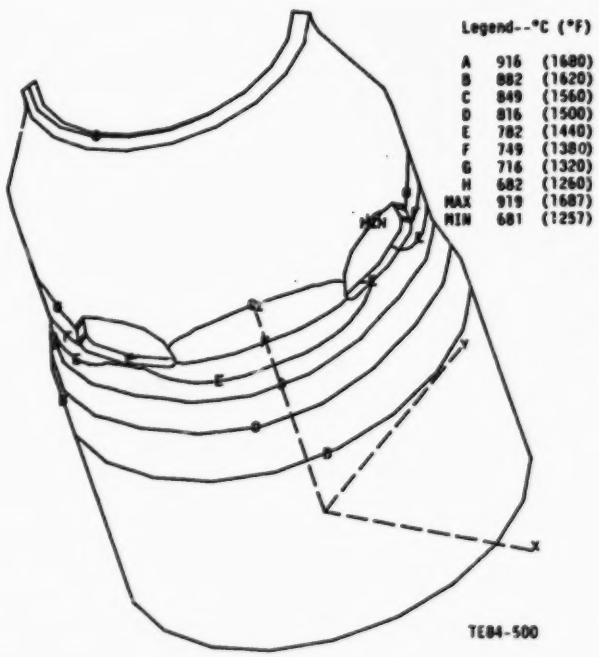

Figure 38. AGT 100 combustor body temperatures at steady-state conditions—1649°C (3000°F) primary and 954°C (1750°F) secondary (T_6).

Table XV.
Transient heat transfer analysis.

Time—sec	Transient 1 T_g—°C (°F) primary zone	T_g—°C (°F) dilution zone	BIT—°C (°F)
0	149 (300)	149 (300)	149 (300)
3	927 (1700)	593 (1100)	232 (450)
6	1649 (3000)	971 (1780)	316 (600)
15	1604 (2920)	1004 (1840)	404 (760)
30	1727 (3140)	1016 (1860)	443 (830)
45	1871 (3400)	1038 (1900)	482 (900)
SS	1871 (3400)	1038 (1900)	482 (900)

Time—sec	Transient 2 T_g—°C (°F) primary zone	T_g—°C (°F) dilution zone	BIT—°C (°F)
0	149 (300)	149 (300)	149 (300)
3	1871 (3400)	938 (1720)	232 (450)
6	1649 (3000)	971 (1780)	316 (600)
15	1677 (3050)	1004 (1840)	404 (760)
30	1788 (3250)	1016 (1860)	443 (830)
45	1871 (3400)	1038 (1900)	482 (900)
SS	1871 (3400)	1038 (1900)	482 (900)

SS = steady state

Conditions:

Mass flow rate:	0.109 km/s (0.24 lbm/sec)
Flow distribution:	60% dilution holes
	40% front end
Inlet pressure:	179.26 kPa (26 psia)
Wall emissivity:	0.80
Fuel/air primary zone:	0.04

VII. REGENERATOR DEVELOPMENT

The design goals for the AGT 100 regenerator system are to operate at 1065°C (1950°F) gas inlet temperatures with leakage levels of 5.0-5.5%. Current designs operating at 982°C (1800°F) have demonstrated 5.5-7.0% system leakage, and these designs also meet the operational requirements for initial engine testing. Laboratory and rig testing of regenerator matrix configurations to meet the higher temperatures as well as design/test efforts on advanced seals are described in this section. Rig testing continued to have primary importance in the development of regenerator hardware; engine testing led to design modifications to eliminate interference problems at the power turbine/regenerator ceramic bulkhead interface.

7.1 DESIGN AND MATERIAL DEVELOPMENT

Design and test effort during this period continued to emphasize reduction of regenerator system leakage, increased temperature capability, and the support of engine testing.

7.1.1 Outboard Seals

An alternate design of the outboard seal incorporates a one-piece silicone leaf to eliminate the seal leaf joints (current design has 9 joints) and minimize leaf leakage. Concepts utilizing the silicone leaf have been fabricated with both the present metal platform/graphite wearface and an integral polyimide platform/wearface, both shown in cross section in Figure 39 along with the current leaf design.

Rig testing of the silicone leaf/metal platform seal resulted in local separation of the silicone leaf attachment along the negative (low pressure carryover side) crossarm due to excessive temperatures. A modification using a thermal barrier of zirconia base cement and Zircar fabric, shown in Figure 40, was tested and significantly reduced the high temperature deterioration. A second change is being accomplished to modify both the thermal barrier configuration and incorporate a recently developed higher temperature silicone cement. This seal will be tested during the next quarter.

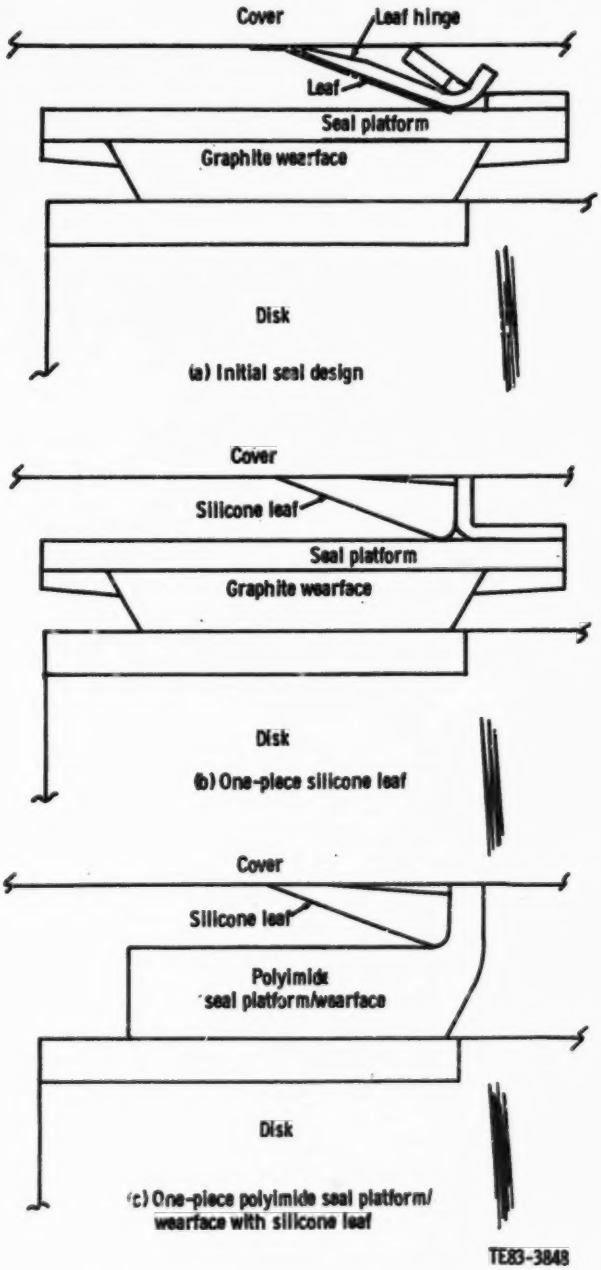

Figure 39. Outboard seal development sequence.

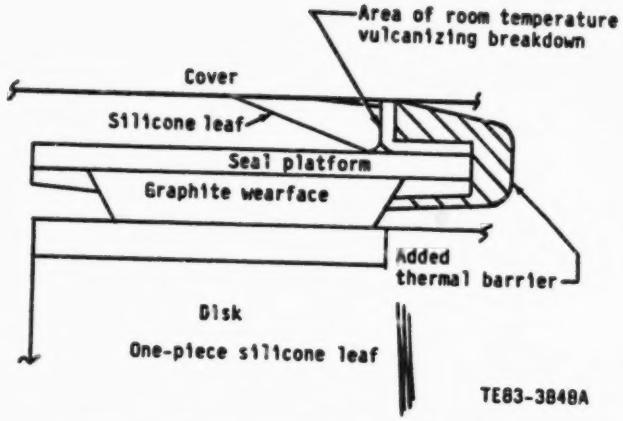

Figure 40. Cross section showing the thermal barrier addition to metal platform/silicone leaf seal.

Figure 41. Photograph of polyimide outboard seal wearface.

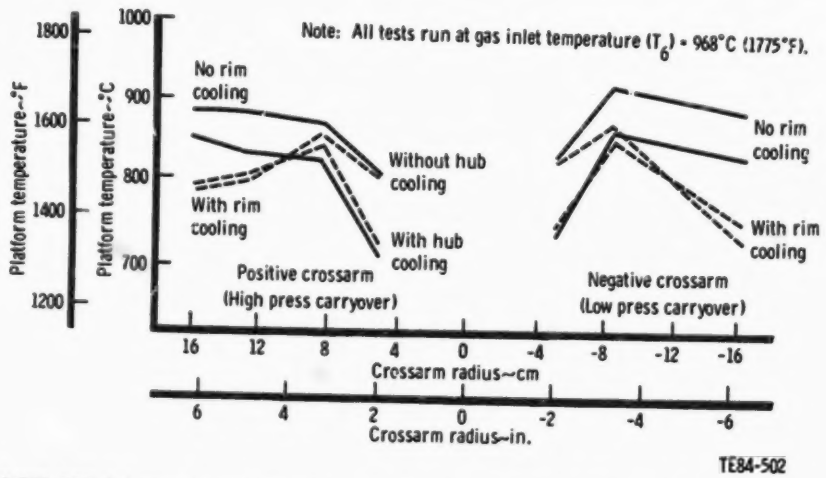

Figure 42. AGT 100 inboard seal platform temperature profile with and without cooling.

A polyimide platform/silicone leaf seal was rig tested for 35 hr at gas side (T_6) temperatures up to 982°C (1800°F). There were no adverse effects of temperature on either the silicone leaf or the room temperature vulcanizing (RTV) attachment and no signs of adverse wearface conditions after the test (see Figure 41). Testing of the seal terminated in a platform fracture due to the failure of an antirotation tab while operating at high torque conditions. Testing will continue with a design, incorporating reduced seal clamping and reduced torque levels, now being fabricated.

Characteristically, graphite wear rates are higher (2-3x) during the initial run-in period (10-15 hr) and then stabilize at a lower rate for the remaining life of the part. Two outboard seals have each accumulated 150 test hours and have a measured wear of 0.2 mm (0.008 in.). Based on related seal experience at Allison this projects to a wearface life of >1000 hr. These wear rates reflect the current use of high clamping forces on the seal wearface to reduce seal leakage. Planned seal designs with lower clamping forces will reduce graphite wear rates.

7.1.2 Inboard Seals

The current inboard seal crossarm relies on air cooling from both the hub and rim regions to permit operations to gas temperatures (T_6) of 982°C (1800°F). A series of hot rig tests were conducted to define the effectiveness of the cooling sources and evaluate several design modifications for possible use in extending the operating gas temperature to 1065°C (1950°F). Figure 42 summarizes the

ORIGINAL PAGE IS
OF POOR QUALITY

effectiveness of the currently employed rim and hub cooling techniques, which show 80–110°C (144–198°F) temperature reductions near the air entry point. Attempts to redistribute the flow along the crossarm had minimal [<15°C (27°F)] effects on reducing the maximum crossarm temperatures. Parametric testing of maximum platform temperature versus T_6 gas temperature resulted in the data shown in Figure 43. These data extrapolate to a platform temperature increase of 40°C (72°F) at the RPD design T_6 temperature of 1065°C (1950°F).

These results indicated that a different cooling approach was needed for more uniform crossarm temperature but that expected maximum temperatures at the 1065°C (1950°F) design point could possibly be met with a metal platform rather than a ceramic seal platform. Preliminary designs of several concepts are under way. One of the approaches employs a cooled interface between the plasma wearface and the metal platform. A cross section of this concept is illustrated in Figure 44 along with the current design. A key element in the design is the necessary leak-proof seal formed at the plasma spray/metal platform interface to prevent leakage of cooling air into the T_6 cavity of the engine. Test specimens of this and alternate concepts will be fabricated and lab tested before full-scale seals are built.

With the exception of the disk/seal interference problem noted in subsection 7.3, inboard seal wearfaces have proved satisfactory for engine/rig testing to date. For example, 150 hr of testing have been accumulated on one inboard seal assembly (35 hr engine/115 hr rig), the wear of the plasma-sprayed crossarm was 0.46 mm (0.018 in.), and the graphite rim wear was 0.08 mm (0.008 in.). The higher crossarm wear was the result of the increased crossarm clamping forces being utilized for reduced seal leakage. Alternate designs under study to permit reduction of clamping forces will reduce wear rates from this source.

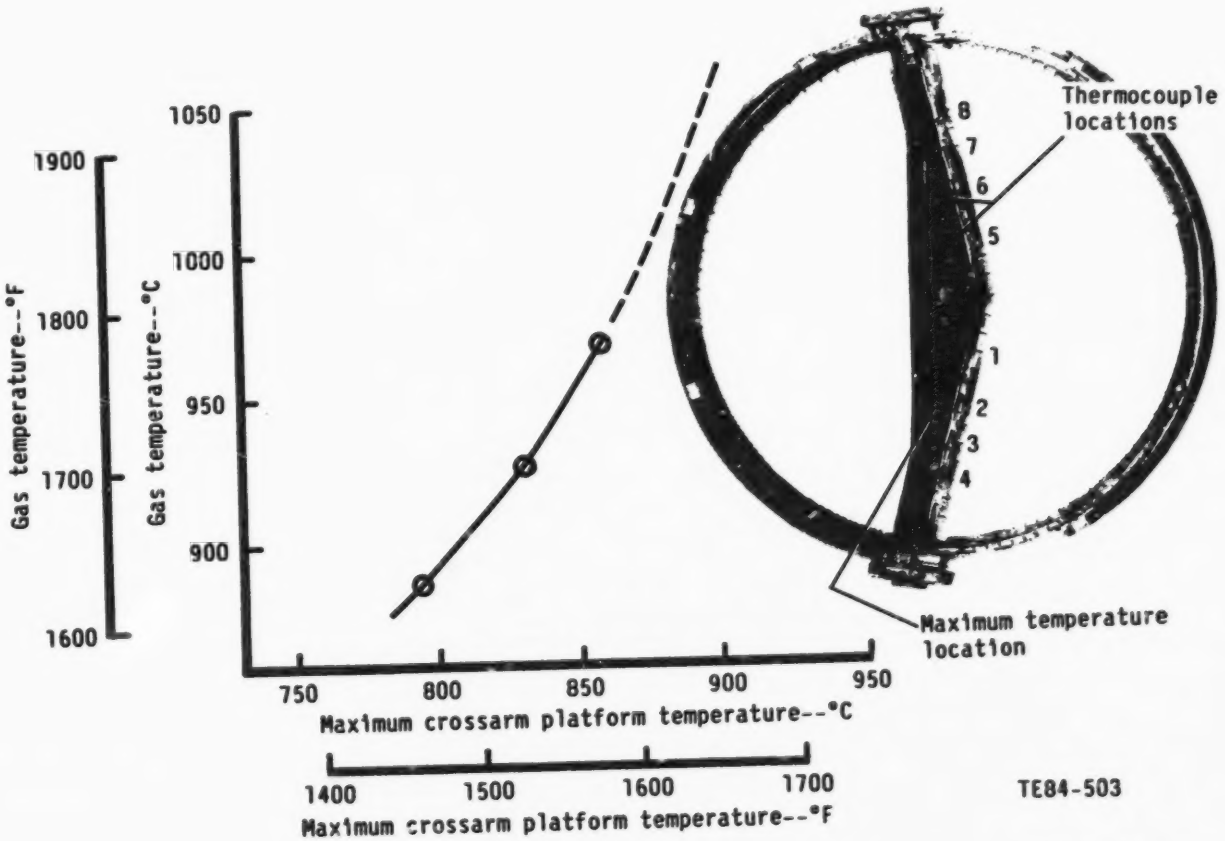

Figure 43. A graph of maximum platform temperature as a function of gas temperature including extrapolation to the RPD to design temperature.

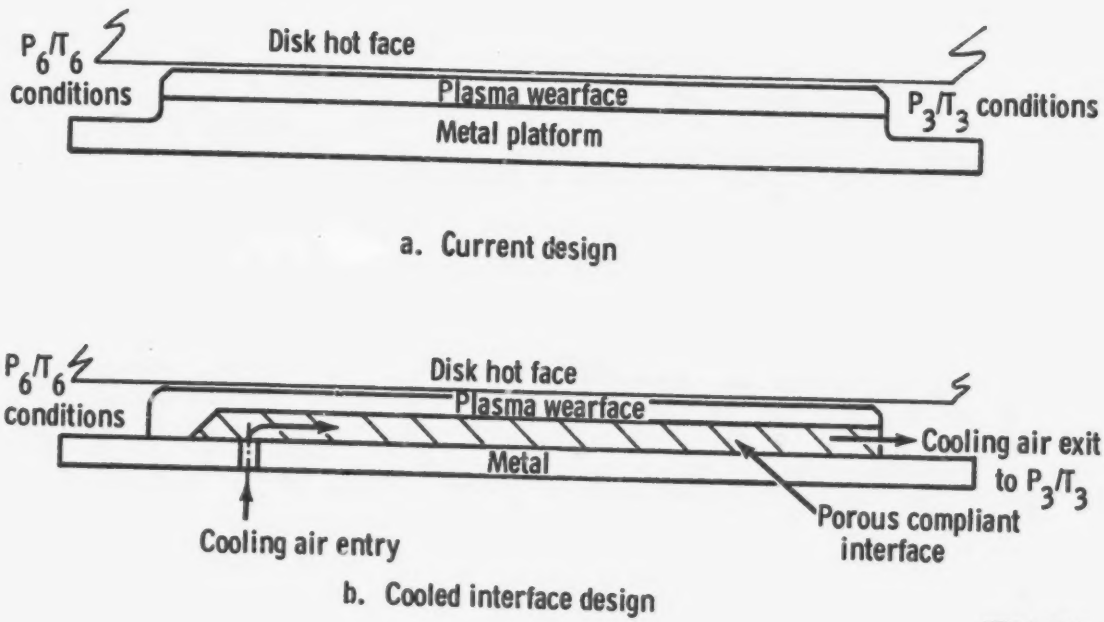

Figure 44. A comparison of the current inboard seal crossarm and a cooled interface concept.

7.1.3 Regenerator Disks

The primary disk design for the AGT 100 regenerator is the Corning Glass Works (CGW) code 9461 aluminum-silicate (AS) wrapped matrix rated at 1100°C (2012°F) and developed in the Ceramic Application in Turbine Engines (CATE) program. While meeting the current engine operating requirements, laboratory testing of this matrix design has uncovered variabilities in disk strength and through-wall leakage as well as the basic 1100°C temperature limit of the AS material. Consequently, two alternate materials, extruded magnesium-aluminum-silicate (MAS) matrices by NGK-Locke (NGK) and an advanced MAT (Corning trade name) material by CGW are being evaluated in the AGT 100 program. Figure 45 illustrates sections of the CGW/AS and NGK/MAS matrices. Table XVI summarizes the basic as-received characteristics of the materials under study with the highlights noted in the following:

- The current CGW 9461 exhibits excellent tangential strength, good through-wall leakage, but reduced radial strength due to the random lay-up of the wrap process. Due to process variabilities, some disks (line 2 of Table XVI) show reduced wall thickness resulting in a significant increase in leakage and reduced strength.
- The higher temperature MAS has lower tangential strength but the extruded matrix produces a much improved radial strength characteristic. Initial MAS (CO_3) samples had unacceptable leakage rates as well as low tangential strength.
- Impregnation of the MAS with a ceramic coating reduces leakage levels to those approaching AS with significant modulus of rupture (MOR) improvements; these materials were selected for the full-size disks being evaluated.
- The CGW MAT material is in the early development phase and only limited testing has been completed; it has strength characteristics similar to the impregnated MAS but with superior temperature capabilities.

Earlier work at Allison on the CATE program established that the critical operational mode for a ceramic regenerator disk is the combination of an engine maximum acceleration transient followed by a maximum braking effort. As a result, a laboratory cyclic thermal exposure (CTE) test procedure has been developed for use in evaluating each matrix candidate.

CTE testing of the CGW AS matrix has included samples tested to 1232°C (2250°F) peak temperature as well as other samples cycled 20,000 times [to 1176°C (2150°F)]. Typical results for AS are shown in Figure 46, illustrating a characteristic reduction in disk hot face strength that diminishes to a minor effect at the disk cold face. During this reporting period, tests of AS included evaluation of

ORIGINAL PAGE IS
OF POOR QUALITY

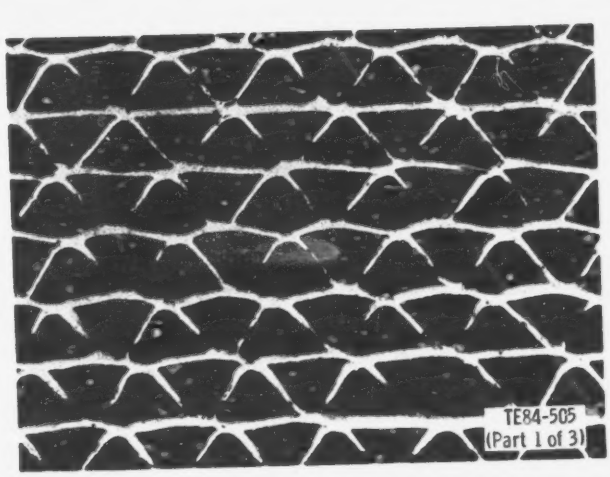

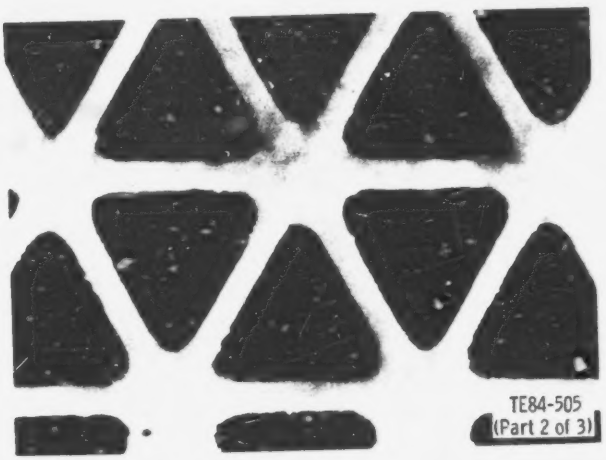

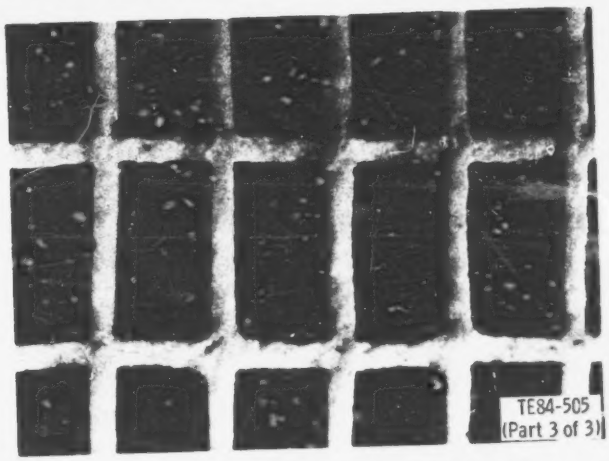

Figure 45. AGT 100 regenerator matrix configurations.

Table XVI.
Summary of as-received disk properties.

Material	Temp limit— °C (°F)	Cells/m²— (cells/in.²)	Relative leakage	Wall thickness— m (in.)	Tangential MOR kPa (lb/in.²)	Radial compressive strength— kPa (lb/in.²)
CGW-AS						
9461	1100 (2012)	2.17×10^{6} (1400)	1.0	0.64×10^{-4} (0.0025)	3121 (452)	587 (85)
9461	1100 (2012)	2.17×10^{6} (1400)	1.5	0.48×10^{-4} (0.0019)	2417 (350)	407 (59)
NGK-MAS						
C03*	1200 (2192)	1.395×10^{6} (900)	18.0	1.17×10^{-4} (0.0046)	1360 (197)	1595 (231)
CO3P**	1200 (2192)	1.395×10^{6} (900)	1.5	1.37×10^{-4} (0.0054)	2488 (360)	— —
CO9P***	1200 (2192)	1.705×10^{6} (1100)	1.5	1.22×10^{-4} (0.0048)	1982 (287)	— —
CGW-MAT	1500 (2732)	—	—	1.78×10^{-4} (0.007)	1844 (267)	— —
	1500 (2732)	—	—	2.54×10^{-4} (0.010)	1885 (273)	— —

*Triangular flow path
**Triangular flow path with impregnated walls
***Rectangular flow path with impregnated walls

ORIGINAL PAGE IS
OF POOR QUALITY

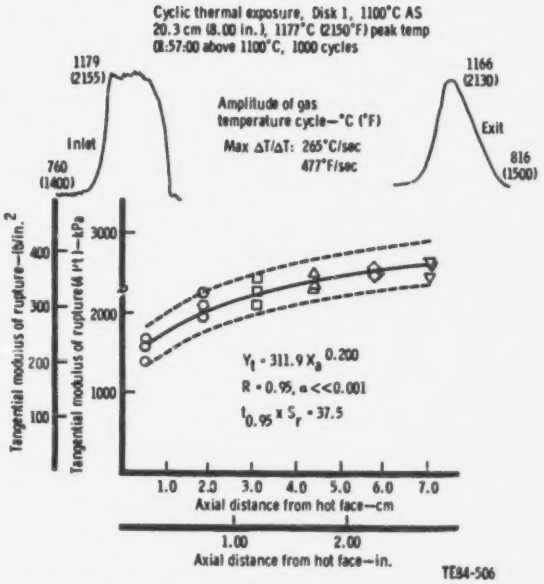

Figure 46. Strength of Corning Glass Works AS matrix at reduced temperature gradients showing negligible changes.

the effect of rate of temperature increase/decrease during the CTE test. Changing the rate from 1167°C (2100°F) per sec to 361°C (650°F) per sec resulted in negligible changes in matrix strength.

The first fracture of an 1100°C AS matrix occurred during hot rig testing on a disk that had accumulated approximately 80 hr of test time. The disk, S/N 17-01, developed a radial fracture starting from a 38 mm (1.5 in.) long circumferential crack at the inner edge of the filled area at the disk periphery, as shown in Figure 47. Close examination of the disk, after removal of the ring gear, showed that the radial fracture extended from the outer diameter (o.d.) to a circumferential crack at 77 mm (3.0 in.) radius and then extended through a 150 deg arc at that radius. Radial saw cuts at the ends of this crack revealed that the crack extended through the disk.

Three samples were cut from the disk at radii of 184 mm (7.25 in.), 124 mm (4.88 in.), and 63.5 mm (2.50 in.) away from the radial fracture. Two more samples were cut at 184 and 124 mm (7.25 and 4.88 in.)—immediately adjacent to the fracture—for comparison. Separator wall fracture plane thicknesses (X_W) and channel skew angle (X_S) were measured and the tangential MOR determined. The data were then reduced using single and multiple regression analyses to separate and identify the importance of the variables.

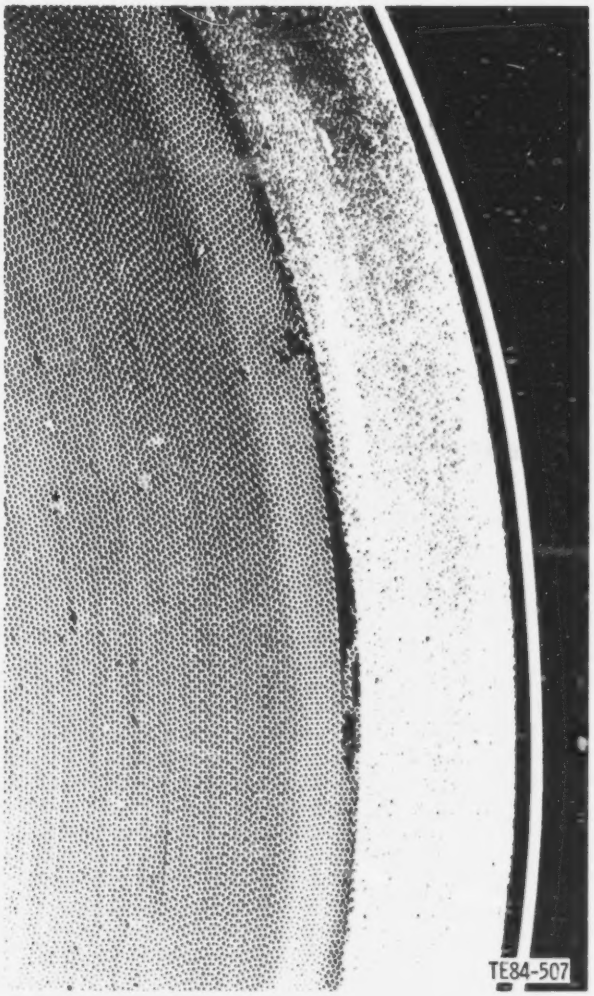

Figure 47. A photograph showing radial and circumferential cracks in AGT 100 disk 17-01 after 80 hr of testing.

The disk proved to be by far the weakest 1100°C AS disk tested to date, with mean sample MOR values ranging from 1083 to 1372 kPa (157 to 199 lb/in.²). The sample separator wall fracture plane thickness averaged 0.04 mm (0.0015 in.) with individual test bars averaging as low as 0.03 mm (0.0011 in.). No significant differences are shown in wall thickness with radial position or between samples taken close to the fracture or away from it. The test results showed clearly that the disk was uniformly low in strength due largely to thin separator walls. However, comparison of Disk 6 (S/N 17-01) with the four 1100°C AS disks tested under the CATE program shows a high probability that a second variable accounted for some of the reduced

strength level. The comparison is carried out in two steps. First, the Disk 6 data were reduced using multiple linear regression, including the wall thickness and channel skew angle that established that a significant correlation exists for both wall thickness 1.4960 kPa/mm (55 lb/in.² mil) and skew angle 35 to 62 kPa/deg (5 to 9 lb/in.² deg) for Disk 6 samples. The skew angle was eliminated as the cause for the reduced strength because of the positive regression coefficient. The second step was to compare the wall thickness regression coefficient of Disk 6 with that for the general disk population. The Disk 6 coefficient is 14,960 kPa/mm (3747.3 lb/in.²/in.) while the four disk population coefficient is 25,300 kPa/mm (6337.3 lb/in.²/in.). Neither coefficient is large enough to account for the difference in strength [1257 to 2424 kPa (182.3 to 351.6 lb/in.²) mean].

Porosity data, expressed as through-wall leak rates, indicate that this lower than expected strength level could very well be due to high porosity for this disk. Figure 48 plots two frequency histograms showing the distribution of through-wall leakage rates of AGT disks and CATE disks with disk fractures identified with an asterisk. The failures occurred in units with leak rates of at least 4.9 × 10^{-2} kg/s·m² (7 × 10^{-5} lb/sec-in.²). These rates indicate that low strength is at least partially due to high wall porosity.

As indicated earlier, the NGK MAS extruded matrix is being evaluated for its higher temperature capability and the potential of improved strength from the extruded flow paths (which also potentially offer improved heat transfer characteristics). Both triangular (CO3P) and rectangular (CO9P) extrusions are being considered and laboratory specimens of each were tested to determine physical and chemical properties including CTE effects. Results of the CTE testing are shown in Figure 49 for both CO3P and CO9P—both exhibit a more rapid drop in hot face strength than the AS matrix (see Figure 46).

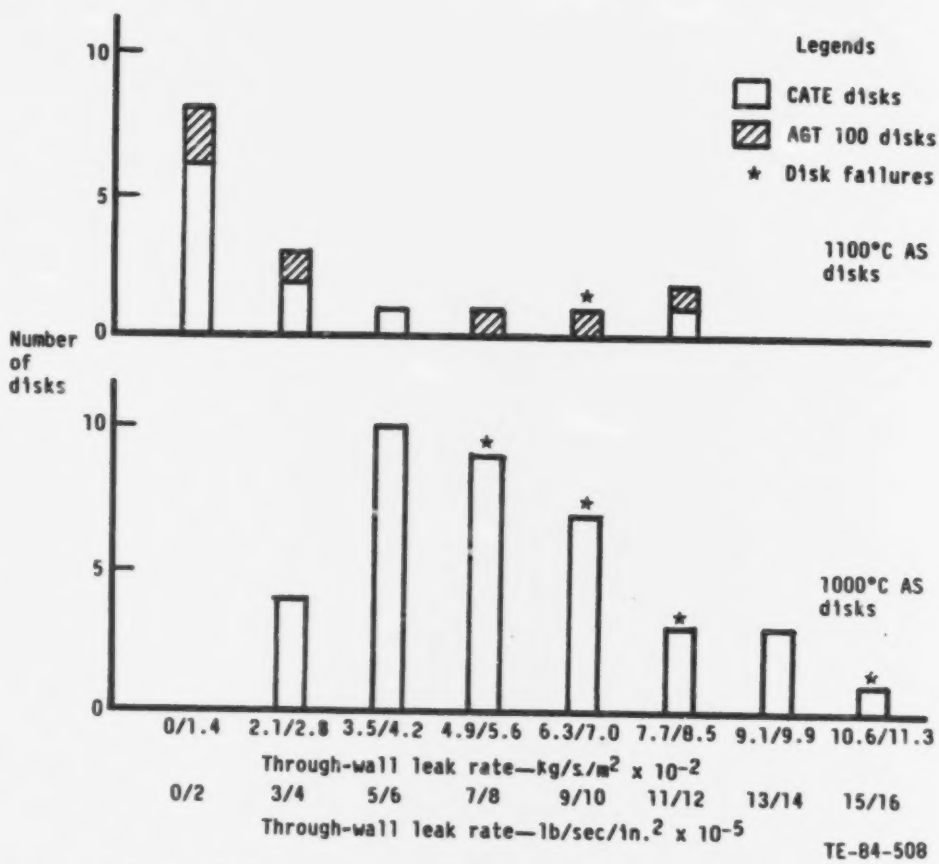

Figure 48. History of disk failures compared with measured through-wall leakage rates indicating low strength is at least partially due to high wall porosity.

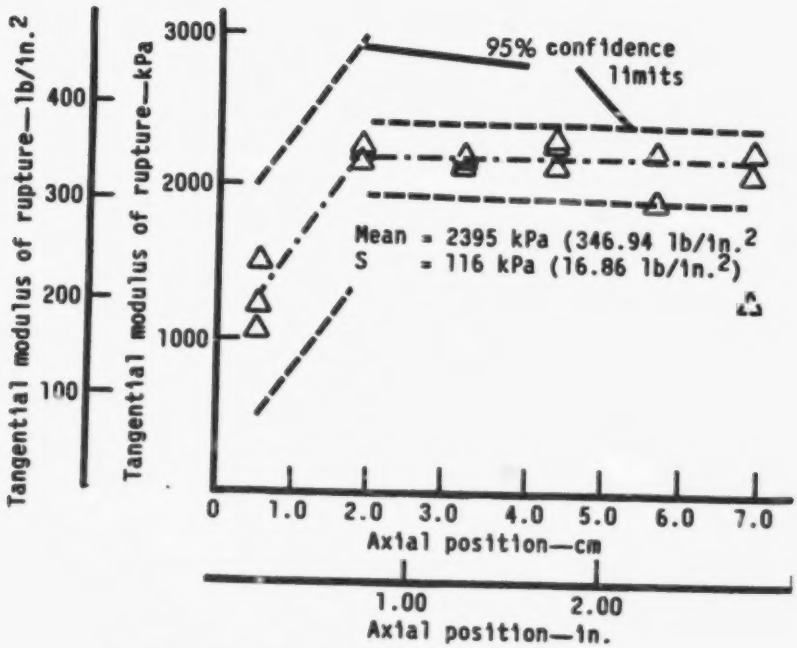

a. MAS/NGK CO3P triangular matrix cyclic thermal exposure at 1010°C (1850°F), 5000 cycles

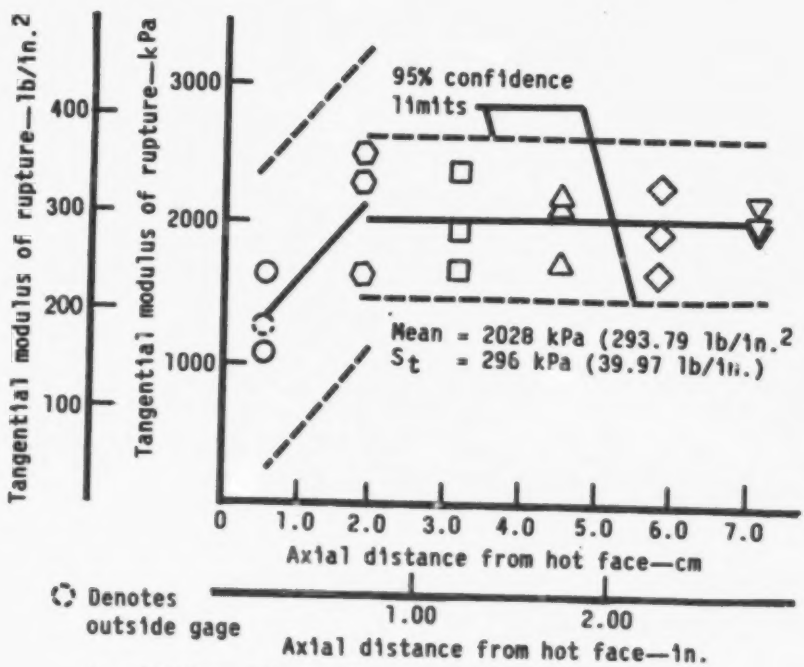
Tangential modulus of rupture—lb/in.2
Tangential modulus of rupture—kPa
95% confidence limits
Mean = 2028 kPa (293.79 lb/in.2
St = 296 kPa (39.97 lb/in.)
Axial distance from hot face—cm
Denotes outside gage
Axial distance from hot face—in.

b. MAS/NGK CO9P rectangular matrix cyclic thermal exposure at 1177°C (2150°F), 100 cycles

TE84-509

Figure 49. CTE test strength for MAS CO3P and CO9P samples.

ORIGINAL PAGE IS
OF POOR QUALITY

During this reporting period, two completed disk assemblies of CO3P, shown in Figure 50, were received and hot rig testing was conducted. Fifteen hours of testing were completed on S/N G-1 triangular (CO3P) disk. The first disk (S/N G-1) was operated at 650°C (1200°F) throughout the engine operating pressure range. Loss of filler cement in the hot-face rim thermal-relief slots that occurred during testing is shown in Figure 51. Minor radial cracks can be seen in the rim between the relief slots radiating inward 1.3 to 2.5 mm (0.050 to 0.100 in.) in several locations. No radial cracks were found at the base of the thermal relief slots. Since the loss of the relief slot cement filler results in a significant leak path, disk leakage data could not be measured and testing was shifted to the second CO3P triangular matrix disk (S/N G-2).

Disk S/N G-2 was tested at 100% engine speed conditions [T_6 = 760°C (1400°F)] and after 4 hr the disk was found to have more relief slot filler missing than the first disk. Although performance measurements were not possible, testing was continued for a total of 46 hr to evaluate the mechanical design changes incorporated in the disk (earlier NGK mosaic disks for CATE failed both in the rim and at the hub attachment). The test validated the mechanical integrity of the mosaic disk but disclosed an unexplained surface deterioration of the hot face that first appeared as a stain (approximately circumferential) both around the hub and near the rim. The stain first appeared after 7 hr of test after a run at T_6 = 870°C (1600°F). Examination showed it was only a stain at that time but at ≈25 hr the matrix walls started breaking down along the stain marks. Testing continued at T_6 temperatures of 927–982°C (1700–1800°F). Figure 52 shows a photograph of the disk after 46 hr when the wall breakdown was ≈1 to 2 mm (0.040 to 0.080 in.) deep. Samples from the disk are to be analyzed at Allison and NGK during the next quarter. The first CO3P disk is to be returned to NGK for application of an improved rim slot filler; the CO9P disks now being completed will also incorporate the new filler.

Limited laboratory CTE testing of the third sample of CGW MAT matrix also was conducted. In the results, shown in Figure 53, the MAT appears to lose hot face strength in a similar manner to the MAS samples described previously. Work is continuing with CGW in defining a formation that will improve the material strength retention after CTE.

7.1.4 Parts Fabrication

Work continued with Tri-Industries during the period to qualify them as a supplier of regenerator parts for the AGT 100 program. Three disk/ring

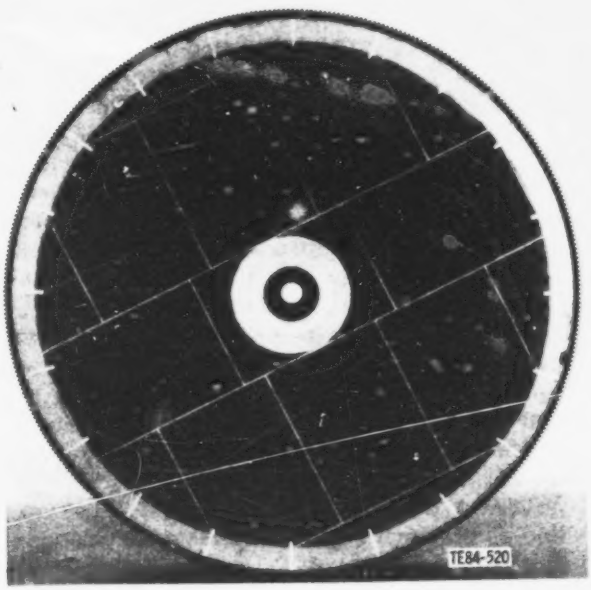

Figure 50. A photograph showing the hot face of an AGT 100 regenerator disk with NGK CO3P extruded matrix.

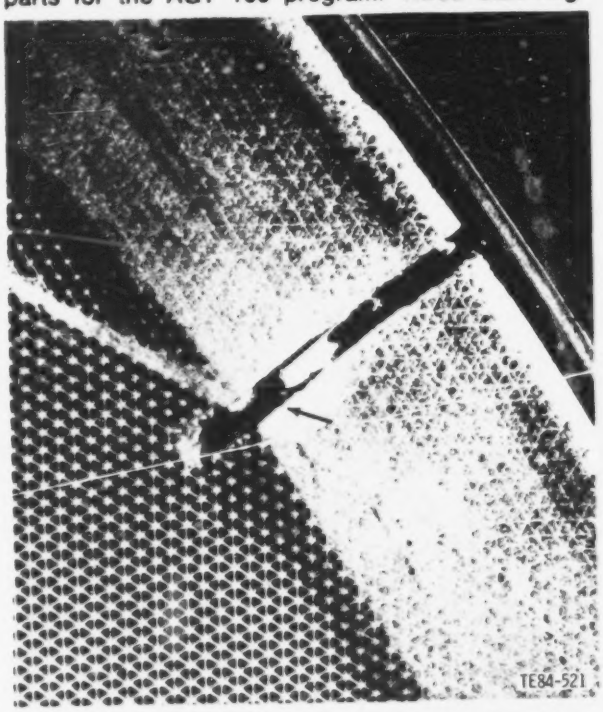

Figure 51. Illustration of the loss of hot face rim relief slot filler that occurred during testing with CO3P disk G-1.

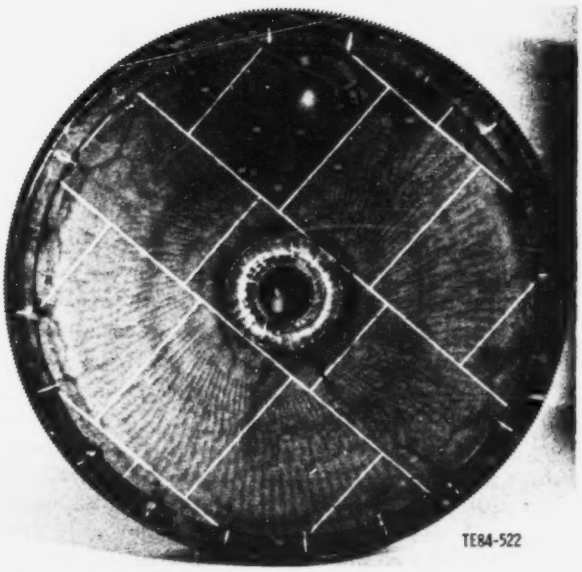

Figure 52. Magnesium-aluminum-silicate disk S/N G-2 after 46 hr testing.

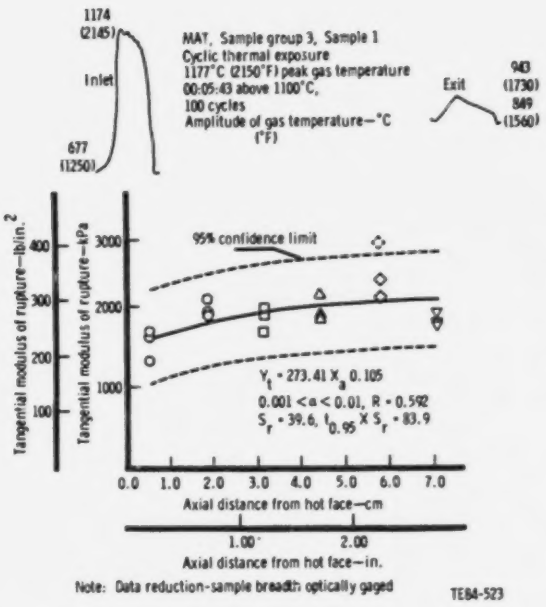

Figure 53. Cyclic thermal exposure test strength of MAT matrix exposed to 1179°C for 100 cycles.

gear assemblies were completed and four outboard seal assemblies delivered. Details have been completed for the initial order of inboard seal assemblies and work is under way to finish these first units.

7.2 RIG DEVELOPMENT TESTING

Regenerator hot rig testing dominated rig testing during these past six months as 145 hr of additional testing was accomplished (480 hr total) on 23 seal/disk combinations. Testing highlights explained earlier included the following:

- qualification of engine hardware sets for engines S/N D-1 and S/N D-2
- testing of silicone leaf seal on metal platform with thermal barrier added
- initial testing of polyimide platform/silicone leaf seal assembly
- completed investigation of inboard seal crossarm cooling effectiveness
- completed initial evaluation of two NGK mosaic disks

Reduced hot rig testing is anticipated during the next six months because of the planned overhaul to update the rig to accept engine regenerator subassemblies and to complete the modeling of the engine flow path. The majority of parts necessary for this changeover are completed, and the rig reconditioning is planned for early spring 1984.

7.3 ENGINE TESTING

Four engine builds and 31 hr of engine testing were completed during the period. The initial ceramic bulkhead failure described in the last report was followed by two additional failures on S/N D-1, BU9 and BU10. The probable cause was determined to be the inability of the power turbine/ceramic bulkhead coupling to adjust to misalignments occurring during engine operation. Figure 54 illustrates the changes to reduce the height of the ceramic bulkhead and to lengthen the coupling. The change accommodates ≈2.5 times greater misalignment and reduces the potential for the coupling to lock in the bore due to friction. New couplings were fabricated and two ceramic bulkheads reworked for the next engine builds.

Two engine builds (engine S/N D-2) and 20 hr of testing were completed with this design change; no additional problems were encountered. Two of the three broken bulkheads were salvageable to the new configuration and are being reworked for later use in the program.

Testing of the first build of engine S/N D-2 was interrupted when it could not be restarted with indications of severe leakage. On teardown the primary rim graphite wearface of the inboard seal was found to be locally worn away at the outside diame-

ORIGINAL PAGE IS
OF POOR QUALITY

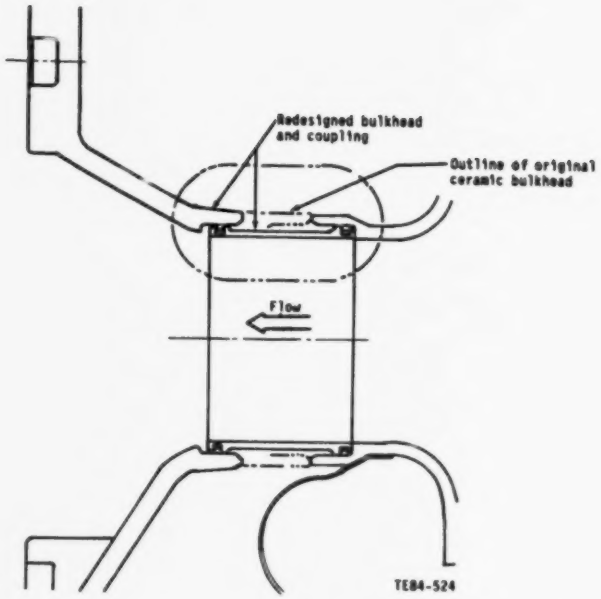

Figure 54. A cross section of the redesigned bulkhead and power turbine coupling.

Figure 55. Photograph of the seal wearface failure on engine S/N D-2, BU1.

ter; the graphite segment was then free to shift radially outward. This opened a joint between the graphite segments and caused the leakage (see Figure 55). Cause of the excess wear was contact between the graphite retention plasma spray and the disk rim coating cement—the resulting debris causing accelerated (≈4 hr) wear of the adjacent graphite surface. The disk and seal assembly from engine S/N D-1 was installed to complete the scheduled testing.

The silicone O-ring support of the ceramic bulkhead continued to indicate distress from overtemperature conditions. A ceramic fiber packing will be installed in the next engine build for evaluation.

VIII. SECONDARY SYSTEMS

During this reporting period activity focused on the gearbox, bearings and seals, and the secondary airflow system. The oil pump in the gearbox did not provide main oil pressure during an engine test. Another oil pump was installed to continue testing and a redesigned valve was incorporated in all pumps. Deterioration of carbon elements in the shaft seals behind both turbines has been minimized by using seals with higher temperature capability. Definition of secondary airflow leakage is being approached systematically by (1) qualitative detection of sources using leak detection dye; (2) initiating plans for quantitative definition including turbine nozzle flow calibration; (3) helium seeding for turbine backface leakage; (4) carbon dioxide dilution measurements for leakage into the flow paths; and (5) carbon dioxide dilution measurement technique verification on the regenerator rig. Also sensitivity studies are being used to determine leakage impact on performance.

8.1 GEARBOX

During initial testing of BU1 of engine S/N D-2, 17 October 1983, the engine was unable to develop main oil pressure. Attempts to correct the situation on the test stand were unsuccessful. To continue engine testing, another pump was installed and the inoperative pump disassembled.

The AGT 100 oil pump is a fixed displacement gear-type pump with a spring-loaded pressure regulating valve that bypasses excess flow to the pump inlet. The regulator is set to 482.63 kPa (70 lb/in.^{2}) and is on during normal engine operation. If the regulating valve became lodged in the box, oil would be bypassed all the time, preventing the development of oil pressure, as the case with engine S/N D-2.

The original regulating valve was short and had a low length/diameter (l/d) ratio. This, in addition to the edge radius, could allow the valve to skew and lodge in the bore (see Figure 56). A design modification was made to increase the length of the valve, increasing the l/d ratio, thereby reducing the possibility of the valve lodging in the bore. This was done by increasing the bore diameter enough to let the valve wall form a pilot for the spring. This allowed the original spring to be used. This modification should then provide oil flow and pressure as originally designed. This revised pump assembly is shown in Figure 57. Bench testing has shown the improved pump to be satisfactory.

8.2 BEARINGS AND SEALS

The AGT 100 engine uses air buffered dual element carbon shaft seals to segregate bearing oil flow and turbine airflow. The seals are placed between the turbine and the thrust bearing on both the gasifier and power turbine shafts. This engine has experienced recurring rapid deterioration of the carbon element nearest the turbine. The deteri-

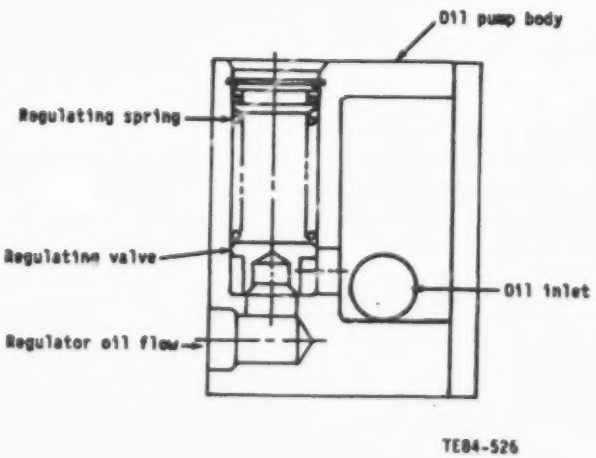

Figure 56. The oil pump assembly showing the original regulating valve.

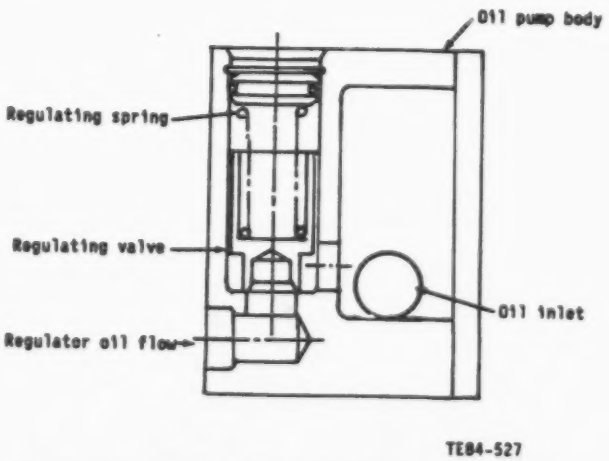

Figure 57. The oil pump assembly showing the improved regulating valve.

oration was caused by overheating the resin binder in the carbon, causing it to bake out. This left the soft carbon susceptible to cracking and erosion.

The first step in stopping this wear was to provide a cooler atmosphere for the seal. This was done by drilling eight 0.762 mm (0.030 in.) diameter holes around the seal to bring compressor discharge air to this area. This arrangement provided a blanket of cooler air to shield the seal from the hot backplate in the gasifier only, as it was the hotter environment. This arrangement is shown in Figure 58.

A second step taken to improve seal life was to improve the temperature capability of the seals. Seals that have a resin binder with a much higher temperature capability than the original seals have been procurred. These two improvements are now installed in an engine and are awaiting testing.

8.3 SECONDARY AIRFLOW SYSTEMS

Qualitative investigation of engine air leakage was conducted on both S/N D-1 and S/N D-2 engines during this reporting period. White titanium dioxide and blue CoAlCr powder dyes were injected into each engine flow path upstream of the regenerator inlet and at the compressor inlet, respectively.

Powder dye injection first took place on BU10 of engine S/N D-1 at nominal conditions of 70% N_G and 538°C (1000°F) BIT. The color traces observed and photographed during subsequent teardown revealed leakage occurring at regenerator seals, interturbine and exhaust duct piston rings, Grafoil seals at scroll cross-key attachments, and the gasifier turbine scroll support spacer. No clear leakage source indications were provided by the two-color system, due to the complexity of the leakage flows and the presence of both colors in the primary stream. Splitline and instrumentation site leakage indications were minimal.

The powder dye injection procedure was repeated at the same nominal run conditions for engine S/N D-2 on BU2. On teardown, evidence of leakage was observed at the regenerator seals, interturbine duct piston rings, and Grafoil seals of the scroll cross-key attachments. Leakage at the exhaust duct piston rings appeared to be considerably less for this test than for the S/N D-1 test. This is attributable to the subsequent changes in the ceramic exhaust duct and coupling designs.

The tests indicated problem areas but could not be interpreted quantitatively. The next step will be to consider methods of measuring engine leakage so that a better assessment of performance can be achieved.

The first engine measure of leakage will be obtained from flow calibration of the gasifier and power turbine nozzles. Earlier rig testing of the gasifier and power turbines showed that turbine equivalent flow correlated well with vane hub static pressure ratio, independent of rotor speed. The flow can be determined from calibration curves and vane pressure ratio measured during engine testing. The difference between measured engine inlet flow and gasifier inlet flow from calibration is an indication of total leakage out of the flow path. The two nozzle calibrations can be used with engine data to determine leakage into the flow path between turbines. Plans were completed for flow calibrating engine S/N D-1 gasifier and power turbine nozzles in a rig adapted to the engine hardware.

The second measurement considered will quantify turbine backface leakage by helium seeding and detection. This concept is illustrated in Figure 59. The engine flow path is broken at the compressor exit and the compressor flow is exhausted. The turbines are supplied externally through the regenerator inlet. The engine inlet is seeded with helium, and the exhaust helium concentration is obtained from mass spectrometer measurements. Since the compressor flow is exhausted, any helium present in the exhaust will have been leaked into the flow path past turbine backface seals. The flows exiting the compressor and supplied to the turbines are also measured directly using orifices.

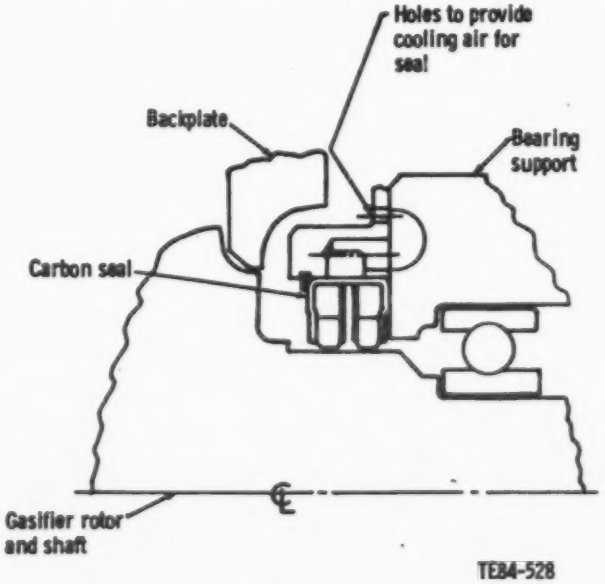

Figure 58. A cross section of the carbon seal installation showing the improved cooling arrangement.

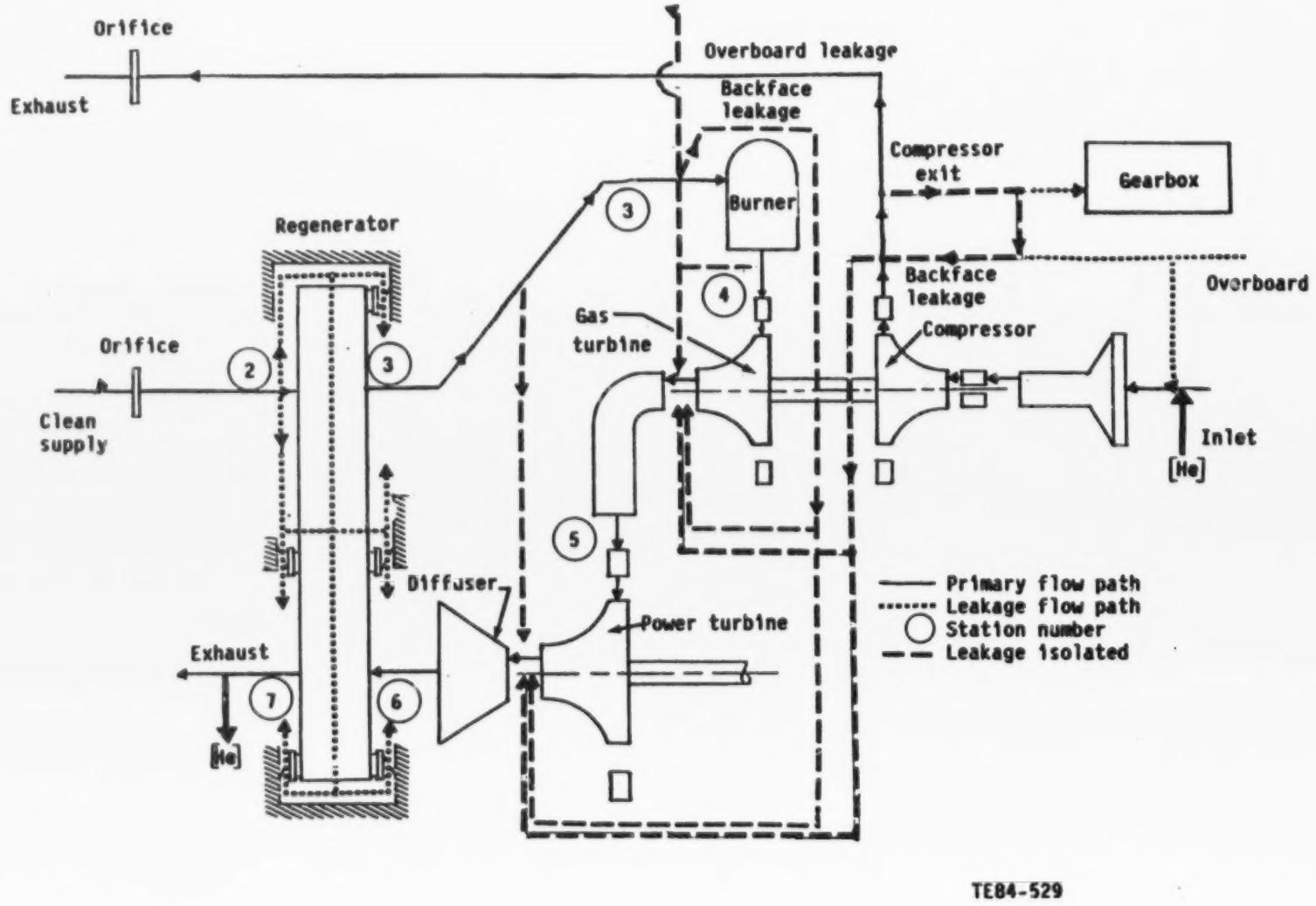

Figure 59. A schematic of the AGT 100 helium leak detection system.

Efforts to outline engine and test-stand modifications necessary to accommodate these measurements began in December.

Measurement of carbon-dioxide dilution downstream of the combustor was investigated as a method of measuring air leakage into the flow path at turbine backface seals and piston rings and at the exhaust side of the regenerator. The measurements of CO_2 concentration can be made using a nondispersive infrared analyzer typically used for emissions characterization. Figure 60 highlights the leakages isolated by measuring the CO_2 concentration change between stations 4 and 6 and stations 6 and 7.

The governing equation for relating the carbon-dioxide concentrations to leakage shows that the leakage measurement accuracy is a function of both the concentration level at the upstream station and the concentration change between stations. The feasibility of the technique was assessed using best estimates of leakage and CO_2 levels measured for the AGT 100 combustor during rig testing. The measurement was determined to be feasible, but also to be sensitive to instrument accuracy. Specifically, the concentration level and change should be measurable, but a very small error in measured concentration corresponds to a significant error in indicated leakage for the levels assumed.

Because of the cost and risk involved with developing the CO_2 dilution technique on the engine, the technique will be first qualified on the regenerator rig, where leakage is measured directly.

The regenerator rig, shown schematically in Figure 61, differs from the engine regenerator system in terms of gas composition. The system uses

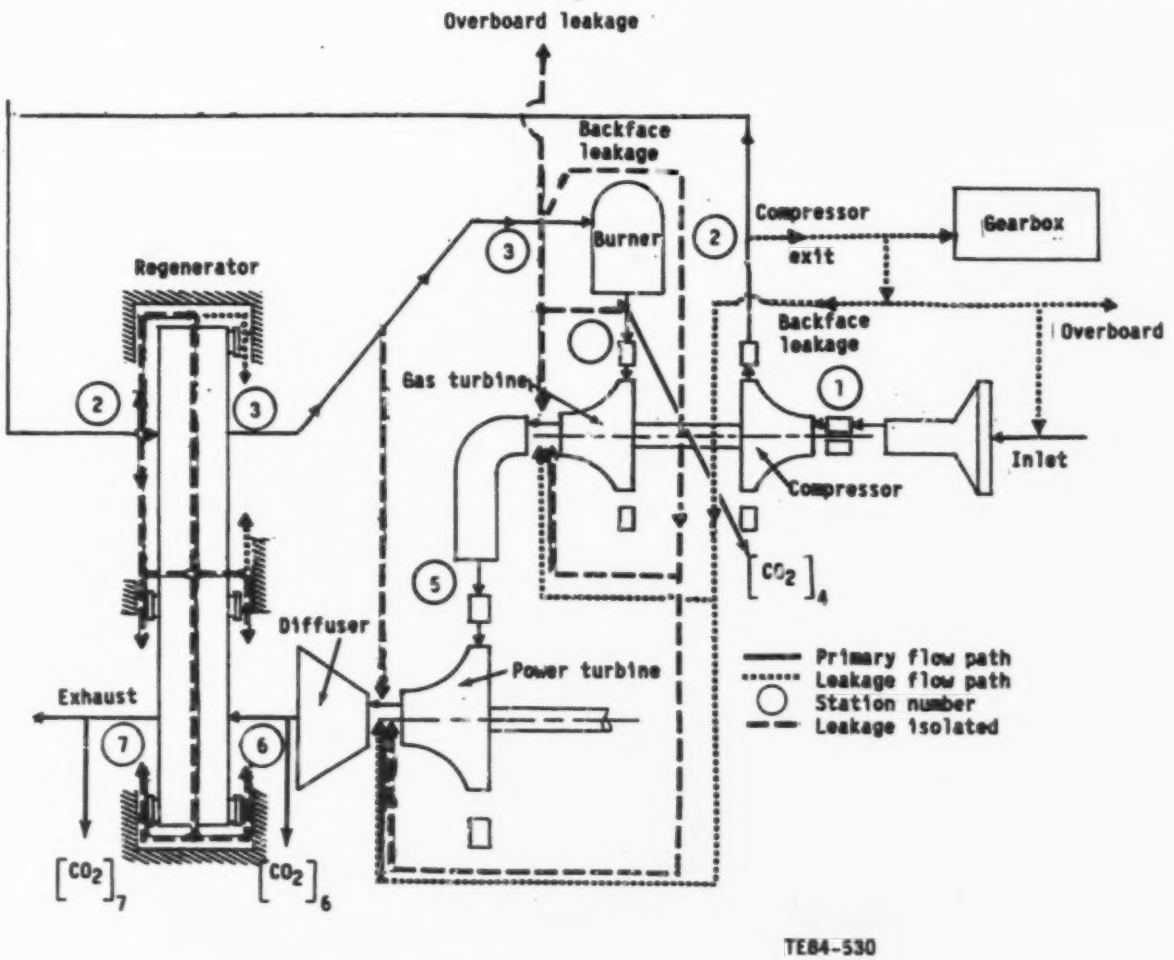

Figure 60. A schematic highlighting the carbon dioxide dilution measurements for AGT 100 leakage testing.

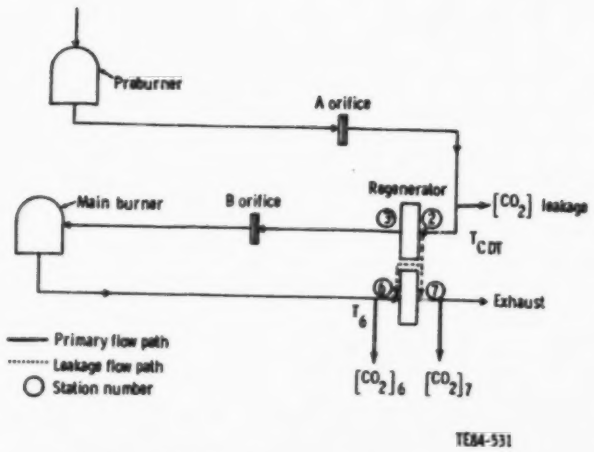

Figure 61. A schematic of the AGT 100 regenerator rig leakage measurement system.

two slave burners to duplicate engine temperatures. The leakage measurement accuracy is a function of inlet concentration level, leakage concentration level, and the change in concentration across stations 6 and 7. Leakage for the rig will have a higher CO_2 level than the engine leakage, and will therefore dilute the primary stream less for a given leakage amount. Nevertheless, the basic principle is the same for the regenerator rig as for the engine, and the rig offers a direct measurement of leakage for evaluating the technique. Rig measurements are planned for early 1984 and are expected to provide a rigorous test of the CO_2 technique. If the measurements are successful, application to the engine will be investigated further.

A performance model leakage sensitivity study was conducted to determine the relative payoff for leakage reduction at a site. The payoff was expressed as a net power increase per percent leakage decrease for operation at a given mechanical speed and turbine inlet temperature. The engine performance model used for the analysis incorporated turbine maps estimated for BU8 of engine S/N D-1 and was further adjusted to match BU8 engine test data record No. 11163. The cycle that matches record No. 11163 was chosen as the baseline for the study. The operating point is nominally N_G = 94%, N_o = 90%, TIT = 1033°C (1891°F). The assumed leakage for this cycle is that predicted for BU8 prior to test.

Net power was assumed to exhibit a linear dependence on leakage of the following form:

$$\Delta HP_{N,\,TIT} = (\partial HP/\partial L_1)\,\Delta L_1 + (\partial HP/\partial L_2)\,\Delta L_2 + \ldots (\partial HP/\partial L_N)\,\Delta L_N$$

$\frac{\partial HP}{\partial L_1}$ change in horsepower per unit change in leakage flow at site 1 (2, 3 etc.) (Ref. Fig. 62)

where all deltas are relative to record No. 11163 values and the influence coefficients, $\partial HP/\partial L_i$, are constants. Each influence coefficient was obtained by independently varying leakage at each of seven sites over a range of 0 to 115% of its BU8 predicted value, rematching the cycle, and holding mechanical speed and turbine inlet temperature. Turbine inlet temperature was maintained by varying starter input at this speed. The net power was taken to be the difference between output shaft power and starter input power.

The seven leakage locations studied are shown in Figure 62. The area labeled 1 denotes overboard leakage from the combustor cavity at E seals and scroll cross-key attachments. The areas numbered 3 and 5 represent backface leakage from the compressor exit. Area 2 represents leakage from the combustor cavity at the gasifier turbine scroll seals and interturbine duct piston rings. Area 4 includes the power turbine scroll and exhaust duct leakage. Region 7 encompasses compressor leakage to the gearbox and overboard leakage at the compressor scroll and transfer tube.

Figure 63 is a plot of hp_{NET} versus leakage for the seven locations. The net power shows a linear dependence on leakage throughout the range considered, with the slope depending on the site of the leakage. Since the change in horsepower with respect to leakage is apparently constant for each location, the sensitivity, $\Delta hp/\Delta L_N$ as $\Delta L_N \rightarrow 0$, is simply the slope of the line.

The results of the study are interpreted in Figure 64. This figure shows the power improvement to be expected after reducing leakage at a site by 10% of its predicted BU8 value. Clearly, the implication is that regenerator leakage has the strongest influence on engine output. Nevertheless, the combined effects of leakage at the turbine scrolls and piston ring seals are nearly as great.

The results of this study are qualitative because the mathematical model of the engine assumes a particular distribution of parasitic losses. The measurements of engine leakage discussed earlier can make the model and future sensitivity studies powerful tools for identifying potential performance gains.

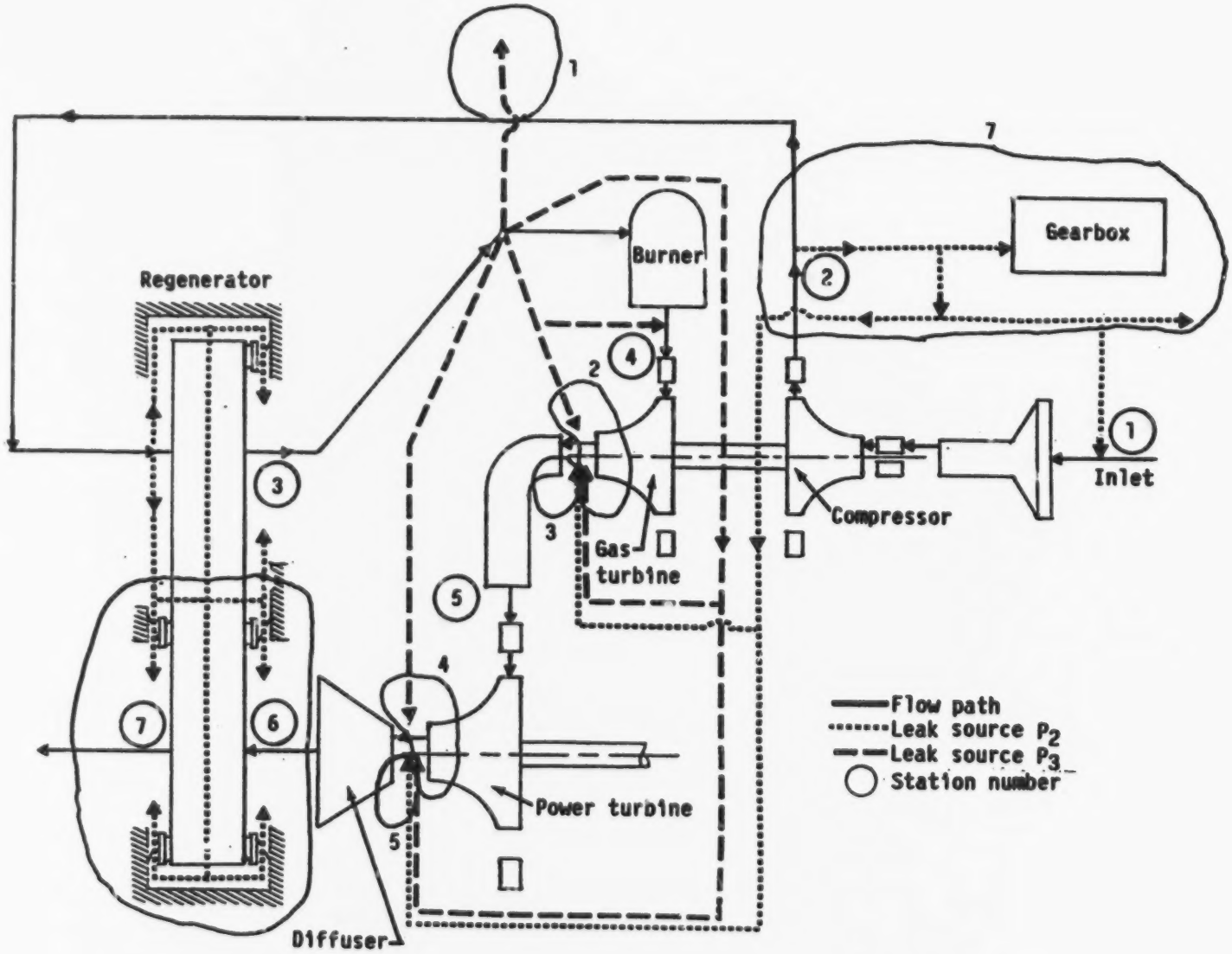

TE84-532

Figure 62. A schematic defining the seven leakage sites included in the performance model leakage sensitivity study.

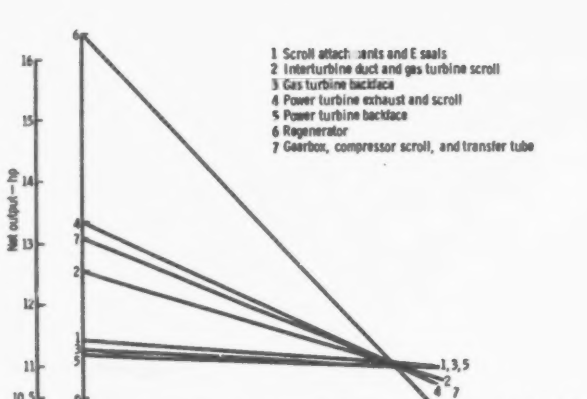
1 Scroll attachments and E seals
2 Interturbine duct and gas turbine scroll
3 Gas turbine backface
4 Power turbine exhaust and scroll
5 Power turbine backface
6 Regenerator
7 Gearbox, compressor scroll, and transfer tube
Net output – hp
Leakage—% REC 11163 value
TE84-533

Figure 63. AGT 100 sensitivity to leakage at each of the seven sites defined for the performance model.

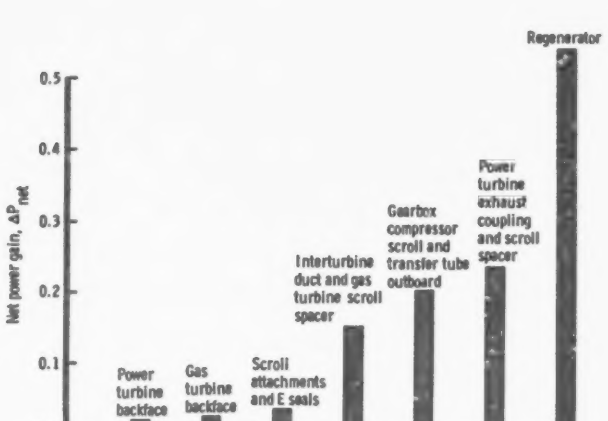
Regenerator
Power turbine exhaust coupling and scroll spacer
Gearbox compressor scroll and transfer tube outboard
Interturbine duct and gas turbine scroll spacer
Power turbine backface
Gas turbine backface
Scroll attachments and E seals
Net power gain, ΔP net
Leakage location
TE84-534

Figure 64. Anticipated power gains for 10% leakage reduction at the seven leakage sites.

IX. MATERIALS DEVELOPMENT

Materials development during this reporting period included effort on thermal barrier materials—both mullite and zircon, silicon carbide components—gasifier scrolls and rotors, and silicon nitride rotors.

9.1 THERMAL BARRIER DEVELOPMENT

Sixteen batches of mullite have been produced and analyzed. Data contained herein show the mean value of thermal expansion for mullite to be only slightly greater than that for silicon carbide. Analysis of current bulk zircon material shows a 25% increase in strength as compared with earlier work; however, advanced materials development to reduce cristobalite in the as-fired condition indicates increases in strength up to 73% are possible.

9.1.1 Carborundum (CBO) Mullite Development

Thermal barrier development has continued on the mullite and cordierite system. Work focused on batch-to-batch consistency.

Sixteen individual batches were produced. Each batch had the same composition, theoretically 59% mullite and 41% cordierite. Previous work showed this to give the most satisfactory values for the coefficient of thermal expansion (CTE).

In each batch the same procedure was followed. Solgel processing techniques were used to form the powder, isopressing was used to form the compacts, and microprocessor-controlled furnace ensured identical firing conditions.

The application and performance of the mullite thermal barrier material depends on a number of factors. For each batch the following were determined: phases by X-ray diffraction analysis (XRDA), coefficient of thermal expansion, modulus of rupture (MOR), density, and percent linear shrinkage. Table XVII lists the results for the 16 batches.

The phases in the material were consistent; mullite was always the major phase and cordierite the minor phase. The strengths represent an overall mean of 95.7 MPa (13,880 lb/in.^{2}). The range in shrinkage was 29.80–24.04%. That represents a ±2.88% window for a target linear dimension. The percent shrinkage window was far greater than expected. (One percent is considered the acceptable level for holding as-fired tolerances.)

The CTE was measured for the 16 batches from room temperature (RT) to 1300°C (2372°F). The maximum and minimum values as well as a mean for all values were used to compute percent expansion from RT to 900°C (1742°F). Figure 65 shows a plot of the percent expansion for sintered silicon carbide (SiC) and the data for the mullite/cordierite batches. The mean value of CTE gave a slightly greater percent expansion value as compared with silicon carbide.

Work on mullite will continue to complete the batch-to-batch consistency study. Also an effort will be directed to understand the strength-controlling features of these materials. Considerations will be given to material systems with greater strength and comparable thermal insulating characteristics.

9.1.2 Zircon Thermal Barrier Material

Bulk zircon. The development of a zircon-based thermal barrier material has continued. Recent effort focused on two areas: batch-to-batch variability and strength improvement.

Concern over the impact of material property variability has prompted an effort to ensure predictable and reliable thermal barrier performance. To assess the variability of critical material properties, four individual billets were produced. Current and identical processing methods were used for each billet, and the MOR, percent shrinkage, and density have been established for each billet.

An 8 kg (17.63 lb) batch of pressing granules was produced by spray drying. Early experience showed that granule storage in a humid environment helped to produce more uniform pore-free microstructures. Compaction was accomplished by uniaxial pressing to 103.41 MPa (15,000 lb/in.^{2}) in a steel die followed by isopressing to 206.82 MPa (30,000 lb/in.^{2}).

Critical properties for the thermal barrier material are: strength (4 pt MOR), percent shrinkage, true density, and coefficient of thermal expansion (CTE). Table XVIII lists the percent shrinkage, true density, and average modulus of rupture for each billet.

Reproducible shrinkage is required in cases where as-fired dimensions are critical. The range of shrinkage results represents a ± 0.3% window on a target linear dimension. Adherence to the procedure for granule preparation and compaction will ensure tight control over as-fired dimensions. The

Table XVII.
Critical properties of mullite thermal barrier material.

Batch No.	Phases Major	(XRDA) Minor	CTE $°C^{-1} \times 10^{-6}$ RT—300°C (°F-1)		Mean MOR— MPa (lb/in.$^2 \times 10^3$)		Standard deviation— MPa (lb/in.$^2 \times 10^3$)		Density— g/cm^3	Percent linear shrinkage—%
1	Mullite	Cordierite	4.96	(2.75)	85.08	(12.34)	—		2.73	27.50
2	Mullite	Cordierite	4.88	(2.71)	109.21	(15.84)	7.92	(1.15)	2.75	29.80
3	Mullite	Cordierite	4.94	(2.74)	101.07	(14.66)	13.85	(2.01)	2.74	27.90
4	Mullite	Cordierite	5.15	(2.86)	94.45	(13.70)	9.79	(1.42)	2.71	28.60
5	Mullite	Cordierite	5.69	(3.16)	87.70	(12.72)	7.37	(1.07)	2.72	27.50
6	Mullite	Cordierite	4.92	(2.73)	121.96	(17.69)	7.03	(1.02)	2.76	25.20
7	Mullite	Cordierite	4.92	(2.73)	105.00	(15.23)	9.10	(1.32)	2.70	24.04
8	Mullite	Cordierite	4.94	(2.74)	93.83	(13.61)	9.37	(1.36)	2.77	25.42
9	Mullite	Cordierite	4.83	(2.68)	110.24	(15.99)	8.48	(1.23)	2.81	24.71
10	Pending	Pending	4.94	(2.74)	94.80	(13.75)	11.30	(1.64)	2.77	24.34
11	Pending	Pending	5.09	(2.82)	121.34	(17.60)	19.37	(2.81)	2.79	24.37
12	Pending	Pending	4.92	(2.73)	95.21	(13.81)	6.82	(0.99)	2.79	25.26
13	Pending	Pending	4.89	(2.71)	75.70	(10.98)	13.23	(1.92)	2.73	24.74
14	Pending	Pending	4.85	(2.69)	86.04	(12.48)	5.92	(0.86)	2.80	24.62
15	Pending	Pending	4.92	(2.73)	76.80	(11.14)	13.65	(1.98)	2.81	26.12
16	Pending	Pending	4.98	(2.76)	72.53	(10.52)	13.30	(1.93)	2.77	25.55

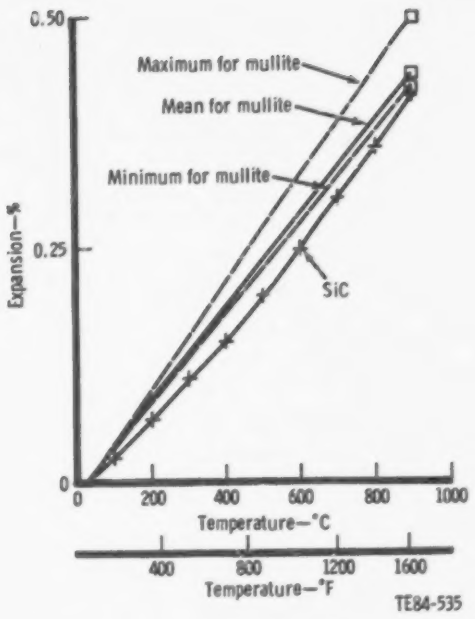

Figure 65. Percent expansion of sintered SiC and mullite/cordierite samples showing a slightly greater percentage for the mean values of mullite as compared with sintered SiC.

data in Table XVIII represent excellent control on a billet-to-billet basis.

Ten machined test bars—6.35 mm (0.25 in.) × 3.17 mm (0.125 in.) × 50.80 mm (2.0 in.)—were cut from each billet. The average MOR for each billet is listed in Table XVIII. A statistical F-test was performed on the data. With 95% confidence, there is no significant difference on a billet-to-billet basis. The overall mean strength of 210.42 MPa (30,520 lb/in.^{2}) represents a 25% increase in strength over the initial load reported early in the development effort. The material described herein has been used in present engine applications and has been designated ZSA-100.

Advanced material development. Studies have been initiated to determine the effect of phase purity and bulk composition on strength. The present bulk zircon raw material has 10-15% silica, which converts to β cristobalite during firing and transforms to cristobalite between 300 and 200°C (572 and 392°F) on cooling. This situation could lead to thermal stress during thermal cycling.

Initial material development has indicated that higher strengths are possible. Biaxial strengths of 337.53 MPa (48,960 lb/in.^{2}) have been observed in compacts (ZSA-200) processed from as-received raw materials. That represents a 60% increase in strength over ZSA-100 tested by the same method. To date efforts have centered on in situ reaction to reduce the cristobalite in the as-fired materials. ZSA-100 is representative of this mode of processing.

A second mode involved leaching out the silica with concentrated hydrofluoric acid (HF). X-ray diffraction analysis and density measurements were performed to determine the effectiveness of this treatment. Bulk zircon powders were agitated in concentrated HF and water in a plastic bottle. Centrifuging was used to separate the powder and acid. Multiple washes with deionized water were used to remove as much HF from the powder as possible. Near stoichiometric zircon was produced. Appropriate sinter-promoting additives and sintering temperatures were identified to yield fully dense materials. Subsequent XRDA showed no trace of silica (cristobalite) and the near 4.6 g/cm^3 (theoretical density for zircon) densities confirmed a very high degree of phase parity. This material has been designated ZSA-300X.

As-fired disks of ZSA-100, ZSA-200, and ZSA-300 were prepared by uniaxial die pressing at

Table XVIII.
Critical properties of zircon-based thermal barrier material.

Billet No.	Percent shrinkage	True density—g/cm^3	Average 4 pt. MOR MPa—(lb/in.^{2} × 10^3) machined surface	Standard deviation—MPa (lb/in.^{2} × 10^3)	Number of bars
1	16.22	4.038	194.77 (28.25)	31.71 (4.60)	10
2	16.21	4.030	224.14 (32.51)	28.75 (4.17)	10
3	16.66	4.026	215.87 (31.31)	32.88 (4.77)	10
4	16.20	4.020	206.98 (30.02)	19.09 (2.77)	10

Table XIX.
Biaxial strength of zircon-based thermal barrier material.

Material designation	True density— g/cm³	Mean biaxial strength— MPa (lb/in.²×10³)	Standard deviation— MPa (lb/in.²×10³)	Number of disks
ZSA-100	4.00	232.07 (33.66)	28.47 (4.13)	8
ZSA-200X	4.12	337.57 (48.96)	30.34 (4.40)	8
ZSA-300X	4.57	166.57 (24.16)	23.23 (3.37)	8

103.42–137.90 MPa (15,000-20,000 lb/in.²). Table XIX lists the biaxial strength results.

9.2 SILICON CARBIDE COMPONENT DEVELOPMENT

Efforts during this reporting period continued to focus on the fabrication, characterization, and qualification of silicon carbide gasifier rotors and scrolls. Development activities at Carborundum (CBO) on the gasifier rotor consisted of extensive processing trials culminating in the establishment of a fixed process for the fabrication of engine candidate rotors. Rotors produced in this study demonstrated substantial improvements in overall quality and dimensional conformance. Overspeed-to-failure spin tests resulted in an average failure speed of 99,330 rpm (115% design speed). Processing studies for the gasifier scroll assembly continued, with four complete assemblies received for evaluation and finish machining.

9.2.1 Gasifier Rotor

The seventh semiannual report (1 January 1983-30 June 1983) described evaluation of the initial group of 48 sintered alpha SiC engine configuration rotors (ECRs). The evaluation was complete except for spin burst tests of nine rotors. These were tested during the current report period. A tabular summary of spin tests for 17 rotors tested is shown in Table XX. Typically, the rotors exhibited surface flow lines and porosity. The burst speed was frequently lower than the 97,100 rpm average burst speed observed for the prototype configuration rotors. The process development work initiated early in 1983 has successfully addressed this experience and resulted in improved quality rotors. The process development is divided into the following three groups:

I. optimized process routing with microprocessor control based on the prototype rotor process
II. experimental processing with various combinations of sprue bushings and injection nozzles

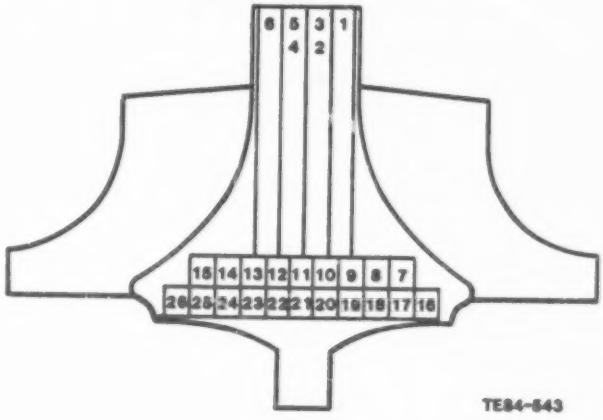

Figure 66. Location of test bars cut from CBO sintered alpha SIC rotors.

III. optimum bushing/nozzle combination with thermal control of the mold base (rotor backface)

The process trials are listed by group in Table XXI. For 1983 deliverables, 614 rotors were molded with a net yield of 122 sintered rotors. The rotors were nondestructive evaluation (NDE) inspected and allocated for subsequent tests. The results of the inspection and the disposition of the rotors are summarized in Table XXII.

Further evaluation of the material/component consisted of strength samples (MOR bars) cut from rotors and spin burst tests of rotors.

Group I. Standard-size four-point modulus of rupture (MOR) test bars were cut from various locations in three rotors (FX 34130, 34135, and 34176) for material strength characterization and to determine the nature and location of the strength-controlling defects. Strength measurements were obtained on material from both the rotor backface region (radial direction) and from the rotor hub near the exducer (axial direction), as shown in Figure 66. The results of these evaluations are summarized in Table XXIII.

Table XX.
Spin test, ECR samples (first 100).

No.	Allison S/N	NDE(1)	Test date	Attach-ment	Nose configuration	I_{pitch} / I_{polar}	Rig configuration	Failure	Comment	Valid test
1	FX 31572	N (severe flow lines and porosity)	10/22/82	Test adapt	Trimmed	0.95	String, 3/16 D/A	Burst at 48,500 rpm		Yes
2	FX 30549	N (cracks and flow lines)	10/22/82	Test adapt	Trimmed	0.95	String	Burst at 75,000 rpm	FX 31551 originally scheduled, blades broken in handling	Yes
3	FX 31566	N	11/24/82	Shaft simul zircon insul	Trimmed	1.94	String	Rotor release at 33,500 rpm	Shaft stub fracture	No
4	FX 31559	N (flow lines)	4/29/83	Shaft simul mullite ins	Trimmed	1.94	String	Burst at 95,200 rpm	Instability (large whip) at 38,000 rpm drove through it. Retraced, whip repeated, two balance attempts, second was successful	Yes
5	FX 30542	N (bent and broken airfoils)	5/13/83	Test adapt	Trimmed	0.95	String	Burst at 93,250 rpm		Yes
6	FX 30557	N (broken airfoils)	6/8/83	Test adapt	Trimmed	0.971	String (1) and (2) Support bearing (3)	Rotor release at 77,000 rpm	1. Severe whip at 77,600 rpm, quill loose in adapter, classic out of balance 2. Refit quill and rebalance. Achieved 81,500 rpm, severe whip, bent shaft. 3. Stagnation at 77,000 rpm, fatigued and failed shaft, rotor released	No
7	FX 31563	N (bent vane)	6/10/83	Test adapt	Full	1.07	String	Rotor release at 56,000 rpm	Severe whip at 42,500 rpm, drove through it, shaft failed at 56,000 rpm	No
8	FX 31553	N (bent vane)	6/24/83	Test adapt	Full	1.07	Support bearing	Rotor release at 65,500 rpm	At 75,000 rpm, stagnation against support bearing, on decel shaft failed at 65,500 rpm	No
9	FX 31558	N (porosity)	7/12/83	Test adapt	Trimmed	0.95	0.79 cm (5/16 in.) quill	Rotor release at 58,000 rpm	Stagnation at 58,000 rpm, 12 sec dwell, test adapter failure, rotor release, cobbed blades, 5/16 in. quill, okay	No
10	FX 30555	A (flow lines)	7/15/83	Test adapt	Trimmed	0.95	String, 0.19 cm (3/16 in.)	Burst at 110,300 rpm	1. Run to 100,000 and check balance 2. Second run to 100,000 and on to burst	Yes
11	FX 30551	N (broken blades)	7/29/83	Test adapt	Trimmed	0.95	0.79 cm (5/16 in.) quill	Burst at 68,000 rpm	Repeat trial, test 9	
12	FX 31544	N (porosity, broken blades)	7/19/83	Test adapt	Trimmed	0.95	String, 0.19 cm (3/16 in.)	Burst at 104,000 rpm	Rebalance required	Yes
13	FX 31546	N (porosity, broken blade)	7/20/83	Test adapt	Trimmed	0.95	String, 0.19 cm (3/16 in.)	Burst at 88,000 rpm	Rebalance required	Yes
14	FX 31549	N (broken blade, flow lines)	8/9/83	Test adapt	Full	1.07	0.79 cm (5/16 in.) quill	Blade at 90,300 rpm	Rebalance required, section of inducer blade released, 0.4 mm Hg vac	Yes
15	FX 31554	N (severe porosity)	8/5/83	Test adapt	Full	1.07	0.79 cm (5/16 in.) quill	Burst at 88,600 rpm	Improved vacuum, 0.4 mm Hg versus 4 mm for prior tests. 1 mil whip	Yes
16	FX 31568	N (severe porosity and flow lines)	8/9/83	Test adapt	Full	1.07	0.79 cm (5/16 in.) quill	Burst at 90,550 rpm	Clean burst, 360 deg splatter little whip, 0.4 mm Hg	Yes
17	FX 31569	A (some porosity)	8/9/83	Test adapt	Full	1.07	0.79 (5/16 in.) quill	Burst at 86,200 rpm	Clean burst, 0.4 mm Hg	Yes
18	FX 31549	N (two broken inlet blades 0 deg and 180 deg)	8/24/83	Test adapt	Full	1.07	0.79 cm (5/16 in.) quill	Sharp increase in whip at 76,000 rpm, burst at 88,300 rpm	1. Rebalance required 2. Suspect release of airfoil section at 76,000 rpm and subsequent unbalance and failure 3. 0.3 mm Hg vacuum	Yes

This exhausts the supply of ECR (first 100) rotors for spin testing.
(1) NDE based on visual and FPI inspection
A = acceptable including defects present that may be machined out to meet all NDE requirements
N = not acceptable

ORIGINAL PAGE IS
OF POOR QUALITY

Table XXI.
Process development, gasifier turbines.

P/N	No. molded	CBO S/N	No. as-molded suitable for binder removal/sinter	Sintered rotors		Process	
				Quantity	Date		
AA100395 (oval shaft)	42	486 to 527	14	9	6/3/83	Reed + microprocessor	
	90	528 to 617	21	20	6/8/83	Reed + microprocessor	Group I(1)
	110	618 to 727	33	29	7/19/83	Reed (0.06 m [2 9/16 in.] shot)	
	16	728 to 743	0			Reed (0.66 m [2 5/8 in.] shot)	
AA100932 (round shaft)	138	744 to 881	16	10	8/5/83	SB-1, N-1 experimental	
	15	882 to 896	7	6	8/22/83	SB-1, N-1 (15)	
	20	897 to 916	5	4	8/22/83	SB-2, N-2 (20—same as 15)	Group II(1)
	33	917 to 949	13	8	9/13/83	SB-2, N-2 experimental	
	15	950 to 964	10	6	9/30/83	SB-2, N-2 (15)	
	15	965 to 979	7			SB-3, N-1 experimental	
	20	980 to 999	8	8	11/8/83	SB-3, N-1 (20)	
	100	1000 to 1099	17	12	11/21/83	SB-2, N-2 (100) without heat	
	100	1100 to 1199	29	10	11/21/83	SB-2, N-2 (100) with heat	
	76	1200 to 1275	0	19	1/23/84 (2)	Variable conditions	Group III(1)
	100	1276 to 1375	27	26	1/31/84 (2)	SB-2, N-2 (100) with heat	
				167 deliverable rotors (estimated)			

Code:
Reed = type of compounder
SB-1, -2, -3 = three sizes for the injection mold sprue bushing
N-1, #2 = two sizes for the injection mold nozzle
(1) see text for definition
(2) estimated

Table XXII.
Summary, development ECRs.

Group I (based on prototype rotor process)

CBO S/N	Allison S/N	NDE[1]	Dimensional[2] nominal = 8.33 mm (0.328 in.) rotor/throat—mm (in.)	Comment	Disposition
508	FX 34128	N	8.15 mm (0.321 in.)	Exducer curled	Reserve
510	FX 34129	N	Not measured	Handling damage	Scrapped
511	FX 34130	A	5.64 mm (0.222 in.)	—	MOR
512	FX 34131	N	7.11 mm (0.280 in.)	—	Trial spin at Balco, burst at 73,420 rpm
515	FX 34134	A	6.78 mm (0.267 in.)	Broken exducer tip	NASA, HIP
516	FX 34135	A	6.60 mm (0.260 in.)	—	MOR
517	FX 34136	N	5.11 mm (0.201 in.)	Exducer droop	Section
519	FX 34137	A	6.60 mm (0.260 in.)	Broken blade	Section
527	FX 34139	N	6.61 mm (0.260 in.)	—	Trail spin at Balco, burst at 69,700 rpm
528	FX 34140	N	7.49 mm (0.295 in.)	—	Display
529	FX 34141	N	7.42 mm (0.292 in.)	—	Spin
530	FX 34142	N	7.44 mm (0.293 in.)	—	Shaft attach
531	FX 34143	N	7.34 mm (0.289 in.)	—	MOR
532	FX 34144	N	7.54 mm (0.297 in.)	—	NASA, HIP
533	FX 34145	N	7.77 mm (0.306 in.)	Large grain	Spin
534	FX 34146	N	7.62 mm (0.300 in.)	—	Shaft attach
536	FX 34147	A	7.65 mm (0.301 in.)	Large grain	Proof spin at Allison at 82,000 rpm
538	FX 34149	N	7.65 mm (0.301 in.)	—	DOE display
543	FX 34150	N	7.65 mm (0.301 in.)	—	Machine
545	FX 34151	N	7.67 mm (0.302 in.)	—	Thermal shock
549	FX 34152	A	7.70 mm (0.303 in.)	—	Spin
550	FX 34153	A	7.95 mm (0.313 in.)	Large grain	Trail spin at Balco, burst at 74,790 rpm
554	FX 34154	A	7.77 mm (0.306 in.)	Large grain	Proof spin at Allison, at 86,000 rpm
561	FX 34155	A	7.87 mm (0.310 in.)	Large grain	MOR
562	FX 34156	A	7.96 mm (0.313 in.)	Large grain	Section
563	FX 34157	A	7.54 mm (0.297 in.)	—	Spin
572	FX 34158	N	7.67 mm (0.302 in.)	—	Pontiac display
574	FX 34159	N	7.75 mm (0.305 in.)	—	Spin
581	FX 34160	A	7.47 mm (0.294 in.)	—	DOE display
621	FX 34162	N	7.36 mm (0.290 in.)	—	Section
622	FX 34163	N	7.42 mm (0.293 in.)	—	Shaft attach
623	FX 34164	N	7.47 mm (0.294 in.)	Large grain	Section
627	FX 34165	N	5.82 mm (0.229 in.)	Exducer droop	Pontiac display
628	FX 34166	N	7.57 mm (0.298 in.)	—	Spin
630	FX 34167	A	7.65 mm (0.301 in.)	—	Spin
631	FX 34168	A	7.50 mm (0.295 in.)	—	NASA, HIP
632	FX 34169	N	7.62 mm (0.300 in.)	—	Spin
634	FX 34170	A	7.50 mm (0.295 in.)	—	Spin
637	FX 34171	N	7.52 mm (0.296 in.)	Cracked blade	Balco Dev
638	FX 34172	A	7.72 mm (0.304 in.)	—	Spin

Table XXII. (cont)

CBO S/N	Allison S/N	NDE[1]	Dimensional[2] nominal = 8.33 mm (0.328 in.) rotor/throat—mm (in.)	Comment	Disposition
639	FX 34173	N	7.77 mm (0.306 in.)	—	Spin
641	FX 34174	A	7.70 mm (0.303 in.)	—	Spin
642	FX 34175	N	7.06 mm (0.278 in.)	Large grain	Spin
643	FX 34176	A	6.60 mm (0.260 in.)	—	MOR
644	FX 34177	N	7.44 mm (0.293 in.)	—	NDE/sect
648	FX 34178	N	7.72 mm (0.304 in.)	—	MOR
650	FX 34179	N	6.91 mm (0.272 in.)	—	NASA
657	FX 34181	N	7.62 mm (0.300 in.)	—	NASA, HIP
669	FX 34183	A	7.72 mm (0.304 in.)	Broken inducer tip	Spin
673	FX 34184	A	7.47 mm (0.294 in.)	—	Spin
681	FX 34185	N	7.57 mm (0.298 in.)	—	Balco/development
682	FX 34186	A	7.57 mm (0.298 in.)	—	Spin
683	FX 34187	A	7.50 mm (0.295 in.)	—	Spin
691	FX 34191	A	6.50 mm (0.256 in.)	Severe distortion	NASA, HIP
702	FX 34192	N	8.05 mm (0.317 in.)	—	Spin
703	FX 34193	N	7.70 mm (0.303 in.)	Broken blade	MOR
714	FX 34194	N	7.95 mm (0.313 in.)	—	Spin
716	FX 34195	A	7.72 mm (0.304 in.)	—	Spin

58 rotors—This is the entire sample of Group I rotors.

Group II (experimental processing)

CBO S/N	Allison S/N	NDE[1]	Dimensional[2] nominal = 8.33 mm (0.328 in.) rotor/throat—mm (in.)	Comment	Disposition
747	FX 34196	A	7.52 mm (0.296 in.)	Surface quality and dimensional conformance varied widely—experimental processing	Reserve
748	FX 34197	A	7.00 mm (0.276 in.)		Reserve
749	FX 34198	A	6.88 mm (0.271 in.)		Reserve
762	FX 34199	A	6.40 mm (0.252 in.)		Reserve
766	FX 34200	A	7.16 mm (0.282 in.)		Insulator attach sample
770	FX 34201	A	5.84 mm (0.230 in.)		Reserve
819	FX 34202	N	6.35 mm (0.250 in.)		Reserve
823	FX 34203	A	6.55 mm (0.258 in.)		Reserve
830	FX 34204	A	7.26 mm (0.286 in.)		Reserve
831	FX 34205	N	7.37 mm (0.290 in.)		Shaft attach sample
854	FX 34207	N	7.32 mm (0.288 in.)		Reserve
868	FX 34208	N	6.81 mm (0.268 in.)		Reserve
870	FX 34209	N	6.68 mm (0.263 in.)		Reserve
876	FX 34210	A	7.32 mm (0.288 in.)		Reserve
877	FX 34211	N	6.81 mm (0.268 in.)		Reserve
884	FX 34212	N	6.73 mm (0.265 in.)		Reserve

Table XXII. (cont)

Group II (experimental processing)

CBO S/N	Allison S/N	NDE[1]	Dimensional[2] nominal = 8.33 mm (0.328 in.) rotor/throat—mm (in.)	Comment	Disposition
886	FX 34213	A	7.04 mm (0.277 in.)		Reserve
888	FX 34214	N	7.19 mm (0.283 in.)		Reserve
892	FX 34215	A	7.11 mm (0.280 in.)		Reserve
893	FX 34216	A	6.76 mm (0.266 in.)		Reserve
894	FX 34217	A	6.91 mm (0.272 in.)		Reserve
896	FX 34218	N	7.24 mm (0.285 in.)		Reserve
903	FX 34219	A	7.19 mm (0.283 in.)		Reserve
904	FX 34220	A	7.62 mm (0.300 in.)		Reserve
905	FX 34221	A	7.14 mm (0.281 in.)		Reserve
906	FX 34222	A	7.16 mm (0.282 in.)		Reserve
913	FX 34223	A	7.37 mm (0.290 in.)		Reserve
920	FX 34224	A	7.72 mm (0.304 in.)		Reserve
925	FX 34225	A	Being measured at		Reserve
928	FX 34226	A	date of report		Reserve
931	FX 34227	N			Reserve
932	FX 34228	A	Being measured at		Reserve
933	FX 34229	N	date of this report		Reserve
934	FX 34230	Not inspected			Returned to CBO
941	FX 34231	N			DOE display
942	FX 34232	N			Reserve
961	FX 34233	N			Reserve
962	FX 34234	N			Reserve
963	FX 34235	A			Reserve
984	FX 34243	N			Reserve
922	FX 34244	A			Reserve
990	FX 34245	A			Airfoil machining trial
1005	FX 34246	A			Reserve
1006	FX 34247	N			Reserve
1017	FX 34248	A			Airfoil machining trial
1020	FX 34249	A			Reserve
1022	FX 34250	A			Reserve
1058	FX 34251	A			Reserve
1063	FX 34252	A			Balco qualification
1065	FX 34253	A			Reserve
1076	FX 34254	A			Allison, two big rig qualifications
1082	FX 34255	A			Allison, two big rig qualifications
1089	FX 34256	A			Reserve
1093	FX 34257	A			Balco qualification

54 rotors—This is the entire sample of Group II rotors.

Table XXII. (cont)

Group III (fixed processing with thermal control of base)

CBO S/N	Allison S/N	NDE(1)	Dimensional(2) nominal = 8.33 mm (0.328 in.) rotor/throat--mm (in.)	Comment	Disposition
1102	FX 34258	A	Being measured at date of this report, fixture utilized during sinter operation to maintain throat opening	Surface generally free of visual indications	Reserve
1103	FX 34259	N			Reserve
1108	FX 34260	A			Reserve
1109	FX 34261	A			Proof spin at Balco
1110	FX 34262	A			Reserve
1113	FX 34263	A			Proof spin at Balco
1114	FX 34264	A			Proof spin at Balco
1118	FX 34265	A			Proof spin at Balco
1124	FX 34266	A			Proof spin at Balco
1126	FX 34267	A			Reserve

(1) NDE based on visual and FPI inspection
A = acceptable including defects present that may be machined out to meet all NDE requirements
N = not acceptable
(2) nominal throat dimension at exducer outer diameter

ORIGINAL PAGE IS
OF POOR QUALITY

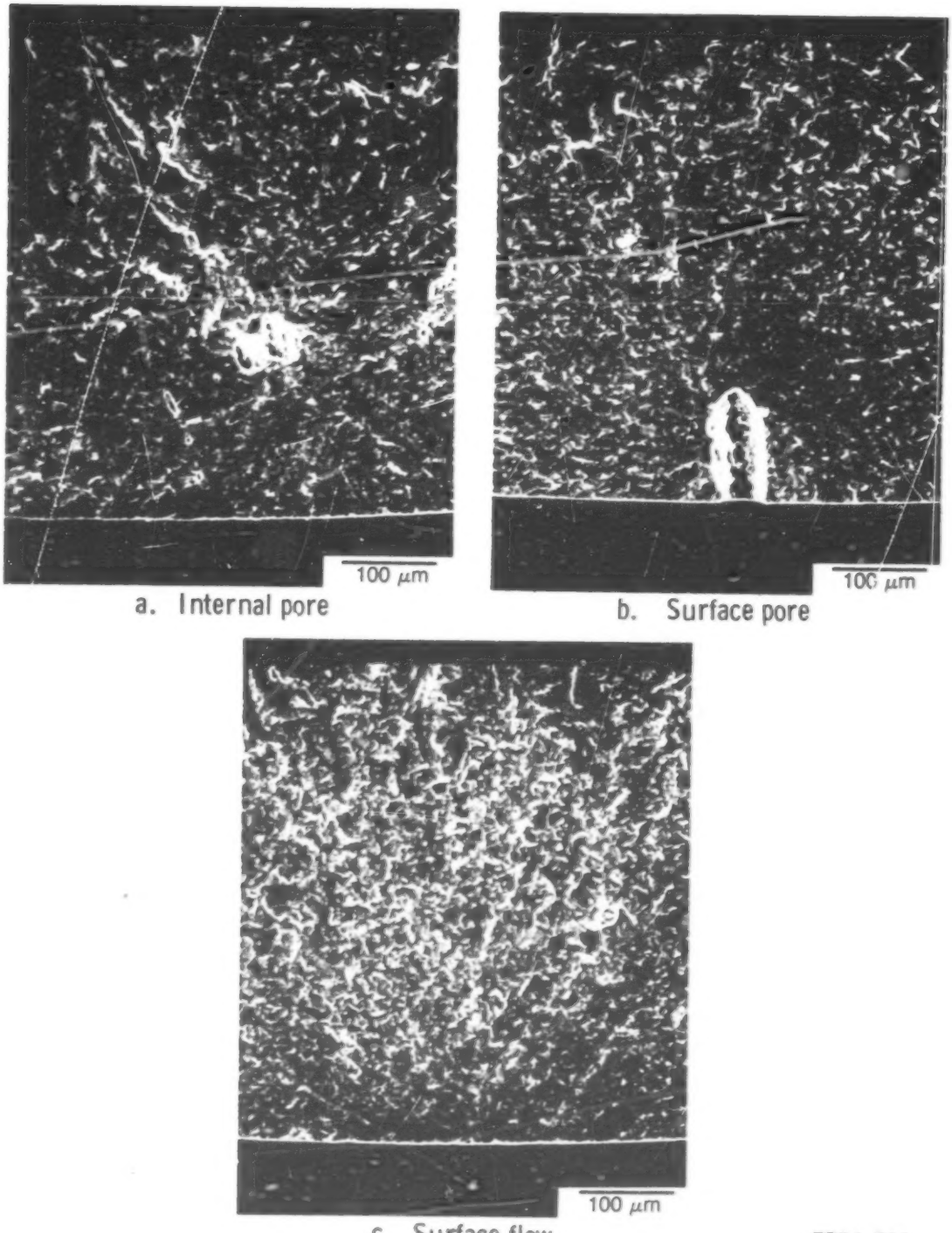

Figure 67. Microphotographs of typical strength-controlling defects observed in a CBO sintered SiC rotor test bar.

Table XXIII.
Strength characteristics of CBO sintered alpha SiC gasifier rotors.

Rotor No.	Radial bar strength—MPa (lb/in.²)	Axial bar strength—MPa (lb/in.²)	Overall strength—MPa (lb/in.²)
FX 34130	406.25 (58,920)	266.70 (38,680)	364.40 (52,850)
FX 34135	404.18 (58,620)	291.11 (42,220)	366.48 (53,150)
FX 34176	407.91 (59,160)	302.62 (43,890)	374.67 (54,340)
Weighed avg	406.18 (58,910)	286.83 (41,600)	368.52 (53,450)

Test material from the backface region (radial) registered an average MOR of 406.18 MPa (58.91 lb/in.²). An average strength of 286.83 MPa (41,600 lb/in.²) was observed for bars cut in the axial direction near the exducer. The primary strength-controlling defects observed in these test bars were internal pores (47%) with the secondary defects consisting of surface pores (37%) and surface flaws (16%). Typical examples of these defects are shown in Figure 67.

Additional characterization of the rotors was accomplished by overspeed-to-failure spin tests. A total of 19 rotors were spin-burst tested. The burst speed is listed versus serial number in Table XXIV. The sample spans a broad range of NDE quality to accommodate process development and variability and includes rotors with surface indications that may not be blendable.

Figure 68 presents the cumulative probability of failure as a function of burst speed for the 19 rotors. An average failure speed of 94,930 rpm and a Weibull modulus of 4.8 were calculated for the data.

Selection of rotors from Group I that are representative of potential engine candidates narrows the sample to nine. These typically exhibit minor surface defects that may be machined out to meet all NDE requirements. Figure 69 illustrates the cumulative probability of failure as a function of burst speed for the nine rotors. An average failure speed of 99,330 rpm and a Weibull modulus of 6.4 were calculated for the data. This is a significant improvement over the initial group of ECRs (see Table XX). The Group III rotors are expected to demonstrate even better strength.

Group II. The Group II rotors (see Table XXIII) represent various processing trials addressing improved quality/strength. The entire sample of 54 sintered rotors was received. A particular combination of injection parameters was identified from the experiment, which resulted in the best quality rotors. These parameters were chosen for the Group III fixed processing manufacture. During the Group II trials, a fixture for support of the exducer throat during the sinter operation was successfully developed and demonstrated. This corrected the closed throat seen for the initial rotors (see Table XXII, CBO S/N 508 through 716).

Group III. A sample of 10 of the Group III rotors (see Table XXII) was received with additional delivery of approximately 35 planned for January 1984. These are candidate engine rotors. The optimization includes thermal control of the rotor backface area of the injection mold—a newly developed process control feature. Preliminary evaluation indicates the surface is generally free of indications and the rotors conform to drawing dimensions. Based on these satisfactory results, processing of an additional supply of rotors was initiated. Two hundred were molded with approximately one third clearing inspection for subsequent processing.

Of the previously noted sample of ten received to date, five rotors have been committed to proof spin test for rotor/shaft attachment development. The rotors are serial numbers: FX 34261, FX 34263, FX 34264, FX 34265, and FX 34266.

The technical milestone plan for development of the rotor/shaft attachment scheme is shown in Figure 70. The development plan culminates in proof of concept of the attachment. To ensure the availability of qualified engine components, the milestone plan further identifies manufacture of an engine qualified assembly and spares.

9.2.2 Gasifier Turbine Scroll Assembly

Seven sintered alpha silicon carbide (SASC) scroll assemblies were fabricated by CBO during this reporting period. One assembly (scroll No. 1) was delivered machined (less vane pockets) to Allison, one assembly (scroll No. 2) is in the machining process at Atlas Tool, Inc, two assemblies (scroll Nos. 5 and 7) were shipped to Allison for casting layout, and three assemblies (scroll Nos. 3, 4, and 6) were rejected at CBO. The following is an inspection summary of these scrolls.

Table XXIV.
Rotor spin burst tests (Group I rotors).

No.	Allison S/N	Test date*	Burst speed--rpm
1	FX 34141	12/06/83	92,500
2	FX 34152(1)	12/07/83	102,500
3	FX 34157(1)	12/08/83	105,500
4	FX 34159(1)	12/14/83	100,500
5	FX 34166	11/30/83	89,500
6	FX 34169	12/03/83	82,000
7	FX 34170(1)	12/09/83	100,000
8	FX 34171	11/29/83 at Balco	89,200
9	FX 34172	12/03/83	82,000
10	FX 34173	12/02/83	106,000
11	FX 34174(1)	12/03/83	101,500
12	FX 34175	12/06/83	95,000
13	FX 34183(1)	12/03/83	95,500
14	FX 34184(1)	12/14/83	105,000
15	FX 34185	11/29/83 at Balco	107,500
16	FX 34186	12/05/83	100,500
17	FX 34192	11/30/83	77,000
18	FX 34194	12/13/83	70,500
19	FX 34195(1)	12/05/83	102,000

*Tested at Allison unless otherwise stated

(1) Rotors free of surface indications or rotors with minor surface indications that may be machined out to meet all NDE requirements

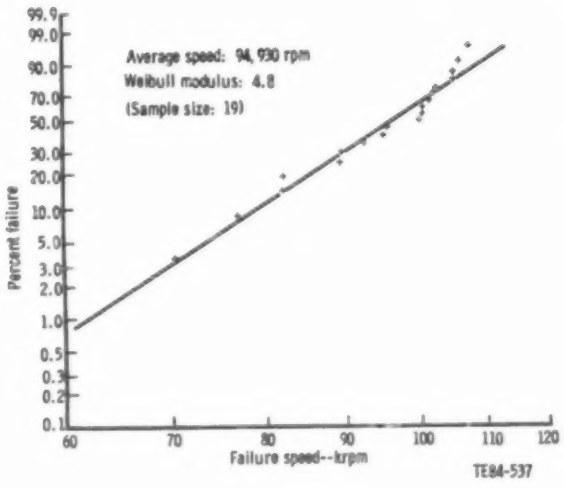

Figure 68. Cumulative probability plot of spin-burst failure for 19 Group I rotors.

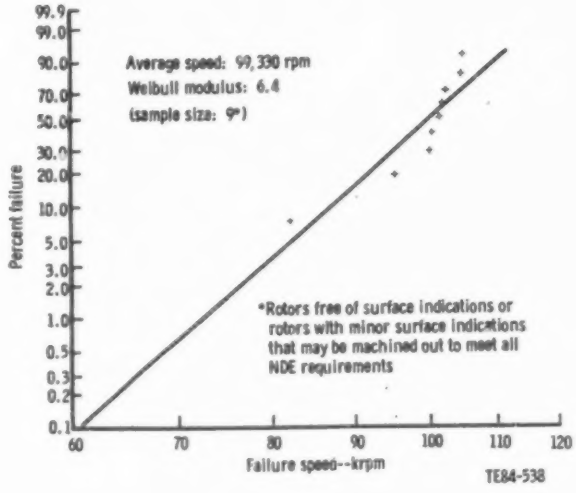
Average speed: 99,330 rpm
Weibull modulus: 6.4
(sample size: 9*)
*Rotors free of surface indications or rotors with minor surface indications that may be machined out to meet all NDE requirements
Percent failure
Failure speed--krpm
TE84-538

Figure 69. Cumulative probability plot of spin-burst failure for nine Group I rotors meeting all NDE requirements.

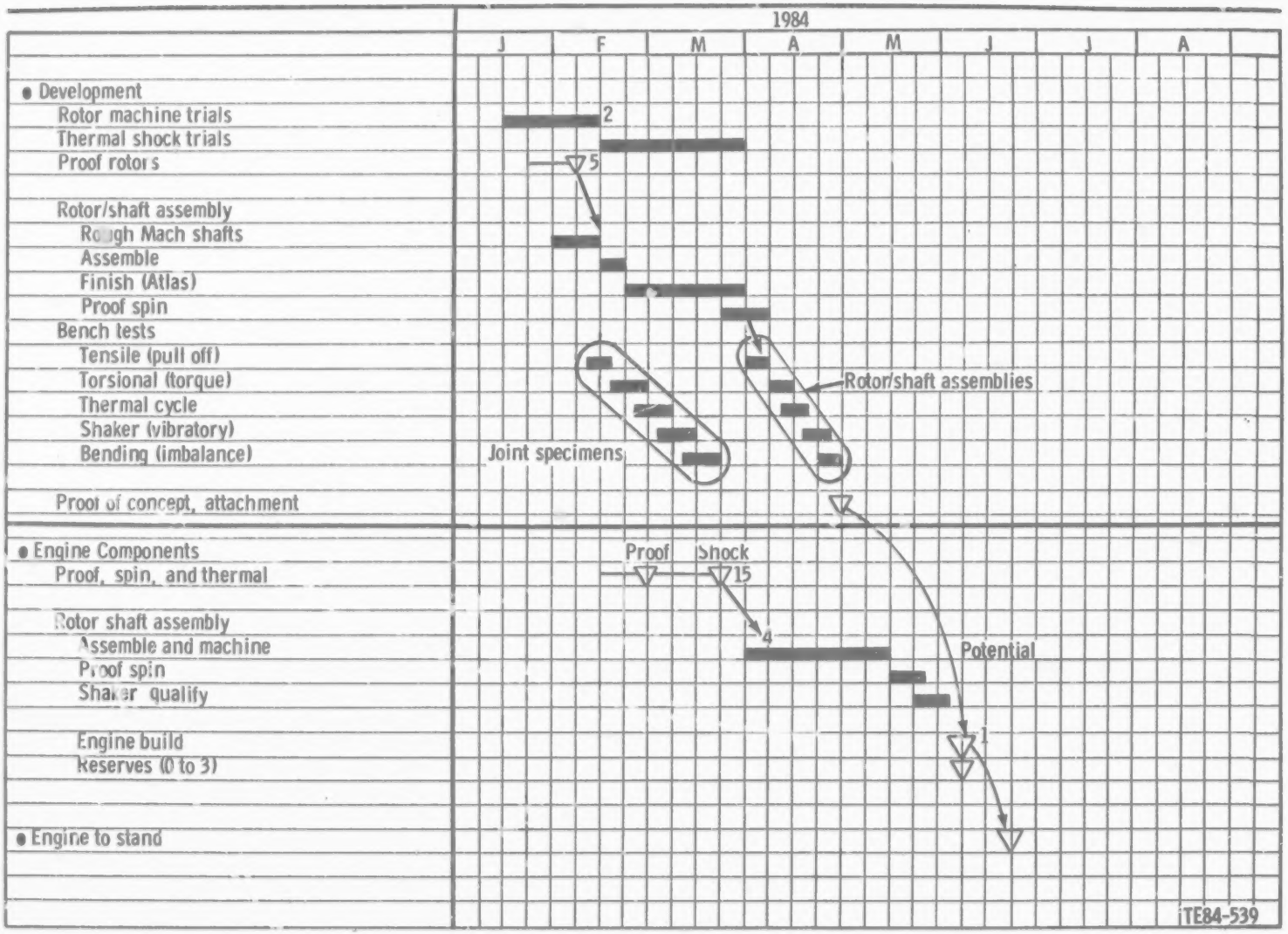

Figure 70. Technical milestone plan for development of the rotor/shaft attachment.

ORIGINAL PAGE IS
OF POOR QUALITY

ORIGINAL PAGE IS
OF POOR QUALITY

Scroll No. 1

- The first trial machining of this assembly was completed (see Figures 71 and 72).
- One lug was broken during machining by some type of impact as observed from the chippage in the failed area.
- Dimensional analysis indicated this part was not machined to print due to distortion in critical areas of the casting, i.e., combustor inlet, crossover duct, and the mating surface for the outer backplate (shown in Figure 71).

Scroll No. 2

- The part was shipped to Allison for casting layout.
- Dimensional analysis revealed distortion in the same areas as in scroll No. 1; however, sufficient stock was available to machine this part to print specification.
- The assembly was shipped to Atlas Tool, Inc, for machining. Delivery is expected mid January 1984.
- This scroll assembly will be used for initial checkout of the scroll thermal shock rig.

Scroll Nos. 3, 4, and 6

- These scrolls were rejected by CBO for dimensional distortion in the casting.

Scroll No. 5

- Dimensional layout revealed the casting to be similar to but more severely distorted than scroll assemblies No. 1 and No. 2.
- Further dimensional analysis is required to determine if a usable machining datum can be identified.

Scroll No. 7

- Dimensional layout revealed this part to be distorted in the same areas as the previous scroll assemblies. Further dimensional analysis has determined a datum feature that is acceptable for machining.
- This assembly will be machined during the first quarter CY 1984.

Due to dimensional anomalies in the casting, Allison and CBO initiated an investigation in December 1983 to address the dimensional distortions in the casting (fixturing, additional quality control, preassembly inspection, and the mold).

NDE was performed on scroll assemblies Nos. 1, 2, 5, and 7. The following is a summary of the results.

Each of the four scroll assemblies delivered to Allison (scroll Nos. 1, 2, 5, and 7) were examined by visual and fluorescent penetrant techniques. A limited number of radiographs were also produced to provide additional volumetric evaluation. Scroll No. 2 has four major linear indications (at locations similar to those shown in Figure 71) on the outer surface near the combustor inlet and the surrounding area. These indications are not visible in the radiographs, which means although they range from 0.5 mm (0.020 in.) to 1.5 mm (0.059 in.) in length, they are not deep. One additional linear flaw was identified by CBO during X-ray evaluation. This indication is in a low stress region that mini-

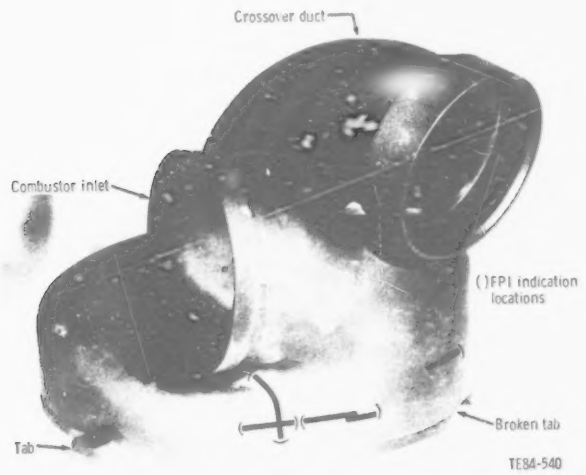

Figure 71. Ceramic scroll assembly No. 1 photograph showing FPI indications on the outer surface and a broken tab.

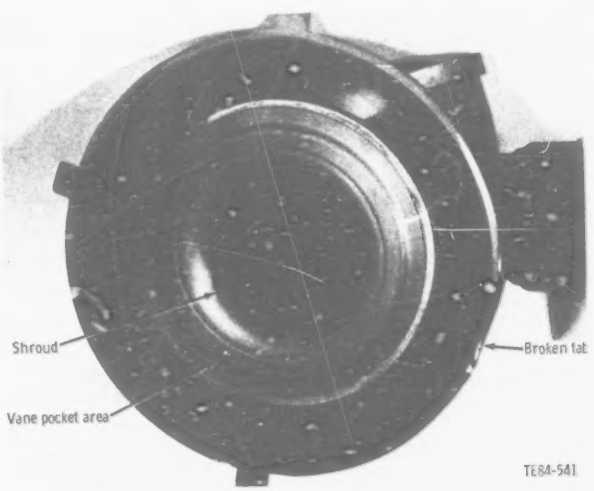

Figure 72. Ceramic scroll assembly No. 1 photograph showing machined shroud surfaces.

ORIGINAL
OF POOR QUALITY

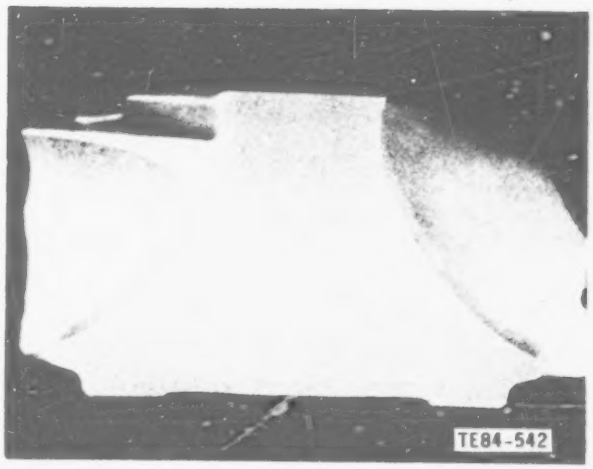

Figure 73. Internal surface of GTE Laboratories HIP processed injection molded AY6-100 Si_3N_4 rotor.

mizes its impact. Scroll Nos. 1, 5, and 7 also have linear indications in the outer scroll body. These indications appear to be shallow and in low stress regions. However, scroll No. 7 has one linear indication in the neck region under the combustor inlet. Although this area is considered a slightly higher stress region, the flaw is shallow and could be removed by minimal blending.

9.3 SILICON NITRIDE COMPONENT DEVELOPMENT

Efforts at GTE Laboratories during this reporting period have continued to focus on the development of injection-molded AY6-100 silicon nitride (Si_3N_4) gasifier rotors. In particular, the use of hot isostatic pressing (HIP) as a means to eliminate the recurring difficulties with internal cracking observed in the sintered Si_3N_4 rotors is being evaluated.

A total of 10 AY6-100 Si_3N_4 rotors were injection molded at GTE, subjected to binder removal, partially sintered to approximately 75% density to provide structural integrity, and shipped to ASEA, Sweden, for HIP processing. The average density of the rotors measured 3.21 g/cm^3 (98% theoretical). The internal surface of sectioned HIP processed rotors exhibited no evidence of macroscopic laminations or flaws, as shown in Figure 73. Visual and fluorescent penetrant inspection (FPI) examinations of the rotors revealed numerous shallow surface indications; however, these indications are much less severe than those observed in the sintered Si_3N_4 rotors.

The material strength characteristics of the HIP processed Si_3N_4 were determined by cutting test bars measuring 25.4 × 2.54 × 1.27 mm (1.0 × 0.10 × 0.05 in.) from the rotor in both radial and axial directions. The average four-point MOR [outer span = 22.9 mm (0.90 in.), inner span = 10.2 mm (0.40 in.)] of the radial test bars measured 761.06 MPa (110,380 lb/in.^{2}) with a standard deviation of 166.91 MPa (24,202 lb/in.^{2}). The average strength of the axial test bars measured 687.05 MPa (99,622 lb/in.^{2}) with a standard deviation of 172.74 MPa (25,050 lb/in.^{2}).

While GTE Labs continues to address the development of sintered injection molded Si_3N_4 rotors, preliminary results of the HIP processing experiment are encouraging. Further characterization of the HIP processed rotors is pending, with five overspeed-to-failure spin tests planned for the next reporting period.

X. CONTROLS DEVELOPMENT

Controls development during this reporting period included effort to support engine operation without a pilot flame and incorporate software changes dictated by engine testing. Also change main fuel nozzle purge procedures were changed and an improved fuel control system was developed.

10.1 ENGINE OPERATION WITHOUT PILOT FLAME

A system was successfully installed on engine S/N D-2 to turn off the pilot flame after starting to prevent carbon formation and attendant hot spots in the combustor. This system was more complicated than might be expected because the fuel metering valve design results in uncontrollable main flow if pilot metering is stopped. To avoid this, the engine pilot nozzle, shut-off solenoid, and air system were duplicated taking the flow into an overboard collector. The switch from engine to overboard was made by energizing the overboard section before de-energizing the engine section using a make-before-break relay.

10.2 SOFTWARE CHANGES TO SUPPORT ENGINE TESTING

10.2.1 Burner Variable Geometry Control

The electronic control positions the burner variable geometry (BVG) based on fuel/air ratio (F/A) and burner inlet temperature (BIT). Several lean blowouts were experienced while running the engine with the pilot flame turned off and an attempt was made to alter the BVG settings to enrich the primary combustion zone. When a rich flashback occurred, more burner rig data were needed to guide the effort.

Rig data with no pilot flame were collected near the end of the reporting period and the software was reprogrammed to obtain a more suitable BVG map, as shown in Figure 74. Some changes were also made to improve the accuracy in calculating main nozzle fuel flow for the F/A input to the BVG map.

10.2.2 Pilot Light-Off Detection

When initiating a start, the start nozzle fuel flow is held off until pilot light-off is detected. Temperature rise was sensed by a thermocouple in the pilot flame tube, but maintaining reliable positioning of this thermocouple without overheating was difficult and failure to detect light-off inhibited starting.

Observation showed that adequate temperature rise was being sensed at turbine inlet so a software change was made whereby a rise in either the pilot or turbine inlet thermocouple now signals pilot light-off.

10.3 MAIN FUEL NOZZLE PURGE

An improvement was made to the main fuel nozzle purge system. Testing will continue into 1984. The old method was to open an overboard vent solenoid at shutdown allowing internal engine air pressure to blow out the main manifold, a technique used successfully on other engines. However, this method did not prevent carbon buildup on the AGT 100.

The new system uses an external air supply to purge fuel into the engine, clearing the manifold and burning at the initiation of shutdown. The air supply was regulated to 17 kPa (2.5 lb/in.^{2}) above internal engine pressure. Several different pressure settings were evaluated to minimize the temperature spike produced and clear fuel at the same time. Evaluation of this trade-off will continue.

10.4 IMPROVED FUEL SYSTEM

Component testing of an improved electric fuel pump and metering valve began in September 1983. System bench testing was started in December and will continue in 1984 to address dynamic response of the valve.

10.4.1 Electric Fuel Pump

The new pump weighs approximately 1 kg (2.2 lb) and is substantially smaller than the pump presently being used for engine testing. Three units were received and tested up to 1379 kPa (200 lb/in.^{2}) at 2 to 15 V direct current. Delivery rate met the specifications and no problems were encountered.

10.4.2 Fuel Metering Valve

The new system meters fuel directly through a proportional solenoid rather than controlling the

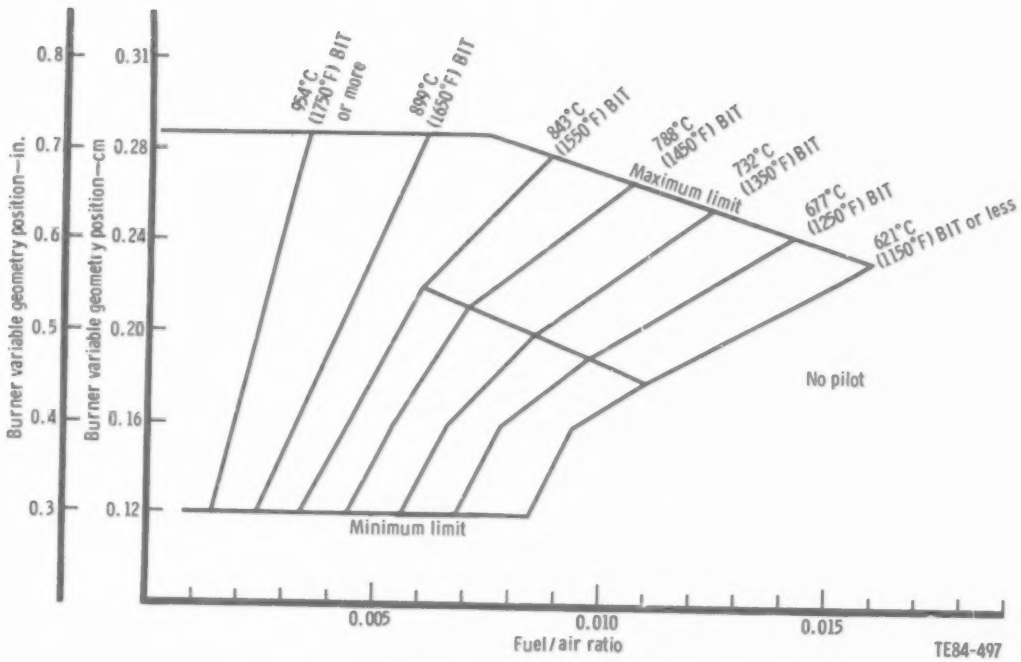

Figure 74. BVG map for operation without pilot flame.

amount through a bypass throttling valve. When completed, engine testing with or without a pilot flame will be simplified. Testing will also eliminate the failure mode of the present system where fuel is not controlled if the pilot nozzle plugs.

Three valves were received and two were bench tested. Steady-state performance was satisfactory, but dynamic response was inadequate for introduction to the engine. Frequency response was good to only 0.5 cycles per second compared with 3.0 cycles per second for the valve now running the engine. Trapped air may be the problem but this remains to be defined.

10.4.3 Electronic Control Unit

A second electronic control unit was built in November for dedicated use with the new fuel system. The only hardware change required was to scale the fuel driver circuit to a higher level, compatible with the new valve. Software logic was simplified due to the direct metering valve, and these changes were defined and implemented. Complete integration and bench checkout will be made in 1984 after valve improvements are defined and tested.

XII. SUPPORTIVE MANUFACTURING, COST, AND MARKETABILITY

An experimental die development and parts fabrication program on two of the major sheet metal engine components was concluded at Pontiac Motor Division. The object of the program was to verify the manufacturability of the combustion case assembly bulkhead incorporating revisions proposed during the manufacturing feasibility and cost analysis studies. The program was also to verify the potential of a new cost savings proposal on the regenerator housing. Two experimental dies were fabricated and both parts were successfully made incorporating the proposed changes. The conclusion drawn from the program was that these parts can be manufactured on a high volume production basis with the potential for additional cost savings in the reference power-train design (RPD) engine.

12.1 MANUFACTURING FEASIBILITY

The effort at Pontiac during this reporting period has been devoted to an experimental die development and parts fabrication program on two of the major sheet metal engine components: the combustion case assembly bulkhead and the regenerator housing. The objectives of this program were as follows:

- to verify the manufacturing feasibility of the bulkhead incorporating design revisions as previously proposed and included in the manufacturing and cost analysis for the RPD engine
- to verify the manufacturing feasibility of a new cost reduction proposal on the regenerator housing not previously included in the manufacturing and cost analysis for the RPD engine
- to gain experience with the draw and forming characteristics of SAE 4130 steel
- to gain experience regarding the downstream machining requirements based on the outcome of actual parts fabrication

The bulkhead (AA-100691-5) was selected because the manufacturing analysis indicated that the initial design had several deep-drawn areas that were not acceptable for high-volume production. Thus the analysis was based on a proposed redesign of these areas. The purpose of the experimental die development program was to verify the manufacturability of the redesigned part as proposed.

Figure 75 shows a bulkhead produced from the experimental die, then manually trimmed. Analysis of this part indicates that it can be made successfully from SAE 4130 steel with the proposed design changes on a high-volume basis.

The experimental die was made to represent a draw die, the first of several dies required in the production process. Additional dies for production would include a trim die for trimming the excess material left from the draw die, a flange and restrike die to qualify the flat areas and outside diameter, and finally two separate piercing dies to punch the required holes in the part. The definition of the formed flat areas and outer flange on the parts produced from the experimental draw die were of high enough quality to conclude that the additional operations for production would be routine. Thus no further experimental dies were thought necessary for verification. Bulkheads made from the experimental die program were furnished to Allison for future reference.

The regenerator housing (AA-100584-2) was selected to verify the manufacturing feasibility of a new cost reduction proposal that was proposed to Allison by Pontiac following completion of the manufacturing and cost analysis for the RPD engine.

Figure 75. Combustion case assembly bulkhead made from experimental die.

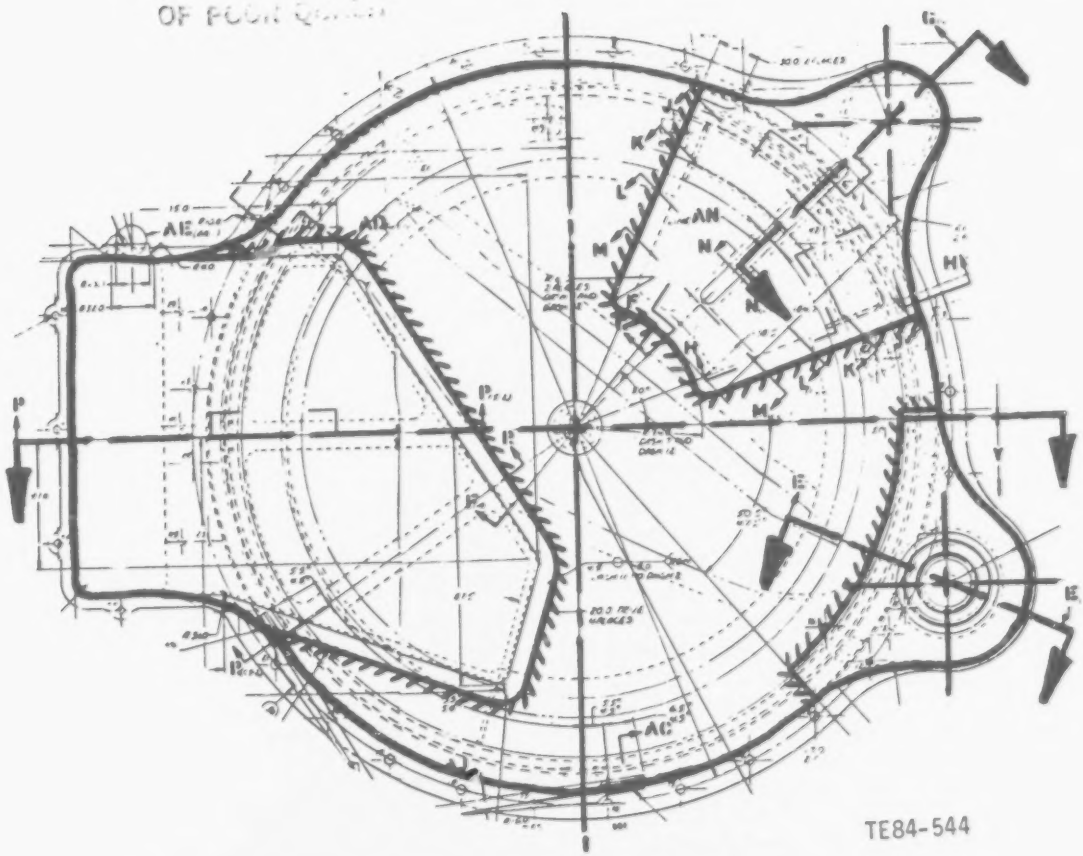

Figure 76. Initial four-piece weldment design for regenerator housing.

This analysis was based on the initial design of the assembly consisting of four major stampings welded together to form the exterior of the housing, and included the costs associated with making and welding the separate stampings, as shown in Figure 76.

The new proposal was to form the exterior of the housing from one piece of metal and to avoid the manufacturing costs associated with the separate stampings. Inasmuch as this proposal involved a large stamping with deep draws, it was determined that an experimental die tryout program would be required to verify the validity of the proposal. If successful, a redesign of the engine for the RPD configuration could take advantage of the resulting cost savings.

Figure 77 shows a regenerator housing produced from the experimental die, then manually trimmed. Analysis of the part indicates that the proposed stamping can be made successfully in one piece from SAE 4130 steel on a high-volume production basis.

Figure 77. Proposed one-piece regenerator housing made from experimental die.

The experimental die was a draw die, and additional dies for production would include a shimmy trim die, a restrike die, and a pierce die. The parts produced from the draw die were of high enough

quality to conclude that the additional operations for production would be routine, thus no further experimental dies would be required for verification. Regenerator housings made from the experimental die tryout program were furnished to Allison for future reference.

APPENDIX A. TERMS AND DEFINITIONS

AGT	advanced gas turbine
AGT 100	the AGT model being developed by Allison
AS	aluminum silicate
BIT	burner inlet temperature
BU	buildup number
BVG	burner variable geometry
°C	degrees Celsius
CBO	Carborundum Company
CGW	Corning Glass Works
cm	centimeter
CTE	cyclic thermal evaluation
CTE	coefficient of thermal expansion
CY	calendar year
S/N D-1	the first experimental AGT 100 engine
S/N D-2	the second experimental AGT 100 engine
DOE	U.S. Department of Energy
E	Young's modulus
ECR	engine configuration rotor
ECU	electronic control unit
EDR	Engineering Development Report (of Allison)
EMI	electromagnetic inspection
EMTL	Energy Materials Testing Laboratory
°F	degrees Fahrenheit
F/A	fuel-to-air ratio
ft	foot
GM	General Motors Corporation
GTE	General Telephone and Electronics Corp
h or hr	hour
HIP	hot isostatically pressed
Hz	Hertz
I/B	inboard
IGV	inlet guide vane
in.	inch
kg	kilogram
kPa	kilopascal
L	liter
LAS	lithium aluminum silicate
lb	pound
lbm	pound mass
LBO	lean blowout
m	meter
mA	milliampere
MAS	magnesium-aluminum-silicate
min	minutes
mm	millimeter
Mod I	the first design of AGT 100 using some ceramic hot section components
Mod II	the second AGT 100 design with ceramic hot section components
MOR	modulus of rupture
MPa	megapascal
N	force (Newton) or speed of rotation (rpm)
N_1	gasifier speed of rotation
N_2	power turbine speed of rotation
NASA	National Aeronautics and Space Administration
NDE	nondestructive evaluation
NGK	a Japanese manufacturing company
O/B	outboard
P_s	probability of survival
PMD	Pontiac Motor Division of General Motors
psig	pounds per square inch gage
RBSiC	reaction-bonded silicon carbide
Ref	reference
RFB	rich flashback
RPD	reference power-train design
RTV	room temperature vulcanizing
s or sec	second
SAE 4130	a ultra-high strength steel
S/N	serial number
TD	teardown
TIT	turbine inlet temperature
TOT	turbine outlet temperature
β	average coefficient of thermal expansion
Δ	difference between two measurements, e.g., T
η	efficiency = E/2G-1

1. Report No.	2. Government Accession No.	3. Recipient's Catalog No.
NASA CR-174798		

4. Title and Subtitle	5. Report Date
ADVANCED GAS TURBINE (AGT) TECHNOLOGY PROJECT	MARCH 1984
	6. Performing Organization Code
7. Author(s)	8. Performing Organization Report No.
Engineering Department, Allison Gas Turbine Operations	EDR 11682
9. Performing Organization Name and Address	10. Work Unit No.
Allison Gas Turbine Operations, Div of General Motors Corp P.O. Box 420 Indianapolis, IN 46206-0420	11. Contract or Grant No. DEN 3-168
12. Sponsoring Agency Name and Address	13. Type of Report and Period Covered
U.S. Department of Energy Office of Vehicle and Engine Research Development Washington, D.C. 20545	Contractor Report (Draft)
	14. Sponsoring Agency Code DOE/NASA

15. Supplementary Notes

Semiannual report, prepared under Interagency Agreement DE-AE01-77CS51040
Project Manager: P. T. Kerwin, Transportation Propulsion Division,
NASA Lewis Research Center, Cleveland, OH 44135

16. Abstract

Significant development activity occurred during the July-December 1983 period in the Allison-Pontiac AGT 100 Advanced Gas Turbine Technology Project. Two builds engine serial number (S/N) D-1 were evaluated through dynamometer testing. Accumulated test time was 11 hr 42 min raising its total time to 20 hr 40 min. A second engine, S/N D-2, was assembled and accumulated 20 hr 39 min of test. Only two builds of engine S/N D-2 were required, and only the regenerator was disassembled between the two builds. Through 1983, total accumulated engine test time (burning) was 41 hr 19 min. Engine D-2 incorporated a modification to the interface system between the ceramic regenerator bulkhead and power turbine scroll assembly, solving the problem of cracked bulkheads experienced on the last builds of engine D-1. A design modification was defined to eliminate the tendency to leak hot gas from the engine flow path into the gearbox vent cavity. Compressor aerodynamic analyses that identified impeller modifications for improved performance were completed. These near-term improvements will be tested next period on a compressor rig. Two turbine aerodynamic improvements were designed for 1984 implementation: improved gasifier vane shape and a reduced capacity power turbine. Combustor development included rig changes to better simulate the engine flow path and to provide viewing stations for use of optical pyrometers. Rig testing was conducted to proof-test ceramic units, to examine starting and igniter relocations, and to map stability limits. Regenerator testing evaluated 23 disk/seal combinations in 145 hr of hot rig testing. Advanced concepts included a silicone leaf seal, polyimide integral wearface and seal platform, different crossarm cooling systems, low-leakage aluminum silicate disks, and an extruded magnesium-aluminum silicate disk. Ceramic turbine rotor development experienced improvement in molding, baking, and sintering engine configuration rotors. Nineteen sintered alpha silicon carbide rotors were cold-spin tested to failure. Average burst speed was 94,930 rpm. The first finish-machined ceramic scroll assembly was received. This assembly, made of sintered alpha silicon carbide, is composed of five separate component parts. Fabrication of a thermal shock rig for proof-testing static ceramic components was initiated, and most parts completed by the end of 1983.

17. Key Words (Suggested by Author(s))	18. Distribution Statement
Automotive gas turbine Ceramic components Engine configuration rotors Alternate propulsion systems Improved fuel economy	Unclassified--unlimited

19. Security Classif. (of this report)	20. Security Classif. (of this page)	21. No. of Pages	22. Price*
Unclassified	Unclassified		

* For sale by the National Technical Information Service, Springfield, Virginia 22151